Fiber-based scanning-probe magnetometry with nitrogen-vacancy spins in diamond nanobeams
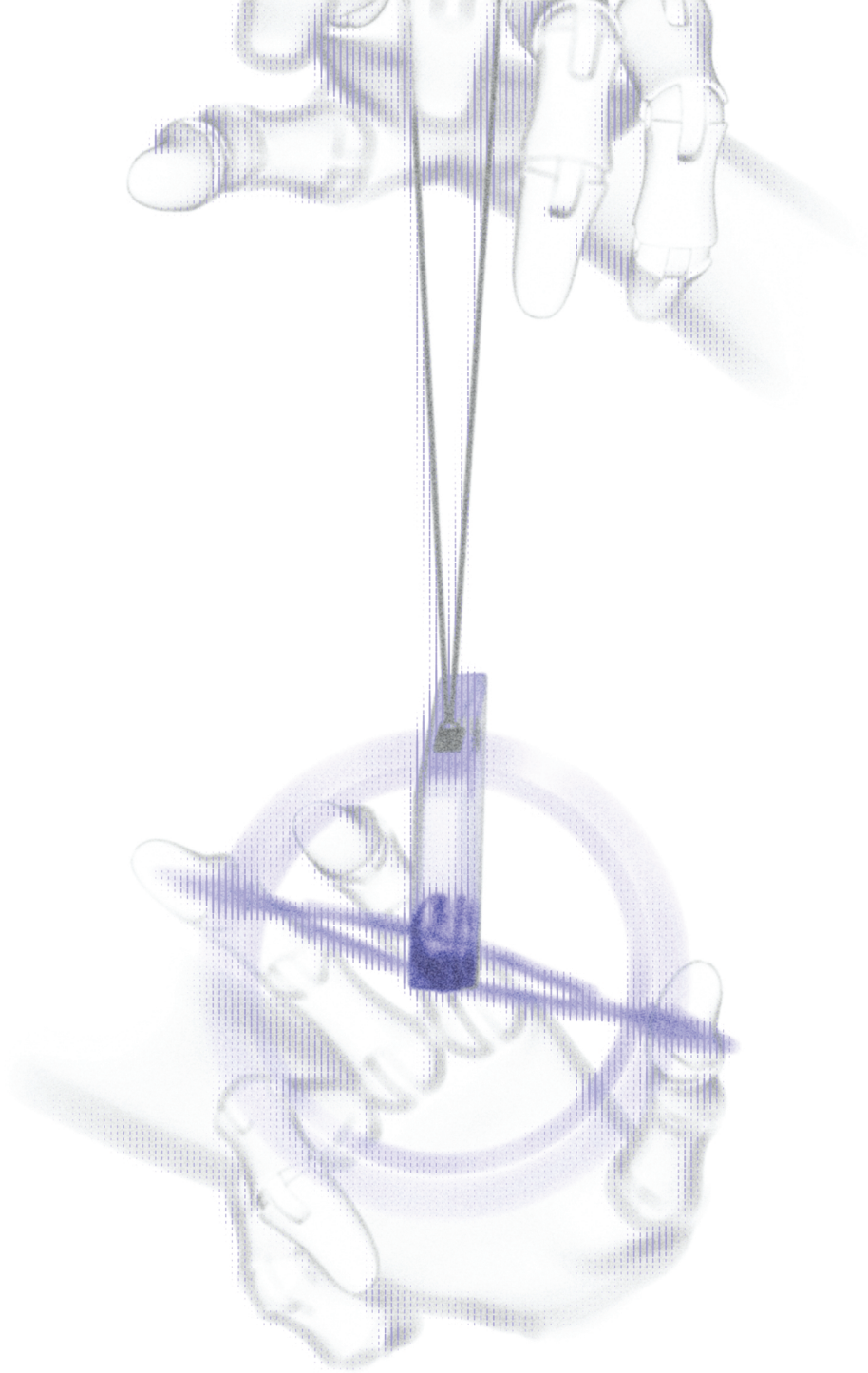
Li, Y.

Important note
To cite this publication, please use the final published version (if applicable).
Please check the document version above.

Fiber-based Scanning-probe Magnetometry
with Nitrogen-vacancy Spins in Diamond Nanobeams

[Yufan Li]

Fiber-based scanning-probe magnetometry with nitrogen-vacancy spins in diamond nanobeams

Fiber-based scanning-probe magnetometry with nitrogen-vacancy spins in diamond nanobeams

Dissertation

for the purpose of obtaining the degree of doctor
at Delft University of Technology
by the authority of the Rector Magnificus, Prof. dr. ir. T.H.J.J. van der Hagen,
chair of the Board for Doctorates
to be defended publicly on
Monday 27th, January 2025 at 10:00 o'clock

by

Yufan LI

Master of Science in Physics,
Eidgenössische Technische Hochschule Zürich, Switzerland

born in Xi'an, China

This dissertation has been approved by the promotors.

Composition of the doctoral committee:

Rector Magnificus	chairperson
Dr. ir. T. van der Sar	Delft University of Technology, *promotor*
Prof. dr. ir. R. Hanson	Delft University of Technology, *promotor*
Dr. R. A. Norte	Delft University of Technology, *copromotor*

Independent members:

Prof. dr. P. G. Steeneken	Delft University of Technology
Prof. dr. ir. T. H. Oosterkamp	Leiden University
Prof. dr. A. G. Widera	University of Kaiserslautern-Landau, Germany
Dr. T. H. Taminiau	Delft University of Technology
Prof. dr. A. F. Otte	Delft University of Technology, *reserve member*

An electronic copy of this dissertation is available at
https://repository.tudelft.nl/.

“我所有的困惑降落在黎明复现之前”

All of my confusion touches down before the rise of the dawn

缺省《平原》

The Plain · Default

Contents

Summary

In modern-day research, magnetometry provides valuable information for a wide range of studies. Among all the different forms of magnetometers, the nitrogen-vacancy (NV) lattice defect in diamond has emerged as a powerful magnetic field sensor thanks to the combination of sensitivity, spatial resolution and versatile capabilities. High-fidelity microwave control and optical readout of the NV spin over a wide range of conditions has enabled applications in condensed matter physics, chemistry, biology, geoscience and many more. In particular, its capability of visualizing magnetic phenomena with high spatial resolution has proven to be a powerful tool in both fundamental physics and applied sciences. Advances in NV magnetometry in the past decade have led to numerous breakthroughs, especially in revealing the nanoscale physics of condensed matter systems.

However, the free-space optics generally used for optical interrogation of the NV spins are challenging to realize in cryogenic, intra-cellular, or other hard-to-reach environments. As such, realizing robust all-fiber-based NV probes with efficient optical readout could enable new measurements in low-temperature (quantum) or biological systems.

Therefore in this thesis, we tackle this challenge by developing a fiber-based scanning-probe NV magnetometer, consisting of a tapered diamond nanobeam that is optically coupled to, and manipulated with, a tapered optical fiber. In chapter 1, we start by introducing the concept of magnetometry and NV magnetometers, and explaining how the fiber-coupled diamond nanobeam can be a feasible solution towards NV measurements in hard-to-reach environments. To further elaborate and motivate this project, in chapter 2 we explain in detail the theoretical and experimental foundations of NV magnetometry, as well as the working principle of a scanning-probe magnetometer with fiber-coupled diamond nanobeams.

Chapters 3 and 4 focus on the process of making these fiber-coupled diamond nanobeam probes. In chapter 3, we describe the process of fabricating NV-hosting diamond nanobeams out of a single-crystal bulk diamond. This process is divided into two parts: the creation of nanobeams using a recipe based on the reactive ion etching (RIE) of diamond, and the creation of NV centers within the nanobeams using ion implantation. For the latter, we show that the NV centers can be deterministically created at the beam tip through angled ion implantation. Then in chapter 4, we demonstrate the approach to couple the fabricated diamond nanobeams to tapered fibers. We first show that it is possible to directly use the tapered fiber to break the nanobeams off the diamond substrate and achieve optical coupling in the same step. Then we demonstrate an improved workflow using optical glue to robustly couple the fiber and the nanobeam with optimized optical coupling efficiency.

Throughout the course of the project, two types of fiber-coupled nanobeams have been developed. The "homogeneous-NV" probes consist of diamond nanobeams with ensemble NVs distributed homogeneously along the entire nanobeam, and the nanobeams are coupled to the tapered fibers through direct fiber break-off. The "tip-NV" probes consists of deterministically implanted NVs at the tip of the nanobeams, and the nanobeams are glued to tapered fibers. Chapters 5 and 6 then discuss the characterization and application of these probes. Specifically, in chapter 5 we demonstrate the through-fiber readout of NV photoluminescence and estimate the coupling efficiencies at the fiber-nanobeam interface for both types of probes. In chapter 6 we implement our two generations of devices in proof-of-principle magnetic imaging measurements. With the homogeneous-NV probes, we image the spin waves in a thin magnet in one dimension, and with the tip-NV probes we demonstrate 2D scanning-probe operation and image the magnetic field profile of a micron-scale current-carrying wire.

Towards the goal of eventually realizing nanoscale imaging at low temperature, we discuss in chapter 7 some of the directions for future effort. We discuss the possibilities and challenges towards single-NV magnetometry with the diamond nanobeams, possible configurations of nanoscale lift-height control via integration into tuning fork atomic force microscope structure, challenges on the sidewall roughness, as well as the sensing capabilities of group-IV color centers.

1

Introduction

Now we'll know,
Now you'll know what I am telling.

As can be inferred from the title, this thesis is about a very specific form of *magnetometer*: a device that measures the magnetic field. Long before even establishing any knowledge of what the magnetic field actually is, the history of magnetometers already started when the earliest form of a compass (*sinan*, "the governor of the south") was invented in ancient China around 2,000 years ago [1]. Built with a piece of magnetized lodestone, such a device can align itself with the earth's magnetic field, thereby "measuring" its orientation. In the 2,000 years that follow, development in science and technology has enabled people to build magnetometers in vastly different forms [2, 3], and precisely measure magnetic fields that are ~10,000,000,000 times weaker than the earth's magnetic field [4, 5].

The motivation of devoting such effort to measuring the magnetic field is usually the rich information that can be encoded in the magnetic field, rather than its exact value per se. In the case of the compass, that "information" is the geographical orientation associated with the earth's magnetic field. In modern-day research, magnetometry provides valuable information for a wide range of studies, including the history of rock formation [6], neuron activities in the brain [7], properties of astrophysical bodies [8], nanoscale condensed matter physics [9] and much more.

It is also the extremely wide range of application that gives rise to all the different forms of magnetometers, each developed and optimized for the specific environment of their intended application. Again taking the compass as an example, to function as a navigation tool for travellers, it needs to be a portable device that can measure the orientation of the earth's magnetic field under room temperature and atmospheric pressure. Therefore for this specific application, a 2-euro pocket compass is the better choice over a state-of-the-art superconducting quantum interference device (SQUID) [10] which works only at cryogenic temperatures, despite the latter being 10,000,000,000 times more sensitive.

The goal of this thesis is essentially under the same spirit: we aim to develop a magnetometer that is optimal for a specific working condition. Our *fiber-coupled diamond nanobeam* magnetometer aims to provide a solution for high-sensitivity, high-spatial-resolution magnetic field sensing in hard-to-reach environments, and facilitate the studies in e.g low-temperature quantum physics, in-cell biomagnetic phenomena and so on. The motivation of developing such devices will be elaborated in the following sections.

1.1. Nitrogen-vacancy centers as scanning-probe magnetometers

The magnetometer we aim to develop in this thesis is based on the nitrogen-vacancy (NV) center. This is an atomic structure that naturally exists in diamond, where two adjacent carbon atoms in the diamond lattice are replaced by a nitrogen atom and a lattice vacancy (fig. 1.1(a)). NV centers have been extensively studied since almost 50 years ago [11], and have nowadays become a well-established building block for quantum information processing [12–14] and quantum sensing [15–18].

Among all its applications, the NV center can function as a magnetometer due to
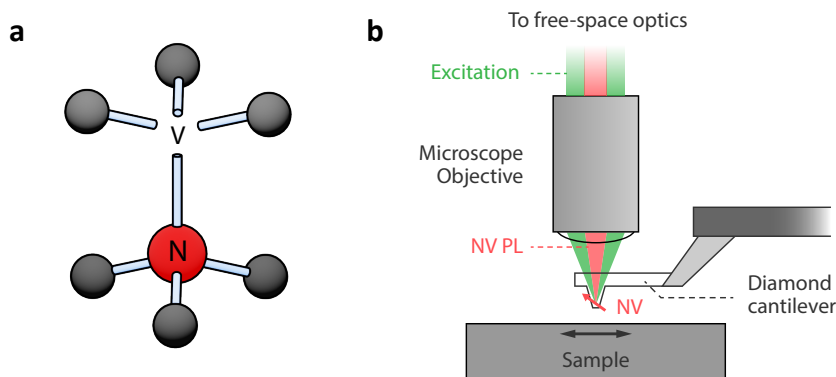
Figure 1.1 - **Scanning-probe magnetometry with NV centers. (a)** Atomic structure of an NV center in diamond. The nitrogen atom is colored in red and the surrounding carbon lattice in grey. **(b)** Schematics of a scanning-probe NV magnetometer. A single NV is placed at the apex of a diamond tip-on-cantilever structure, and is scanned across the target sample with the tip-sample distance controlled by a tuning-fork atomic force microscope (AFM) structure. The optical access to the NV center is provided by free-space optics.

the interaction between its intrinsic magnetic moment and the external magnetic field (known as the *Zeeman* interaction). Such interaction encodes the information of the external magnetic field in the transition frequencies between the NV center's quantum states. These transition frequencies can be read out optically via the light emission of the NV center upon laser excitation ("photoluminescence"), thereby allowing the optical readout of the magnetic field.

Since their first experimental demonstration [19, 20], NV magnetometers have found a wide range of applications thanks to their remarkable versatility. They can operate from (above) room temperature down to sub-kelvin cryogenic conditions [21–23], from vacuum to ambient conditions to extreme high-pressure environments [24], and in vastly different configurations from macroscopic endoscopes [25] to fluorescent nanocrystals injected into living cells [26].

And NV magnetometers are particularly interesting for physicists because of their capability of high-resolution magnetic *imaging*: Because they are *atomic* in size, the spatial profile of the external magnetic field can in principle be resolved and mapped out also with atomic resolution. This makes the NV center a powerful tool for studying condensed matter systems, where interesting physics happen on nanometer or even shorter length scales. Valuable insight on e.g. current distribution, magnetic domain structures and magnetic excitations can be extracted from the spatial profile of their associated magnetic field [9]. In the past decade, advances in NV magnetometry have led to numerous breakthroughs in revealing the nanoscale physics of condensed matter systems [27–30].

Yet you might have noticed the discrepancy in the choice of words, between the promised "atomic" spatial resolution and the "nanoscale" that is actually achievable. This is because the sensor size is not the only experimental factor that determines the spatial resolution. Especially for the previously mentioned application in condensed matter physics, we are ultimately interested in resolving the (electro-)magnetic phenomena *within* the studied sample with high resolution. And this is only possible if the magnetometer is in sufficiently *close proximity* to the sample. Therefore, the experimental limit of an NV magnetometer's spatial resolution in such measurements is actually set by the minimal NV-sample distance.

For exactly this reason, *scanning-probe* NV magnetometers have been proposed [31] and realized [32] to perform magnetic imaging with minimized NV-sample distance.   This is achieved by embedding a single NV center at the apex of a nano-fabricated diamond tip that is sub-micron in size (fig. 1.1(b)).   Precise mechanical control over the tip position allows the tip to be placed and scanned above the sample in nanometer proximity, thereby realizing nanoscale magnetic imaging with the NV center.

Like every technique, however, the scanning-probe NV magnetometer also has its constraints in terms of application. One aspect of the constraints is the optical access: As briefly mentioned previously, the NV center needs to be addressed and read out optically. In the scanning-probe scheme, this is achieved by using a microscope objective to focus a laser beam onto the NV center and collect its photoluminescence emission (fig. 1.1(b)). Yet having a microscope objective in the (usually sub-millimeter) vicinity of the probe and sample as well as directing a *free-space* laser beam onto the probe can be challenging in certain environments. Examples include low-temperature dilution refrigerators [33], inside biological tissues and so on. While these environments are hard for conventional NV magnetometers to reach, NV magnetometry can still provide valuable information if there is a way to implement it.

1.2. Towards a fiber-based NV scanning-probe

One possible way to overcome this challenge is to instead guide the excitation laser light and the NV photoluminescence with *optical fibers*.   This way, the implementation of NV magnetometry in previously mentioned environments can be facilitated by the flexibility of optical fibers, and the absence of free-space optical components in the vicinity of the sample.

Towards this goal, fiber-based NV magnetometers have been developed in various forms [25, 34, 35]. These devices consist of an NV-hosting diamond crystal fixed to one end of the optical fiber, allowing through-fiber excitation and readout of the NV centers. However, most of the existing fiber-based NV magnetometers are intended for magnetic characterization on a larger scale, and a similar solution for scanning-probe NV measurements on the nanoscale is not yet existent.

Therefore, the goal of this thesis is to tackle this exact challenge, by developing and demonstrating the *fiber-coupled diamond nanobeam* scanning-probe, illustrated in fig. 1.2.
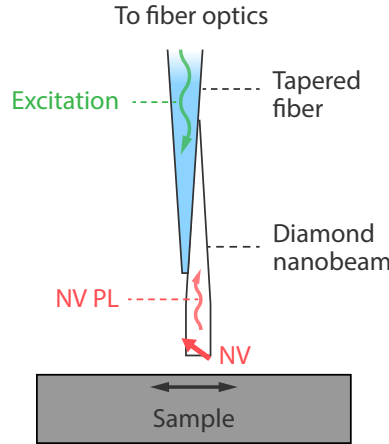
Figure 1.2 - **Schematics of a fiber-coupled diamond nanobeam scanning magnetometer.** An ensemble of NVs or a single NV is placed near the end facet of a diamond nanobeam, and is addressed through the tapered fiber interface. The target sample is mounted on a (nano-)positioner realize scanning-probe magnetic imaging.

Here, our NV-hosting diamond is fabricated into a "nanobeam" shape, the prefix "nano" referring to its sub-micron-sized cross section. The diamond nanobeam has a tapered profile and is coupled to an optical fiber that is also tapered at the end. This so called "adiabatic coupling" structure, widely used in nanophotonics as a fiber-coupling interface, ensures the efficient transfer of light signal via a *gradual* transition between the fiber and the diamond nanobeam [36–38]. With a natural scanning-probe geometry, the fiber-coupled diamond nanobeams hold the potential to realize nanoscale magnetic imaging in a similar way as the existing diamond tip solution, with enhanced accessibility to hard-to-reach environments provided by the all-fiber optical interface.

As physicists, our long-term motivation for developing the diamond nanobeam scanning-probe is, among all its potential applications, to facilitate NV magnetometry in the study of *low-temperature* physics on the nanoscale. This is where many interesting quantum phenomena - quantum Hall effect, superconductivity, quantum phase transitions, to name a few - take place [39, 40]. Compared to the low temperature implementation of existing scanning-probe NV magnetometers [23, 41, 42], the fiber-coupled diamond nanobeams could benefit from reduced heat load and easier alignment. Furthermore, towards even lower temperatures in the millikelvin regime where NV centers themselves tend to fail, the fiber-coupled diamond nanobeams could still be an excellent platform for exploring the sensing potential for group-IV color centers in diamond (e.g. the silicon-vacancy or tin-vacancy centers) that are more stable at these temperatures [43–45].

1

1.3. Thesis outline

This thesis focuses on the efforts of bringing fiber-coupled diamond nanobeam scanning-probes into reality. Instead of a compilation of my work during the PhD period, it is rather intended as a *handbook* for anyone who wishes to learn about or work on fiber-coupled diamond nanobeams. As such, its chapters are divided according to the different steps throughout the development and demonstration of these probes, and organized in their logical order.

Specifically, we start in chapter 2 by reviewing the theoretical foundations of this work. We will discuss the structure of NV centers in diamond, and how they can be used to accurately measure the magnetic field. We will also give a brief overview of the existing experimental configurations of NV magnetometry, from which we motivate the necessity to develop a fiber-based, scanning-probe NV magnetometer.

Starting from chapter 3, we dive into the experimental details of realizing the fiber-coupled diamond nanobeam probes. In this chapter, we go through the nanofabrication workflow of the diamond nanobeams. We fabricate free-hanging nanobeams from a single-crystal bulk diamond based on reactive ion etching, and show that the NV centers can be deterministically created at the beam tip through angled ion implantation.

Chapter 4 focuses on the process of coupling the fabricated nanobeam to the optical fibers. Two methods will be discussed: We first show that it is possible to directly use the tapered fiber to break the nanobeams off the diamond substrate, and achieve optical coupling in the same step. To increase the robustness of the assembly and rule out the randomness involved in the previous process, we then demonstrate the assembly workflow using optical glue. Using this approach, we realize a robust and transportable fiber-nanobeam probe with optimized optical coupling.

As a result of workflow evolution both in nanobeam fabrication and fiber coupling procedure, two generations of fiber-coupled diamond nanobeam probes have been developed through the course of the project: the first generation, "homogeneous-NV" probes consists of nanobeams with ensemble NVs distributed along the entire nanobeams and coupled through direct fiber break-off, and the second generation, "tip-NV" probes with deterministically implanted NVs at beam tip, and robustly glued to tapered fibers. In chapter 5, we demonstrate the through-fiber readout of NV photoluminescence for both generations, and estimate the coupling efficiencies at the fiber-nanobeam interface.

Then in chapter 6, we implement our two generations of devices in proof-of-principle magnetic imaging measurements. We show that we can image the spin waves in a thin magnet in one dimension, using the homogeneous-NV nanobeams as scanning probes. And with the tip-NV probes, we demonstrate 2D scanning-probe operation in sub-micron proximity to the sample surface, and image the magnetic field profile of a micron-scale current-carrying wire. We conclude this thesis in chapter 7, where we also discuss possible future efforts towards a fiber-based magnetometer at low temperature and with nanoscale spatial resolution.

References

[1] W. Lowrie. *Fundamentals of geophysics*. 2nd edition. Cambridge: Cambridge University Press, 2007.

[2] A. Grosz, M. J. Haji-Sheikh, and S. C. Mukhopadhyay. "High sensitivity magnetometers". In: *Smart Sensors, Measurement and Instrumentation*. Vol. 19. New York: Springer, 2016.

[3] M. W. Mitchell and S. Palacios Alvarez. "Colloquium: Quantum limits to the energy resolution of magnetic field sensors". In: *Reviews of Modern Physics* 92.2 (June 2020). ISSN: 15390756. DOI: 10.1103/REVMODPHYS.92.021001.

[4] H. B. Dang, A. C. Maloof, and M. V. Romalis. "Ultrahigh sensitivity magnetic field and magnetization measurements with an atomic magnetometer". In: *Applied Physics Letters* 97.15 (Oct. 2010). ISSN: 0003-6951. DOI: 10.1063/1.3491215.

[5] W. C. Griffith, S. Knappe, and J. Kitching. "Femtotesla atomic magnetometry in a microfabricated vapor cell". In: *Optics Express* 18.26 (Dec. 2010), p. 27167. ISSN: 1094-4087. DOI: 10.1364/OE.18.027167.

[6] L. V. de Groot, K. Fabian, A. Béguin, M. E. Kosters, D. Cortés-Ortuño, R. R. Fu, C. M. Jansen, R. J. Harrison, T. van Leeuwen, and A. Barnhoorn. "Micromagnetic tomography for paleomagnetism and rock-magnetism". In: *Journal of Geophysical Research: Solid Earth* 126.10 (Oct. 2021). ISSN: 21699356. DOI: 10.1029/2021JB022364.

[7] E. Boto, S. S. Meyer, V. Shah, O. Alem, S. Knappe, P. Kruger, T. M. Fromhold, M. Lim, P. M. Glover, P. G. Morris, R. Bowtell, G. R. Barnes, and M. J. Brookes. "A new generation of magnetoencephalography: Room temperature measurements using optically-pumped magnetometers". In: *NeuroImage* 149 (Apr. 2017), pp. 404–414. ISSN: 10538119. DOI: 10.1016/j.neuroimage.2017.01.034.

[8] C. S. Arridge, J. P. Eastwood, C. M. Jackman, G.-K. Poh, J. A. Slavin, M. F. Thomsen, N. André, X. Jia, A. Kidder, L. Lamy, A. Radioti, D. B. Reisenfeld, N. Sergis, M. Volwerk, A. P. Walsh, P. Zarka, A. J. Coates, and M. K. Dougherty. "Cassini in situ observations of long-duration magnetic reconnection in Saturn's magnetotail". In: *Nature Physics* 12.3 (Mar. 2016), pp. 268–271. ISSN: 1745-2473. DOI: 10.1038/nphys3565.

[9] F. Casola, T. Van Der Sar, and A. Yacoby. "Probing condensed matter physics with magnetometry based on nitrogen-vacancy centres in diamond". In: *Nature Reviews Materials* 3 (Jan. 2018). ISSN: 20588437. DOI: 10.1038/natrevmats.2017.88.

1

[10]   R. L. Fagaly. "Superconducting quantum interference device instruments and applications". In: *Review of Scientific Instruments* 77.10 (Oct. 2006). ISSN: 0034-6748. DOI: 10.1063/1.2354545.

[11]   G. Davis and M. F. Hamer. "Optical studies of the 1.945 eV vibronic band in diamond". In: *Proceedings of the Royal Society of London. A. Mathematical and Physical Sciences* 348.1653 (Feb. 1976), pp. 285–298. ISSN: 0080-4630. DOI: 10.1098/rspa.1976.0039.

[12]   W. Pfaff, B. J. Hensen, H. Bernien, S. B. van Dam, M. S. Blok, T. H. Taminiau, M. J. Tiggelman, R. N. Schouten, M. Markham, D. J. Twitchen, and R. Hanson. "Unconditional quantum teleportation between distant solid-state quantum bits". In: *Science* 345.6196 (Aug. 2014), pp. 532–535. ISSN: 0036-8075. DOI: 10.1126/science.1253512.

[13]   G. Waldherr, Y. Wang, S. Zaiser, M. Jamali, T. Schulte-Herbrüggen, H. Abe, T. Ohshima, J. Isoya, J. F. Du, P. Neumann, and J. Wrachtrup. "Quantum error correction in a solid-state hybrid spin register". In: *Nature* 506.7487 (Feb. 2014), pp. 204–207. ISSN: 0028-0836. DOI: 10.1038/nature12919.

[14]   M. Ruf, N. H. Wan, H. Choi, D. Englund, and R. Hanson. "Quantum networks based on color centers in diamond". In: *Journal of Applied Physics* 130.7 (Aug. 2021). ISSN: 0021-8979. DOI: 10.1063/5.0056534.

[15]   R. Schirhagl, K. Chang, M. Loretz, and C. L. Degen. "Nitrogen-vacancy centers in diamond: Nanoscale sensors for physics and biology". In: *Annual Review of Physical Chemistry* 65 (2014), pp. 83–105. ISSN: 0066426X. DOI: 10.1146/annurev-physchem-040513-103659.

[16]   F. Dolde, H. Fedder, M. W. Doherty, T. Nöbauer, F. Rempp, G. Balasubramanian, T. Wolf, F. Reinhard, L. C. L. Hollenberg, F. Jelezko, and J. Wrachtrup. "Electric-field sensing using single diamond spins". In: *Nature Physics* 7.6 (June 2011), pp. 459–463. ISSN: 1745-2473. DOI: 10.1038/nphys1969.

[17]   V. M. Acosta, E. Bauch, M. P. Ledbetter, A. Waxman, L.-S. Bouchard, and D. Budker. "Temperature dependence of the nitrogen-vacancy magnetic resonance in diamond". In: *Physical Review Letters* 104.7 (Feb. 2010), p. 070801. ISSN: 0031-9007. DOI: 10.1103/PhysRevLett.104.070801.

[18]   J. Teissier, A. Barfuss, P. Appel, E. Neu, and P. Maletinsky. "Strain coupling of a nitrogen-vacancy center spin to a diamond mechanical oscillator". In: *Physical Review Letters* 113.2 (July 2014), p. 020503. ISSN: 0031-9007. DOI: 10.1103/PhysRevLett.113.020503.

[19]   G. Balasubramanian, I. Y. Chan, R. Kolesov, M. Al-Hmoud, J. Tisler, C. Shin, C. Kim, A. Wojcik, P. R. Hemmer, A. Krueger, T. Hanke, A. Leitenstorfer, R. Bratschitsch, F. Jelezko, and J. Wrachtrup. "Nanoscale imaging magnetometry with diamond spins under ambient conditions". In: *Nature* 455.7213 (Oct. 2008), pp. 648–651. ISSN: 0028-0836. DOI: 10.1038/nature07278.

1

[20] J. R. Maze, P. L. Stanwix, J. S. Hodges, S. Hong, J. M. Taylor, P. Cappellaro, L. Jiang, M. V. G. Dutt, E. Togan, A. S. Zibrov, A. Yacoby, R. L. Walsworth, and M. D. Lukin. "Nanoscale magnetic sensing with an individual electronic spin in diamond". In: *Nature* 455.7213 (Oct. 2008), pp. 644–647. ISSN: 0028-0836. DOI: 10.1038/nature07279.

[21] M. C. Cambria, G. Thiering, A. Norambuena, H. T. Dinani, A. Gardill, I. Kemeny, V. Lordi, Á. Gali, J. R. Maze, and S. Kolkowitz. "Physically motivated analytical expression for the temperature dependence of the zero-field splitting of the nitrogen-vacancy center in diamond". In: *Physical Review B* 108.18 (Nov. 2023), p. L180102. ISSN: 2469-9950. DOI: 10.1103/PhysRevB.108.L180102.

[22] J. Happacher, J. Bocquel, H. T. Dinani, M. A. Tschudin, P. Reiser, D. A. Broadway, J. R. Maze, and P. Maletinsky. "Temperature-dependent photophysics of single NV centers in diamond". In: *Physical Review Letters* 131.8 (Aug. 2023), p. 086904. ISSN: 0031-9007. DOI: 10.1103/PhysRevLett.131.086904.

[23] P. J. Scheidegger, S. Diesch, M. L. Palm, and C. L. Degen. "Scanning nitrogen-vacancy magnetometry down to 350 mK". In: *Applied Physics Letters* 120.22 (May 2022). ISSN: 0003-6951. DOI: 10.1063/5.0093548.

[24] P. Bhattacharyya, W. Chen, X. Huang, S. Chatterjee, B. Huang, B. Kobrin, Y. Lyu, T. J. Smart, M. Block, E. Wang, Z. Wang, W. Wu, S. Hsieh, H. Ma, S. Mandyam, B. Chen, E. Davis, Z. M. Geballe, C. Zu, V. Struzhkin, R. Jeanloz, J. E. Moore, T. Cui, G. Galli, B. I. Halperin, C. R. Laumann, and N. Y. Yao. "Imaging the Meissner effect in hydride superconductors using quantum sensors". In: *Nature* 627.8002 (Mar. 2024), pp. 73–79. ISSN: 0028-0836. DOI: 10.1038/s41586-024-07026-7.

[25] G. Chatzidrosos, J. S. Rebeirro, H. Zheng, M. Omar, A. Brenneis, F. M. Stürner, T. Fuchs, T. Buck, R. Rölver, T. Schneemann, P. Blümler, D. Budker, and A. Wickenbrock. "Fiberized diamond-based vector magnetometers". In: *Frontiers in Photonics* 2 (Aug. 2021). DOI: 10.3389/fphot.2021.732748.

[26] L. Nie, A. C. Nusantara, V. G. Damle, M. V. Baranov, M. Chipaux, C. Reyes-San-Martin, T. Hamoh, C. P. Epperla, M. Guricova, P. Cigler, G. van den Bogaart, and R. Schirhagl. "Quantum sensing of free radicals in primary human dendritic cells". In: *Nano Letters* 22.4 (Feb. 2022), pp. 1818–1825. ISSN: 1530-6984. DOI: 10.1021/acs.nanolett.1c03021.

[27] I. Gross, W. Akhtar, V. Garcia, L. J. Martínez, S. Chouaieb, K. Garcia, C. Carrétéro, A. Barthélémy, P. Appel, P. Maletinsky, J. V. Kim, J. Y. Chauleau, N. Jaouen, M. Viret, M. Bibes, S. Fusil, and V. Jacques. "Real-space imaging of non-collinear antiferromagnetic order with a single-spin magnetometer". In: *Nature* 549.7671 (Sept. 2017), pp. 252–256. ISSN: 14764687. DOI: 10.1038/nature23656.

[28] L. Thiel, Z. Wang, M. A. Tschudin, D. Rohner, I. Gutiérrez-Lezama, N. Ubrig, M. Gibertini, E. Giannini, A. F. Morpurgo, and P. Maletinsky. "Probing magnetism in 2D materials at the nanoscale with single-spin microscopy". In: *Science* 364.6444 (June 2019), pp. 973–976. ISSN: 0036-8075. DOI: 10.1126/science.aav6926.

[29] Q.-C. Sun, T. Song, E. Anderson, A. Brunner, J. Förster, T. Shalomayeva, T. Taniguchi, K. Watanabe, J. Gräfe, R. Stöhr, X. Xu, and J. Wrachtrup. "Magnetic domains and domain wall pinning in atomically thin CrBr3 revealed by nanoscale imaging". In: *Nature Communications* 12.1 (Mar. 2021), p. 1989. ISSN: 2041-1723. DOI: 10.1038/s41467-021-22239-4.

[30] B. G. Simon, S. Kurdi, H. La, I. Bertelli, J. J. Carmiggelt, M. Ruf, N. De Jong, H. Van Den Berg, A. J. Katan, and T. Van Der Sar. "Directional excitation of a high-density magnon gas using coherently driven spin waves". In: *Nano Letters* 21.19 (Oct. 2021), pp. 8213–8219. ISSN: 15306992. DOI: 10.1021/acs.nanolett.1c02654.

[31] C. L. Degen. "Scanning magnetic field microscope with a diamond single-spin sensor". In: *Applied Physics Letters* 92.24 (June 2008), p. 243111. ISSN: 0003-6951. DOI: 10.1063/1.2943282.

[32] P. Maletinsky, S. Hong, M. S. Grinolds, B. Hausmann, M. D. Lukin, R. L. Walsworth, M. Loncar, and A. Yacoby. "A robust scanning diamond sensor for nanoscale imaging with single nitrogen-vacancy centres". In: *Nature Nanotechnology* 7.5 (2012), pp. 320–324. ISSN: 17483395. DOI: 10.1038/nnano.2012.50.

[33] H. Zu, W. Dai, and A. de Waele. "Development of dilution refrigerators—A review". In: *Cryogenics* 121 (Jan. 2022), p. 103390. ISSN: 00112275. DOI: 10.1016/j.cryogenics.2021.103390.

[34] I. V. Fedotov, L. V. Doronina-Amitonova, D. A. Sidorov-Biryukov, N. A. Safronov, S. Blakley, A. O. Levchenko, S. A. Zibrov, A. B. Fedotov, S. Y. Kilin, M. O. Scully, V. L. Velichansky, and A. M. Zheltikov. "Fiber-optic magnetic-field imaging". In: *Optics Letters* 39.24 (Dec. 2014), p. 6954. ISSN: 0146-9592. DOI: 10.1364/ol.39.006954.

[35] S. Dix, D. Lönard, I. C. Barbosa, J. Gutsche, J. Witzenrath, and A. Widera. "A miniaturized magnetic field sensor based on nitrogen-vacancy centers". In: *arXiv:2402.19372* (Feb. 2024). URL: https://arxiv.org/abs/2402.19372.

[36] S. Gröblacher, J. T. Hill, A. H. Safavi-Naeini, J. Chan, and O. Painter. "Highly efficient coupling from an optical fiber to a nanoscale silicon optomechanical cavity". In: *Applied Physics Letters* 103.18 (Oct. 2013). ISSN: 00036951. DOI: 10.1063/1.4826924.

[37] T. G. Tiecke, K. P. Nayak, J. D. Thompson, T. Peyronel, N. P. de Leon, V. Vuletić, and M. D. Lukin. "Efficient fiber-optical interface for nanophotonic devices". In: *Optica* 2.2 (Feb. 2015), p. 70. ISSN: 23342536. DOI: 10.1364/optica.2.000070.

[38] M. J. Burek, C. Meuwly, R. E. Evans, M. K. Bhaskar, A. Sipahigil, S. Meesala, B. MacHielse, D. D. Sukachev, C. T. Nguyen, J. L. Pacheco, E. Bielejec, M. D. Lukin, and M. Lončar. "Fiber-coupled diamond quantum nanophotonic interface". In: *Physical Review Applied* 8.2 (Aug. 2017). ISSN: 23317019. DOI: 10.1103/PhysRevApplied.8.024026.

[39] A. Uri, Y. Kim, K. Bagani, C. K. Lewandowski, S. Grover, N. Auerbach, E. O. Lachman, Y. Myasoedov, T. Taniguchi, K. Watanabe, J. Smet, and E. Zeldov. "Nanoscale imaging of equilibrium quantum Hall edge currents and of the magnetic monopole response in graphene". In: *Nature Physics* 16.2 (Feb. 2020), pp. 164–170. ISSN: 17452481. DOI: 10.1038/s41567-019-0713-3.

[40] D. Roditchev, C. Brun, L. Serrier-Garcia, J. C. Cuevas, V. H. L. Bessa, M. V. Miloševi, F. Debontridder, V. Stolyarov, and T. Cren. "Direct observation of Josephson vortex cores". In: *Nature Physics* 11.4 (Apr. 2015), pp. 332–337. ISSN: 17452481. DOI: 10.1038/nphys3240.

[41] M. Pelliccione, A. Jenkins, P. Ovartchaiyapong, C. Reetz, E. Emmanouilidou, N. Ni, and A. C. Bleszynski Jayich. "Scanned probe imaging of nanoscale magnetism at cryogenic temperatures with a single-spin quantum sensor". In: *Nature Nanotechnology* 11.8 (Aug. 2016), pp. 700–705. ISSN: 17483395. DOI: 10.1038/nnano.2016.68.

[42] S. Chen, S. Park, U. Vool, N. Maksimovic, D. A. Broadway, M. Flaks, T. X. Zhou, P. Maletinsky, A. Stern, and B. I. H. A. Yacoby. "Current induced hidden states in Josephson junctions". In: *arXiv:2402.02472* (Feb. 2024). URL: https://arxiv.org/abs/2402.02472.

[43] A. E. Rugar, S. Aghaeimeibodi, D. Riedel, C. Dory, H. Lu, P. J. McQuade, Z.-X. Shen, N. A. Melosh, and J. Vučković. "Quantum photonic interface for tin-vacancy centers in diamond". In: *Physical Review X* 11.3 (July 2021), p. 031021. ISSN: 2160-3308. DOI: 10.1103/PhysRevX.11.031021.

[44] L. De Santis, M. E. Trusheim, K. C. Chen, and D. R. Englund. "Investigation of the Stark effect on a centrosymmetric quantum emitter in diamond". In: *Physical Review Letters* 127.14 (Sept. 2021), p. 147402. ISSN: 0031-9007. DOI: 10.1103/PhysRevLett.127.147402.

[45] E. I. Rosenthal, C. P. Anderson, H. C. Kleidermacher, A. J. Stein, H. Lee, J. Grzesik, G. Scuri, A. E. Rugar, D. Riedel, S. Aghaeimeibodi, G. H. Ahn, K. Van Gasse, and J. Vučković. "Microwave spin control of a tin-vacancy qubit in diamond". In: *Physical Review X* 13.3 (Aug. 2023), p. 031022. ISSN: 2160-3308. DOI: 10.1103/PhysRevX.13.031022.

2

Nitrogen-vacancy centers in diamond: Theory and application

This particular diamond was extra special.

Everglow · Coldplay

Abstract

In this chapter, we discuss the basic properties of NV centers. Section 2.1 explains the atomic and electronic structure of NV centers in diamond, and introduces the electron spin resonance (ESR) measurement, which will be used to characterize the NV centers experimentally throughout the entire thesis. Section 2.2 discusses the principles of NV magnetometry based on the Zeeman splitting of NV spin states, followed by a brief discussion on the methods to implement NV magnetometry experimentally in section 2.3. Based on this discussion, in section 2.4 we motivate fiber-based NV magnetometry, and introduce the concept of fiber-coupled diamond nanobeams. We explain how such a configuration can function as an all-fiber scanning probe magnetometer, and facilitate high spatial resolution magnetometry measurements in hard-to-reach environments.

Introduction

The central goal of this thesis is to develop a fiber-based, scanning-probe magnetometer using nitrogen-vacancy (NV) centers in diamond nanobeams. The aim of this chapter is then to explain how such a magnetometer works, and justify why we need it. In sections 2.1 and 2.2, we formulate the theoretical foundation of this thesis: How we can measure the external magnetic field via the electron-spin resonance of NV centers. Based on this, we discuss in section 2.3 the strengths and limitations of existing experimental methods of NV magnetometry, and motivate fiber-based scanning-NV magnetometry in section 2.4 based on the discussion.

2.1. Nitrogen-vacancy centers in diamond

The magnetic field sensing capabilities of the NV center are a result of its *electronic* properties. Therefore to formulate an understanding of the latter, in this section we start by explaining the electron configuration of an NV center, and how this configuration leads to its well-known spin-1 behavior (eq. (2.3)). This provides the basis for understanding the subsequent discussion on state dynamics of the NV center, and the physics of NV magnetic sensing.

2.1.1. The NV$^-$ ground state

The nitrogen-vacancy (NV) center in diamond consists of a nitrogen atom replacing the carbon atom in the diamond lattice, and a lattice vacancy in its adjacent site (fig. 2.1(a)). Specifically, most applications of NV centers are based on the *negatively* charged NV center noted as NV$^-$. Throughout this thesis, the term "NV center" will be referring to NV$^-$, apart from where the effect of the *neutral* NV^0 charge state is explicitly studied.

The NV$^-$ center consists of 6 electrons in total: 3 from the dangling bonds of the 3 carbon atoms adjacent to the vacancy, 2 from the dangling bonds of the nitrogen atom, and 1 extra captured from the lattice, resulting in a net charge of -1e. Theoretical analysis [1–3] shows that the ground state of this six-electron system consists of 4 electrons paired up in the two a_1 orbitals and 2 unpaired electron in separate $e_{x,y}$ orbitals (fig. 2.1(b)), forming a spin-1 system.

In the absence of external interrogation (electric/magnetic field, nearby charges/spins, etc.), the NV ground state is dominated by the dipolar spin-spin interaction between the 2 unpaired electrons. Based on this, the NV ground state Hamiltonian can be determined following the approach in Ivády et al. [4], which we briefly elaborate as follows.

The spin-spin interaction can be expressed in the standard form of magnetic dipolar interaction

$$\frac{H_{\text{GS}}}{h} = -\frac{\mu_0}{4\pi} \frac{\gamma^2}{r^3} \left(3(\mathbf{s}_1 \cdot \hat{\mathbf{r}})(\mathbf{s}_2 \cdot \hat{\mathbf{r}}) - \mathbf{s}_1 \cdot \mathbf{s}_2\right), \tag{2.1}$$

where $\mathbf{s}_1$, $\mathbf{s}_2$ are the spin-1/2 operators for the two spins, $\mathbf{r}$ denotes their distance with $r = |\mathbf{r}|$, $\hat{\mathbf{r}} = \mathbf{r}/r$, μ_0 is the vacuum permeability and $\gamma = g\mu_B/h = 28\,\text{GHz/T}$ is the
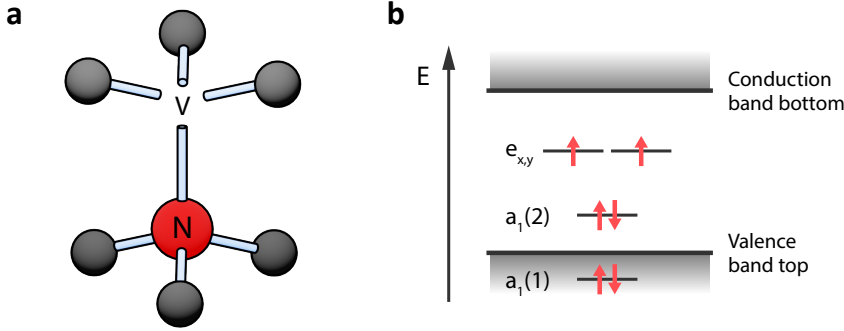
Figure 2.1 - **NV center in diamond.** **(a)** Atomic structure of the NV center. The nitrogen atom is colored in red and the surrounding carbon lattice in grey. **(b)** Simplified electronic structure of the NV center. The single-electron orbitals and their energy levels with respect to the diamond band gap are plotted, together with the occupation of electrons for the ground state of NV⁻. Directions of the arrows indicate spin up/down. The unpaired spins in the $e_{x,y}$ orbitals give rise to the spin-1 behavior of NV⁻. Notation of the orbitals follows ref.[1].

electron gyromagnetic ratio, with $g \approx 2$ being the electron Landé factor, h the Planck constant and μ_B the Bohr magneton. We note that strictly speaking, here the Landé factor should take the value of electrons in the NV center instead of free electrons, yet it's been experimentally demonstrated [5] that these two values are sufficiently close for us to neglect this difference in the rest of this thesis.

This Hamiltonian can be transformed from the basis of two separate spins $|s_1, m_{s,1}; s_2, m_{s,2}\rangle$ into the basis of the *total* spin $|S, m_S\rangle$, and be written in the general form of

$$\frac{H_{\mathrm{GS}}}{h} = \mathbf{S}^T \hat{D} \mathbf{S}. \tag{2.2}$$

Here the total spin operator $\mathbf{S} = \mathbf{s}_1 + \mathbf{s}_2 = (S_x, S_y, S_z)$ becomes a spin-1 operator, in the form of 3×3 Pauli matrices. The specific matrix elements of the *zero-field splitting (ZFS) tensor* $\hat{D}$ represent the expectation values of the dipolar energy, and can be determined via the formalism elaborated in refs. [6, 7]. Under the C_{3v} symmetry of the NV center, the general Hamiltonian can be simplified down to

$$\frac{H_{\mathrm{GS}}}{h} = D\left(S_z^2 - \frac{2}{3}\right), \tag{2.3}$$

where the quantization axis z aligns with the C_3 rotation axis, i.e. the N→V axis, and the ZFS tensor reduces to the ZFS *constant* D.

Equation (2.3) pictures the spin-triplet structure of the NV ground state, consisting of the energy-degenerate $|m_S = \pm 1\rangle$ states and the $|m_S = 0\rangle$ state lower in energy by $D = 2.87\,\mathrm{GHz}$ (determined experimentally).

2.1.2. State dynamics and spin-dependent photoluminescence of NV$^-$

The optical excitation and subsequent spin-dependent photoluminescence of NV centers lies at the heart of their applications. In this section, we will discuss the state dynamics of NV centers under optical excitation, and the principles of electron spin resonance (ESR) measurements.
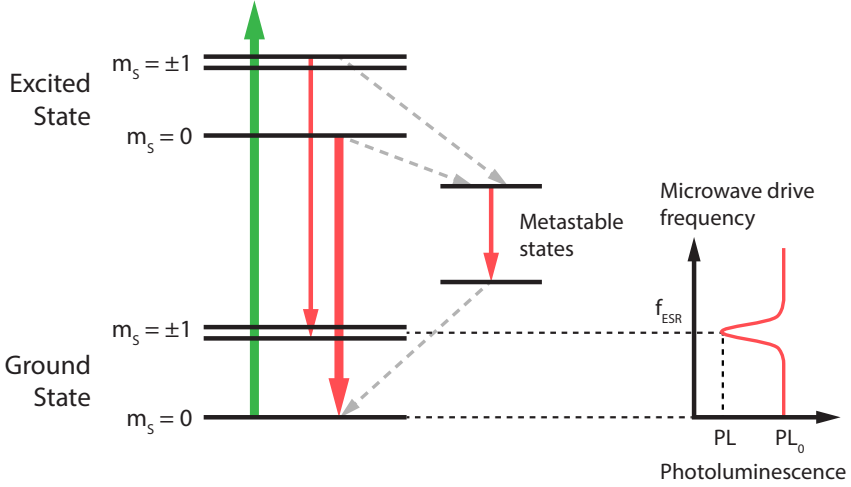
Figure 2.2 - **Energy level diagram and electron spin resonance (ESR) measurement of the NV center.** The green arrow represents off-resonant excitation, and subsequent photoluminescence is denoted in red arrows with the thickness indicating the intensity difference between $|m_S = \pm1\rangle$ states and $|m_S = 0\rangle$ state. Grey dashed arrows denote the non-radiative transitions to/from the metastable states. The right part of the figure plots the response of NV photoluminescence when microwave drive is frequency-swept near the $|m_S = 0\rangle \rightarrow |m_S = \pm1\rangle$ transition.

From the ground state triplet, the optical excitation of NV centers is often achieved off-resonantly with a green laser (usually 520 or 532 nm) in experiments. At single-electron level, the excitation process corresponds to one electron in the $a_1(2)$ orbital (fig. 2.1) being optically excited to one of the $e_{x,y}$ orbitals [8]. The choice of green laser excitation is a consideration balancing the wavelength dependence of excitation efficiency and (unwanted) photo-induced ionization rate [9].

At room temperature, the first excited state of the NV center can also be approximated as a spin-triplet [10], depicted in fig. 2.2. One important property of the optical transitions between the ground state and the first excited state is that they do not flip the spin, i.e. the quantum number m_S is preserved. As a result, optical excitation-decay cycle should not change the population over spin states (Even in presence of vibrational interactions [11]). However, there also exists an alternative decay path through the *metastable states* (Corresponding to the six electrons occupying the single-electron orbitals in a different configuration

compared to fig. 2.1 [1]). The non-radiative and non-spin-preserving transition $|m_S = \pm 1\rangle \rightarrow |m_S = 0\rangle$, indicated by the dashed grey arrows in fig. 2.2, is then made possible via these metastable states as a result of *spin-orbit* interaction [11]. Furthermore, the $|m_S = \pm 1\rangle$ states have a higher probability of decaying through the metastable states compared to $|m_S = 0\rangle$, and are therefore lower in photoluminescence intensity upon continuous excitation (hence being referred to as the "dark states").

The above mentioned state dynamics yield two consequences. Firstly, the presence of the $|m_S = \pm 1\rangle \rightarrow |m_S = 0\rangle$ transition and the absence of the reverse process result in the *optical pumping* effect: Under continuous excitation, the spin state of the NV center will be "pumped" from thermal equilibrium to polarized occupation of $|m_S = 0\rangle$ only [1]. Secondly, the difference in PL intensity enables the optical readout of the NV spin state, referred to as *optically-detected magnetic resonance* (ODMR).

The combination of the two allows the experimental determination of the $|m_S = 0\rangle \rightarrow |m_S = \pm 1\rangle$ transition frequencies, known as the *electron spin resonance* (ESR) frequencies. The continuous-wave (CW) ESR measurement uses a CW laser to pump the NV center into the $|m_S = 0\rangle$ state, and applies a microwave at the ESR frequency to trigger the $|m_S = 0\rangle \rightarrow |m_S = \pm 1\rangle$ transition. This results in a decrease of measured PL intensity. The PL intensity as a function of applied microwave frequency is plotted in fig. 2.2, and will be referred to as the *ESR spectrum* for the rest of the thesis.

2.2. Magnetic field sensing with NV centers

The state dynamics described in the previous sections enable the optical readout of the NV-ESR frequencies. In this section, we describe how the ESR frequencies encode information of the external magnetic field experienced by the NV center, making it a promising magnetometer at the atomic scale.

2.2.1. Extracting the external magnetic field from the NV ESR frequencies

When the NV center experiences an external magnetic field **B**, the energy degeneracy of the $|m_S = \pm 1\rangle$ spin states will be lifted as a result of reduced symmetry. The change in ESR frequencies therefore encodes information of the external field, elaborated as follows.

The presence of **B** adds an additional Zeeman term to the ground state Hamiltonian eq. (2.3):

$$\frac{H_{\mathrm{GS}}}{h} = D\left(S_z^2 - \frac{2}{3}\right) + \gamma \mathbf{B} \cdot \mathbf{S}, \tag{2.4}$$

---

[1] We note here that for the non-resonant excitation scheme, experiments indicate that the aforementioned spin-preserving properties of the optical transitions do not hold strictly [12], while the effect of optical pumping remains intact and the picture of state dynamics in fig. 2.2 remains a valid approximation in practice.

where γ is again the electron gyromagnetic ratio. Note that compared to the case of a real-world NV center, we still ignored the possible presence of an external electric field or strain.

For brevity, we define the angle θ between the external field $\mathbf{B}$ and the NV axis (i.e. the z axis)

$$\cos\theta = \frac{\mathbf{B}\cdot\hat{\mathbf{z}}}{|\mathbf{B}|} \qquad (2.5)$$

and, without loss of generality given the symmetry of the system, further set the orientation of the x axis such that $\mathbf{B}$ lies in the xz plane:

$$\mathbf{B} = B(\hat{\mathbf{z}}\cos\theta + \hat{\mathbf{x}}\sin\theta) \qquad (2.6)$$

with $B = |\mathbf{B}|$. Substituting in the expressions of the spin-1 Pauli matrices, we write eq. (2.4) in matrix form:

$$\frac{H_{\text{GS}}}{h} = \begin{pmatrix} D/3 + \gamma B\cos\theta & \gamma B\sin\theta/\sqrt{2} & 0 \\ \gamma B\sin\theta/\sqrt{2} & -2D/3 & \gamma B\sin\theta/\sqrt{2} \\ 0 & \gamma B\sin\theta/\sqrt{2} & D/3 - \gamma B\cos\theta \end{pmatrix}. \qquad (2.7)$$

By diagonalizing eq. (2.7), we can extract the eigenfrequencies $\{f_1, f_2, f_3\}$ of the system, corresponding to the energies of $|m_S = 0\rangle$ and $|m_S = \pm 1\rangle$ respectively. The lower/upper ESR frequencies are then $f_l = f_3 - f_1$, $f_u = f_2 - f_1$, both functions of B and θ. This is depicted in fig. 2.3(b).

When $\mathbf{B}$ aligns with the NV orientation, i.e. $\theta = 0$, the Zeeman splitting is linear and results in

$$f_{u/l} = D \pm \gamma B. \qquad (2.8)$$

For non-zero misalignment $\theta \neq 0$, the shift in ESR frequencies becomes non-linear and the energy splitting $f_u - f_l$ at the same field amplitude also decreases compared to the aligned scheme. Yet from fig. 2.3, it is worth noting that this splitting does not go to 0 when $\theta = 90°$. In other words, $f_u - f_l$ is a function of both B and $\cos\theta$, instead of solely the field projection on NV axis ($B\cos\theta$).

This actually allows the determination of both the amplitude of the external field and its orientation with respect to the NV axis, through the pair of ESR frequencies $f_u(B, \theta)$ and $f_l(B, \theta)$. In practice, this is achieved through the reverse relations $B(f_u, f_l)$ and $\cos\theta(f_u, f_l)$:

$$B(f_u, f_l) = \frac{1}{\sqrt{3}\gamma}\sqrt{f_u^2 + f_l^2 - f_u f_l - D^2}, \qquad (2.9)$$

$$\cos\theta(f_u, f_l) = \frac{-(f_u + f_l)^3 + 3(f_u^3 + f_l^3) + 2D^3}{27D(\gamma B)^2} + \frac{1}{3}. \qquad (2.10)$$

The above equations further make *vector* magnetometry possible: As there are 4 possible NV orientations in the diamond lattice ($\langle 111 \rangle / \langle \bar{1}11 \rangle / \langle 1\bar{1}1 \rangle / \langle 11\bar{1} \rangle$, corresponding to the 4 possible orientations of C-C covalence bonds), the vector

a

2

b
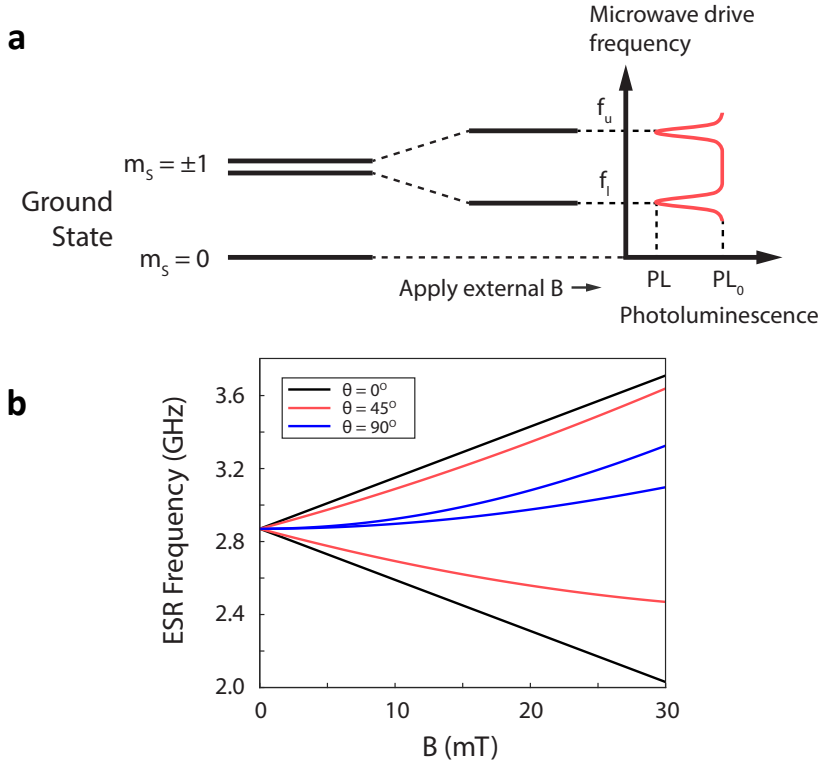
Figure 2.3 - **The NV ESR transitions in presence of external magnetic field.** **(a)** Zeeman splitting of $|m_S = \pm 1\rangle$ states, and corresponding ESR spectrum. The degenerate $|m_S = \pm 1\rangle$ states at zero field are drawn with a separation solely to indicate the presence of two states. **(b)** Calculated ESR frequencies f_l and f_u as a function of external field amplitude B, at different angle θ between the orientation of **B** and the NV axis.

orientation of the external magnetic field $\hat{\mathbf{n}}_B$ can be (over-)determined by measuring the ESR frequencies of an NV ensemble, through the set of equations

$$\cos\theta_i = \hat{\mathbf{n}}_B \cdot \hat{\mathbf{n}}_{\mathrm{NV},i}, \tag{2.11}$$

where $i = 1 \sim 4$ denotes the 4 NV orientations, $\hat{\mathbf{n}}_{\mathrm{NV},i}$ are the (known) unit vectors of the ith NV orientation, and θ_i is the relative angle between **B** and the ith NV orientation as determined from the ESR frequencies using eq. (2.10).

In practice, however, the possibility of measuring the full vector orientation of an external magnetic field using CW-ESR is constrained to a finite range of magnetic field amplitude. On the one hand, the minimum measurable magnetic field is determined by the sensitivity of the NVs and the measurement setup. This will be discussed in more detail in section 2.2.2. On the other hand, a large off-axis

(i.e. $\theta \neq 0$) magnetic field is also known to *quench* the photoluminescence and ESR contrast of the NVs [13]. This is because under such condition, the Hamiltonian eq. (2.4) will be dominated by the Zeeman term and the $|m_S\rangle$ states can no longer hold as the eigenstates of the system. The ODMR properties of NV centers based on these states will therefore also not be valid any more. Also that within this finite range, the extracted vector magnetic field is still ambiguous due to the spatial symmetry of the diamond lattice, and therefore requires further confirmation on the experimental settings to determine the correct orientation.

2.2.2. Magnetic field sensitivity of CW-ESR measurements

One important figure-of-merit for magnetometers is the magnetic field sensitivity. To gain insight into the sensitivity of NV magnetometers, in this section we consider the CW-ESR measurement (as in fig. 2.3) of a single NV center (or an ensemble of NVs in the same orientation) parallel to the field orientation, and discuss the magnetic field sensitivity of such measurements.

Since the external magnetic field aligns with the NV axis, we can determine the external field through the frequency shift of a single ESR dip: $B = (f_u - D)/\gamma$ (eq. (2.8)). The ESR spectrum of this dip can be described by a Lorentzian line shape:

$$I(f) = I_0 \left(1 - \frac{C(\Delta f/2)^2}{(f - f_u)^2 + (\Delta f/2)^2} \right), \tag{2.12}$$

in which a few important parameters for the ESR spectrum is defined:

- **PL intensity** I_0**:** The detected photoluminescence (s^{-1}) in absence of a microwave drive, or when the microwave is off-resonant. Corresponds to PL_0 in fig. 2.3.

- **ESR contrast** C**:** Relative change of PL intensity at ESR frequency f_u, defined as $C = (I_0 - I(f_u))/I_0$. (Or alternatively $C = (PL_0 - PL)/PL_0$, following the notation in fig. 2.3.)

- **Full width at half maximum (FWHM)** Δf**:** Linewidth of the dip, defined as $\Delta f = f_+ - f_-$, where $I(f_+) = I(f_-) = I_0(1 - C/2)$.

Apart from intrinsic properties of the NV(s) [14], the main experimental factors that determine the above parameters are the optical excitation power P_{opt} and the microwave drive power P_{mw}. Specifically:

- $I_0 = N\Gamma_{single}$, with N being the number of NVs addressed and Γ_{single} the single NV PL intensity. Γ_{single} follows a saturation behavior as a function of P_{opt}, and is limited by the optical collection efficiency in practice. This will be discussed more extensively in section 5.2.2.

- The dependence of both C and Δf on optical and microwave power is discussed in details in ref. [15]. Intuitively, P_{mw} drives the system from $|m_S = 0\rangle \rightarrow |m_S = \pm 1\rangle$ and therefore increases the contrast at resonance , P_{opt}

on the other hand effectively drives the system back $|m_S = \pm 1\rangle \rightarrow |m_S = 0\rangle$ through optical pumping, decreasing the contrast as a result. And the linewidth Δf increases with both P_{opt} and P_{mw}.

The magnetic field sensitivity of CW-ESR measurements can be extracted from these parameters. In general terms, *sensitivity* is defined as the minimum detectable signal that yields a signal-to-noise ratio (SNR) of 1 in unit time [16]. For CW-ESR measurements, the maximum sensitivity is achieved by measuring the variation of PL intensity at the maximum slope of $I(f)$. Assuming the readout noise of PL intensity I_0 is dominated by shot noise and therefore scales as $\sqrt{I_0}$, the magnetic field sensitivity η_B can be estimated as [15]:

$$\eta_B = \frac{4}{3\sqrt{3}\gamma} \frac{\Delta f}{C\sqrt{I_0}}. \tag{2.13}$$

It is then obvious from eq. (2.13) that CW-ESR sensitivity improves by increasing the total signal (therefore the amount of NVs addressed), ESR contrast, and decreasing the linewidth. Aside from optimizing these parameters via tuning the optical and microwave powers, the sensitivity of NV centers may be improved on a more fundamental level by e.g. switching to pulsed-ESR measurements, or improving upon the coherence time of the NVs [14, 15].

2.3. Experimental methods of magnetic imaging using NV centers

Due to their small (atomic if using single NV) sensing volume, NV centers hold potential for *imaging* magnetic fields at high spatial resolution. To realize such potential, however, is not trivial and requires effort on experimental implementation. Ever since the first experimental demonstration of NV magnetometry [17, 18], various experimental configurations have been exploited to harness the imaging potential of NV centers, applied in research ranging from biochemistry to condensed matter physics [19–24].

In this section, we briefly discuss two of the most commonly used experimental configurations for NV magnetic imaging, along with their strengths and limitations in real-world applications.

2.3.1. Diamond-on-chip: confocal microscopy with ensemble NVs

In the diamond-on-chip setting, the NV-hosting bulk diamond is directly stacked on top of the sample to be measured. A layer of ensemble NVs is created underneath the diamond surface that is in contact with the sample, with the NV depth and density chosen according to specific experimental needs. The excitation laser is focused onto the NV layer through a free-space microscope objective, addressing the NV centers at the focal spot and subsequently collecting the PL of these NV centers.

To realize imaging, the diamond-sample stack is scanned with respect to the laser spot by either scanning the laser spot (as in the setup discussed in section 3.2.3)

2
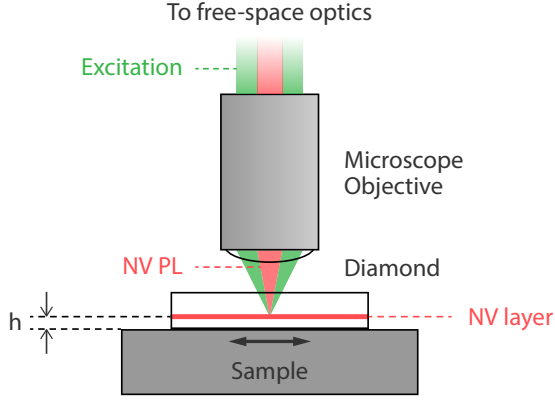
Figure 2.4 - **Schematics of NV magnetic imaging in a confocal microscope configuration.** A bulk diamond is placed on top of the sample, with a layer of ensemble NV centers close to the contact side. The diamond-sample stack is scanned with respect to the focused laser spot, so that NVs at different locations are addressed during the scan. The NV-sample distance h in this configuration is the sum of the NV depth below diamond surface plus the stand-off distance between the diamond and the sample.

or the stack with a motorized positioner. NVs at different locations in plane will therefore be addressed during the scan, allowing magnetic field measurements across the sample surface. Another similar strategy of addressing NVs across the sample is *wide-field* microscopy [19, 24]: the excitation laser is instead defocused to address NVs in a larger area (and therefore requires more power), and a CCD camera is used to simultaneously measure the NV PL from the entire field of view.

The diamond-on-chip configuration is feasible for many applications due to its experimental simplicity: No extra complication in e.g. diamond nanofabrication or fine placement of the NVs is needed, and the use of ensemble NVs provides a strong PL signal and therefore enables the detection of weaker signals (eq. (2.13)).

The main limitation of this configuration lies in its spatial resolution. In the diamond-sample stack, the NV-sample distance h (fig. 2.4) is the depth of the NV layer plus the possible finite stand-off distance due to dust particles in between the diamond and the sample. Since the spatial resolution of magnetic imaging is directly determined by the probe-sample distance [25, 26], it is therefore limited to the micrometer-scale. To minimize the stand-off distance, it is possible to use micrometer-sized diamond membranes instead of millimeter-sized bulk diamond [27, 28], so that the possibility of having dust particles underneath can be eliminated. In this case, the spatial resolution is in turn limited by the laser spot size i.e. the diffraction limit of the excitation laser.

2.3.2. Scanning-probe magnetometry using diamond cantilevers

However, since NV center is an *atomic* sensor, the diffraction limit of the laser is of course not a fundamental limit for NV magnetometers. Therefore, to unlock the potential of nanoscale magnetic imaging, the scanning probe approach has been developed [29]. Instead of a bulk diamond, a nano-fabricated diamond cantilever with an extruding tip is used. A single NV center (or sometimes a small ensemble) resides at the apex of the tip, and is scanned over the sample surface, illustrated in fig. 2.5
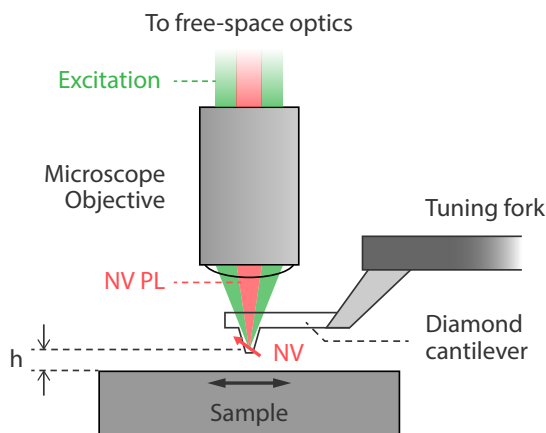
Figure 2.5 - **Schematics of scanning-probe NV magnetometry.** A single NV center resides in the tip apex of a nano-fabricated diamond cantilever. The tip-sample distance h is controlled through a tuning-fork atomic force microscope (AFM) system. The relative position between the objective and the cantilever stays fixed, while the sample is scanned with a (nano-)positioner to realize scanning.

The scanning probe geometry provides a solution to both limiting factors of spatial resolution - diffraction limit and stand-off distance - simultaneously. The former is circumvented by addressing only a single NV center, while the tip-on-cantilever geometry allows the NV probe to be integrated into an atomic force microscope (AFM) system. By gluing the diamond cantilever to the prong of a tuning fork [30], the tip-sample distance can be precisely controlled via the tuning-fork AFM mechanics with nanometer precision. At the cost of experimental complication, the spatial resolution of NV magnetometry can be pushed down to tens of nanometers, leading to numerous experimental breakthroughs especially in condensed matter physics [23, 31–33].

2.4. NV magnetometry using fiber-coupled diamond nanobeams

For both experimental configurations discussed in section 2.3, the NV centers are addressed through free-space optics. For certain applications, however, the requirement of free-space optical access is not trivial to meet. Such conditions include e.g. cryogenic, intra-cellular and other hard-to-reach environments. Yet applying NV magnetometry under these conditions can enable new measurements and provide valuable insight in e.g. low-temperature (quantum) science, biochemistry [19] or paleomagnetism [34], through its unique, versatile capabilities such as vector magnetometry [35, 36] and relaxometry measurements [37–40].

As such, all-fiber based NV probes have been developed. The majority of previously reported all-fiber NV probes usually consist of NV-hosting single-crystal diamonds fixed to the cleaved end of optical fibers [41–43]. Excitation and readout of the NV centers in the diamond is then achieved directly through the core of the fiber. While such probes have demonstrated capabilities of high-sensitivity magnetic field sensing, the size of the sensor diamond (ranging from micrometers to millimeters) limits the spatial resolution, precluding their application in studying magnetic phenomena on shorter length scales. Also, the collection efficiency in such configurations is limited by the mismatch of numerical aperture, and suffers from loss at the diamond-fiber interface.

In order to achieve high spatial resolution and high sensitivity in scanning-probe imaging, the sensor needs to be in close proximity to the target sample, with limited size and optimized readout efficiency. To address these requirements for fiber-based NV probes, in this thesis we aim to develop a new scanning-NV sensor based on a tapered diamond nanobeam that is optically coupled to, and manipulated with, a tapered optical fiber. The nanobeam structure allows us to confine the NV sensor spins to a nanoscopic volume, enabling scanning-probe magnetometry down to nanoscale spatial resolution. Furthermore, such fiber-coupled nanobeam probes can also benefit from the potentially near-perfect optical coupling efficiency [44] through adiabatic coupling, thereby realizing high-sensitivity magnetic imaging.

This section serves as an overview of the fiber-coupled diamond nanobeam scanning probe: we give a brief theoretical explanation to understand the mode coupling at the tapered interface in section 2.4.1, and discuss the envisioned experimental scheme in section 2.4.2.

2.4.1. Optical mode coupling at the fiber-nanobeam interface

The configuration of a fiber-coupled diamond nanobeam probe is illustrated in fig. 2.6(a). Through the contact between the fiber taper and the nanobeam taper, light is *wave-guided* from the fiber to the diamond (and vice versa). Such a configuration has been implemented in e.g. optomechanics and quantum network applications, to realize a fiber-coupled optical interface for nanophotonic waveguide devices with near-perfect coupling efficiency [44–47]. Below we provide a qualitative explanation of the condition required for efficient light coupling.
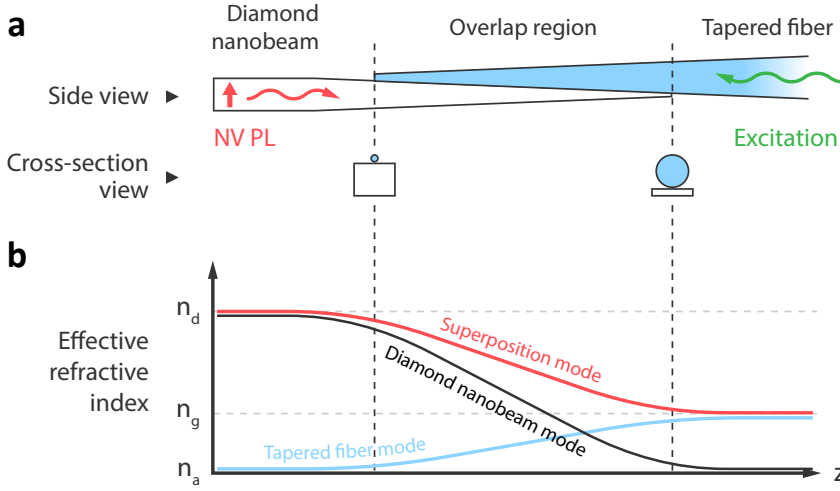
Figure 2.6 - **Schematics of the fiber-nanobeam coupling interface.** **(a)** Side view and cross-section view of the tapering and overlap of the nanobeam and the fiber. **(b)** Qualitative behavior of effective refractive index across the coupling region. When the adiabatic condition (eq. (2.17)) is met, the effective index of the superposition mode exhibits a gradual transition from the diamond nanobeam mode to the tapered fiber mode (or vice versa). n_d, n_g and n_a denote the refractive indices of diamond, glass and air respectively.

The behavior of light in such a configuration is usually elaborated in the language of waveguide optics. In absence of any tapering, i.e. when the waveguide is translationally invariant along the longitudinal direction z, the electric field profile of a wave-guided mode propagating along z can be written in the variable separated form of

$$\mathbf{E}(x, y, z) = \mathbf{e}(x, y)e^{i\beta z}. \tag{2.14}$$

Here, $\mathbf{e}(x, y)$ is the z-invariant cross-sectional field profile, and the propagation of the mode is characterized by the *propagation constant* β, or equivalently, the *effective refractive index*

$$n_{\text{eff}} = \beta / k_0 \tag{2.15}$$

where k_0 is the wave vector in vacuum.

The translational invariance in z is no longer present under the composite waveguide structure in fig. 2.6(a). This introduces z dependence in both the propagation constant β, and consequently the cross-sectional field profile e. In order for the light mode to efficiently evolve from the guided mode of the fiber to that of the nanobeam (or vice versa), it requires the variation of the cross-sectional profile to be *gradual*. The term "gradual" here can be specified as satisfying the "local mode" approximation [48]: at any longitudinal position z_0, the field profile $\mathbf{E}(x, y, z_0)$

can be approximated by that of a translationally invariant waveguide with the same cross section at z_0

$$\mathbf{E}(x, y, z_0) \approx \mathbf{e}(x, y, \beta(z_0)) e^{i\beta(z_0)z}, \qquad (2.16)$$

with $\beta(z_0)$ being the propagation constant of the composite waveguide at z_0, which also implicitly determines the cross-sectional profile at z_0.

The condition at which the local mode approximation holds is referred to as the *adiabatic condition*. One of its approximated forms can be expressed as [46, 48]

$$z_t \gg z_b = \frac{2\pi}{\beta - \beta^*}. \qquad (2.17)$$

where z_t is the length over which the cross section of the composite waveguide changes, and z_b is defined as the *beat length* between the propagating mode of interest and the closest different eigenmode, characterized by propagation constants β and β^* respectively. Essentially, z_b characterizes the length at which the *field profile* exhibits a significant variation due to the presence of the second mode, when the waveguide is approximated as translationally invariant. For the approximation to be valid, a significant variation in the *waveguide profile* can only happen at a larger length scale, hence requiring $z_t \gg z_b$. This is discussed in more detail in sections 19 and 28 of ref. [48].

When the adiabatic condition is met, the propagating light mode can be efficiently guided across the coupling interface. This is best pictured by the effective refractive index of the superposition mode along z, gradually evolving from the refractive index of diamond to that of glass (fig. 2.6(b)). Quantitative, numerical simulations of this process can be found in refs. [44–46]. Ideally, the coupling efficiency can reach 100%, while in reality it can be limited by factors such as fabrication imperfection and finite misalignment.

Aside from the coupling efficiency of the guided mode, extra complication is involved for our envisioned scheme in fig. 2.6(a), where we try to extract the emission of an NV center near the end-facet of the nanobeam. The fraction of NV emission into the guided mode under such complicated boundaries also plays an important role in the total collection efficiency, and it requires further simulation to be accounted for accurately.

2.4.2. Fiber-coupled diamond nanobeam as a scanning probe

As a magnetic field sensor, the fiber-coupled diamond nanobeam has a natural scanning-probe geometry. Similar to the existing scanning cantilever approach, the scanning measurement is enabled by mounting and scanning the sample perpendicularly underneath the nanobeam end facet, as illustrated in fig. 2.7. By getting rid of the free-space optical components in the vicinity of the probe, the nanobeam scanner offers better compatibility with measurements in hard-to-reach environments.

The realization of the measurement scheme in fig. 2.7 can be split into addressing the following challenges:
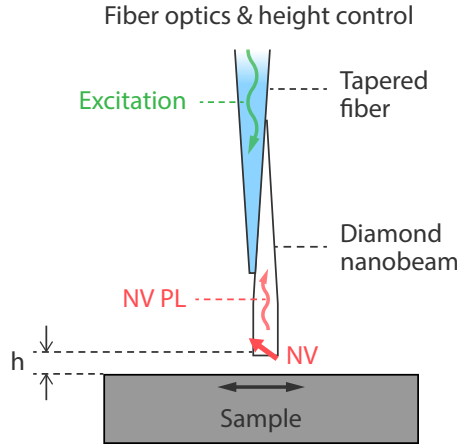
Figure 2.7 - **Schematics of scanning-probe measurements using NVs in a fiber-coupled diamond nanobeam.** An ensemble of NVs or a single NV is placed near the end facet of the nanobeam, and is addressed through the fiber interface. The sample is mounted perpendicular to the nanobeam, and is scannned with a (nano-)positioner to realize magnetic imaging.

- **Fabrication of the nanobeam probe:** A recipe needs to be developed to fabricate single-crystal diamond into tapered nanobeams. Furthermore, to realize proper 2D imaging, such a recipe should also incorporate the creation of NV centers *only* at the end facet of the nanobeams.

- **Coupling the nanobeam to the tapered fiber:** The fabricated NV-hosting diamond nanobeams need to be coupled to the tip of the tapered fiber in a deterministic and robust way, to ensure the optimization of readout efficiency (which is sensitive to the relative position between the nanobeam and the fiber) and keep the readout stable during scanning measurements.

- **Setting up scanning measurement:** One crucial aspect of realizing nanoscale 2D imaging is the precise control of the lift height h in fig. 2.7. Besides, an extra challenge of scanning in the absence of free-space optical access is the navigation over the sample surface, as locating a specific region of interest becomes non-trivial without direct visuals.

Throughout the rest of this thesis, our effort on tackling the above challenges will be discussed in detail.

References

[1] A. Gali, M. Fyta, and E. Kaxiras. "Ab initio supercell calculations on nitrogen-vacancy center in diamond: Electronic structure and hyperfine tensors". In: *Physical Review B* 77.15 (Apr. 2008), p. 155206. ISSN: 10980121. DOI: 10.1103/PhysRevB.77.155206.

[2] A. Lenef and S. C. Rand. "Electronic structure of the N-V center in diamond: Theory". In: *Physical Review B* 53.20 (May 1996), pp. 13441–13455. ISSN: 0163-1829. DOI: 10.1103/PhysRevB.53.13441.

[3] J. R. Maze, A. Gali, E. Togan, Y. Chu, A. Trifonov, E. Kaxiras, and M. D. Lukin. "Properties of nitrogen-vacancy centers in diamond: the group theoretic approach". In: *New Journal of Physics* 13.2 (Feb. 2011), p. 025025. ISSN: 1367-2630. DOI: 10.1088/1367-2630/13/2/025025.

[4] V. Ivády, T. Simon, J. R. Maze, I. A. Abrikosov, and A. Gali. "Pressure and temperature dependence of the zero-field splitting in the ground state of NV centers in diamond: A first-principles study". In: *Physical Review B* 90.23 (Dec. 2014), p. 235205. ISSN: 1098-0121. DOI: 10.1103/PhysRevB.90.235205.

[5] S. Felton, A. M. Edmonds, M. E. Newton, P. M. Martineau, D. Fisher, D. J. Twitchen, and J. M. Baker. "Hyperfine interaction in the ground state of the negatively charged nitrogen vacancy center in diamond". In: *Physical Review B* 79.7 (Feb. 2009), p. 075203. ISSN: 1098-0121. DOI: 10.1103/PhysRevB.79.075203.

[6] M. J. Rayson and P. R. Briddon. "First principles method for the calculation of zero-field splitting tensors in periodic systems". In: *Physical Review B* 77.3 (Jan. 2008), p. 035119. ISSN: 10980121. DOI: 10.1103/PhysRevB.77.035119.

[7] Z. Bodrog and A. Gali. "The spin-spin zero-field splitting tensor in the projector-augmented-wave method". In: *Journal of Physics Condensed Matter* 26.1 (Jan. 2014). ISSN: 09538984. DOI: 10.1088/0953-8984/26/1/015305.

[8] Á. Gali. "Ab initio theory of the nitrogen-vacancy center in diamond". In: *Nanophotonics* (2019). ISSN: 21928614. DOI: 10.1515/nanoph-2019-0154.

[9] N. Aslam, G. Waldherr, P. Neumann, F. Jelezko, and J. Wrachtrup. "Photo-induced ionization dynamics of the nitrogen vacancy defect in diamond investigated by single-shot charge state detection". In: *New Journal of Physics* 15 (Jan. 2013). ISSN: 13672630. DOI: 10.1088/1367-2630/15/1/013064.

[10] J. Happacher, J. Bocquel, H. T. Dinani, M. A. Tschudin, P. Reiser, D. A. Broadway, J. R. Maze, and P. Maletinsky. "Temperature-dependent photophysics of single NV centers in diamond". In: *Physical Review Letters* 131.8 (Aug. 2023), p. 086904. ISSN: 0031-9007. DOI: 10.1103/PhysRevLett.131.086904.

[11] N. B. Manson, J. P. Harrison, and M. J. Sellars. "Nitrogen-vacancy center in diamond: Model of the electronic structure and associated dynamics". In: *Physical Review B* 74.10 (2006), p. 104303. ISSN: 10980121. DOI: 10.1103/PhysRevB.74.104303.

[12] L. Robledo, H. Bernien, T. v. d. Sar, and R. Hanson. "Spin dynamics in the optical cycle of single nitrogen-vacancy centres in diamond". In: *New Journal of Physics* 13.2 (Feb. 2011), p. 025013. ISSN: 1367-2630. DOI: 10.1088/1367-2630/13/2/025013.

[13] J. P. Tetienne, L. Rondin, P. Spinicelli, M. Chipaux, T. Debuisschert, J. F. Roch, and V. Jacques. "Magnetic-field-dependent photodynamics of single NV defects in diamond: An application to qualitative all-optical magnetic imaging". In: *New Journal of Physics* 14 (Oct. 2012). ISSN: 13672630. DOI: 10.1088/1367-2630/14/10/103033.

[14] J. F. Barry, J. M. Schloss, E. Bauch, M. J. Turner, C. A. Hart, L. M. Pham, and R. L. Walsworth. "Sensitivity optimization for NV-diamond magnetometry". In: *Reviews of Modern Physics* 92.1 (Mar. 2020). ISSN: 15390756. DOI: 10.1103/RevModPhys.92.015004.

[15] A. Dréau, M. Lesik, L. Rondin, P. Spinicelli, O. Arcizet, J. F. Roch, and V. Jacques. "Avoiding power broadening in optically detected magnetic resonance of single NV defects for enhanced dc magnetic field sensitivity". In: *Physical Review B* 84.19 (Nov. 2011), p. 195204. ISSN: 1550235X. DOI: 10.1103/PhysRevB.84.195204.

[16] C. L. Degen, F. Reinhard, and P. Cappellaro. "Quantum sensing". In: *Reviews of Modern Physics* 89.3 (July 2017). ISSN: 15390756. DOI: 10.1103/RevModPhys.89.035002.

[17] J. R. Maze, P. L. Stanwix, J. S. Hodges, S. Hong, J. M. Taylor, P. Cappellaro, L. Jiang, M. V. G. Dutt, E. Togan, A. S. Zibrov, A. Yacoby, R. L. Walsworth, and M. D. Lukin. "Nanoscale magnetic sensing with an individual electronic spin in diamond". In: *Nature* 455.7213 (Oct. 2008), pp. 644–647. ISSN: 0028-0836. DOI: 10.1038/nature07279.

[18] G. Balasubramanian, I. Y. Chan, R. Kolesov, M. Al-Hmoud, J. Tisler, C. Shin, C. Kim, A. Wojcik, P. R. Hemmer, A. Krueger, T. Hanke, A. Leitenstorfer, R. Bratschitsch, F. Jelezko, and J. Wrachtrup. "Nanoscale imaging magnetometry with diamond spins under ambient conditions". In: *Nature* 455.7213 (Oct. 2008), pp. 648–651. ISSN: 0028-0836. DOI: 10.1038/nature07278.

[19] D. Le Sage, K. Arai, D. R. Glenn, S. J. Devience, L. M. Pham, L. Rahn-Lee, M. D. Lukin, A. Yacoby, A. Komeili, and R. L. Walsworth. "Optical magnetic imaging of living cells". In: *Nature* 496.7446 (Apr. 2013), pp. 486–489. ISSN: 00280836. DOI: 10.1038/nature12072.

2

[20] H. C. Davis, P. Ramesh, A. Bhatnagar, A. Lee-Gosselin, J. F. Barry, D. R. Glenn, R. L. Walsworth, and M. G. Shapiro. "Mapping the microscale origins of magnetic resonance image contrast with subcellular diamond magnetometry". In: *Nature Communications* 9.1 (Dec. 2018). ISSN: 20411723. DOI: 10.1038/s41467-017-02471-7.

[21] D. R. Glenn, R. R. Fu, P. Kehayias, D. Le Sage, E. A. Lima, B. P. Weiss, and R. L. Walsworth. "Micrometer-scale magnetic imaging of geological samples using a quantum diamond microscope". In: *Geochemistry, Geophysics, Geosystems* 18.8 (Aug. 2017), pp. 3254–3267. ISSN: 15252027. DOI: 10.1002/2017GC006946.

[22] L. Thiel, Z. Wang, M. A. Tschudin, D. Rohner, I. Gutiérrez-Lezama, N. Ubrig, M. Gibertini, E. Giannini, A. F. Morpurgo, and P. Maletinsky. "Probing magnetism in 2D materials at the nanoscale with single-spin microscopy". In: *Science* 364.6444 (June 2019), pp. 973–976. ISSN: 0036-8075. DOI: 10.1126/science.aav6926.

[23] I. Gross, W. Akhtar, V. Garcia, L. J. Martínez, S. Chouaieb, K. Garcia, C. Carrétéro, A. Barthélémy, P. Appel, P. Maletinsky, J. V. Kim, J. Y. Chauleau, N. Jaouen, M. Viret, M. Bibes, S. Fusil, and V. Jacques. "Real-space imaging of non-collinear antiferromagnetic order with a single-spin magnetometer". In: *Nature* 549.7671 (Sept. 2017), pp. 252–256. ISSN: 14764687. DOI: 10.1038/nature23656.

[24] S. E. Lillie, D. A. Broadway, N. Dontschuk, S. C. Scholten, B. C. Johnson, S. Wolf, S. Rachel, L. C. Hollenberg, and J. P. Tetienne. "Laser modulation of superconductivity in a cryogenic wide-field nitrogen-vacancy microscope". In: *Nano Letters* 20.3 (Mar. 2020), pp. 1855–1861. ISSN: 15306992. DOI: 10.1021/acs.nanolett.9b05071.

[25] A. Rustagi, I. Bertelli, T. van der Sar, and P. Upadhyaya. "Sensing chiral magnetic noise via quantum impurity relaxometry". In: *Physical Review B* 102.22 (Dec. 2020), p. 220403. ISSN: 24699969. DOI: 10.1103/PhysRevB.102.220403.

[26] B. G. Simon, S. Kurdi, J. J. Carmiggelt, M. Borst, A. J. Katan, and T. van der Sar. "Filtering and imaging of frequency-degenerate spin waves using nanopositioning of a single-spin sensor". In: *Nano Letters* 22.22 (Nov. 2022), pp. 9198–9204. ISSN: 1530-6984. DOI: 10.1021/acs.nanolett.2c02791.

[27] M. Borst, P. H. Vree, A. Lowther, A. Teepe, S. Kurdi, I. Bertelli, B. G. Simon, Y. M. Blanter, and T. van der Sar. "Observation and control of hybrid spin-wave–Meissner-current transport modes". In: *Science* 382.6669 (Oct. 2023), pp. 430–434. ISSN: 0036-8075. DOI: 10.1126/science.adj7576.

[28] S. Asif, H. Chen, J. Cremer, S. Ravan, J. Tamara-Isaza, S. Lamsal, R. Ebadi, Y. Li, L.-J. Zhou, C.-Z. Chang, J. Q. Xiao, A. Yacoby, R. L. Walsworth, and M. J. H. Ku. "Diamond micro-chip for quantum microscopy". In: *arXiv:2403.10414* (Mar. 2024). URL: https://arxiv.org/abs/2403.10414.

[29] P. Maletinsky, S. Hong, M. S. Grinolds, B. Hausmann, M. D. Lukin, R. L. Walsworth, M. Loncar, and A. Yacoby. "A robust scanning diamond sensor for nanoscale imaging with single nitrogen-vacancy centres". In: *Nature Nanotechnology* 7.5 (2012), pp. 320–324. ISSN: 17483395. DOI: 10.1038/nnano.2012.50.

[30] B. Simon. "Building a platform for magnetic imaging of spin waves". PhD thesis. TU Delft, 2023.

[31] K. Chang, A. Eichler, J. Rhensius, L. Lorenzelli, and C. L. Degen. "Nanoscale imaging of current density with a single-spin magnetometer". In: *Nano Letters* 17.4 (Apr. 2017), pp. 2367–2373. ISSN: 15306992. DOI: 10.1021/acs.nanolett.6b05304.

[32] B. G. Simon, S. Kurdi, H. La, I. Bertelli, J. J. Carmiggelt, M. Ruf, N. De Jong, H. Van Den Berg, A. J. Katan, and T. Van Der Sar. "Directional excitation of a high-density magnon gas using coherently driven spin waves". In: *Nano Letters* 21.19 (Oct. 2021), pp. 8213–8219. ISSN: 15306992. DOI: 10.1021/acs.nanolett.1c02654.

[33] S. Chen, S. Park, U. Vool, N. Maksimovic, D. A. Broadway, M. Flaks, T. X. Zhou, P. Maletinsky, A. Stern, and B. I. H. A. Yacoby. "Current induced hidden states in Josephson junctions". In: *arXiv:2402.02472* (Feb. 2024). URL: https://arxiv.org/abs/2402.02472.

[34] L. V. de Groot, K. Fabian, A. Béguin, M. E. Kosters, D. Cortés-Ortuño, R. R. Fu, C. M. Jansen, R. J. Harrison, T. van Leeuwen, and A. Barnhoorn. "Micromagnetic tomography for paleomagnetism and rock-magnetism". In: *Journal of Geophysical Research: Solid Earth* 126.10 (Oct. 2021). ISSN: 21699356. DOI: 10.1029/2021JB022364.

[35] B. Chen, X. Hou, F. Ge, X. Zhang, Y. Ji, H. Li, P. Qian, Y. Wang, N. Xu, and J. Du. "Calibration-free vector magnetometry using nitrogen-vacancy center in diamond integrated with optical vortex beam". In: *Nano Letters* 20.11 (Nov. 2020), pp. 8267–8272. ISSN: 1530-6984. DOI: 10.1021/acs.nanolett.0c03377.

[36] G. Wang, Y.-X. Liu, Y. Zhu, and P. Cappellaro. "Nanoscale vector AC magnetometry with a single nitrogen-vacancy center in diamond". In: *Nano Letters* 21.12 (June 2021), pp. 5143–5150. ISSN: 1530-6984. DOI: 10.1021/acs.nanolett.1c01165.

[37] H. Wang, S. Zhang, N. J. Mclaughlin, B. Flebus, M. Huang, Y. Xiao, C. Liu, M. Wu, E. E. Fullerton, Y. Tserkovnyak, and C. R. Du. "Noninvasive measurements of spin transport properties of an antiferromagnetic insulator". In: *Science Advances* 8 (2022), eabg8562. DOI: https://doi.org/10.1126/sciadv.abg8562.

[38] N. J. Mclaughlin, C. Hu, M. Huang, S. Zhang, H. Lu, G. Q. Yan, H. Wang, Y. Tserkovnyak, N. Ni, and C. R. Du. "Quantum imaging of magnetic phase transitions and spin fluctuations in intrinsic magnetic topological nanoflakes". In: *Nano Letters* 22.14 (July 2022), pp. 5810–5817. ISSN: 15306992. DOI: 10.1021/acs.nanolett.2c01390.

[39] F. Machado, E. A. Demler, N. Y. Yao, and S. Chatterjee. "Quantum noise spectroscopy of dynamical critical phenomena". In: *Physical Review Letters* 131.7 (Aug. 2023), p. 070801. ISSN: 0031-9007. DOI: 10.1103/PhysRevLett.131.070801.

[40] R. Xue, N. Maksimovic, P. E. Dolgirev, L.-Q. Xia, R. Kitagawa, A. Müller, F. Machado, D. R. Klein, D. MacNeill, K. Watanabe, T. Taniguchi, P. Jarillo-Herrero, M. D. Lukin, E. Demler, and A. Yacoby. "Signatures of magnon hydrodynamics in an atomically-thin ferromagnet". In: *arXiv:2403.01057* (Mar. 2024). URL: https://arxiv.org/abs/2403.01057.

[41] I. V. Fedotov, L. V. Doronina-Amitonova, D. A. Sidorov-Biryukov, N. A. Safronov, S. Blakley, A. O. Levchenko, S. A. Zibrov, A. B. Fedotov, S. Y. Kilin, M. O. Scully, V. L. Velichansky, and A. M. Zheltikov. "Fiber-optic magnetic-field imaging". In: *Optics Letters* 39.24 (Dec. 2014), p. 6954. ISSN: 0146-9592. DOI: 10.1364/ol.39.006954.

[42] G. Chatzidrosos, J. S. Rebeirro, H. Zheng, M. Omar, A. Brenneis, F. M. Stürner, T. Fuchs, T. Buck, R. Rölver, T. Schneemann, P. Blümler, D. Budker, and A. Wickenbrock. "Fiberized diamond-based vector magnetometers". In: *Frontiers in Photonics* 2 (Aug. 2021). DOI: 10.3389/fphot.2021.732748.

[43] S. Dix, D. Lönard, I. C. Barbosa, J. Gutsche, J. Witzenrath, and A. Widera. "A miniaturized magnetic field sensor based on nitrogen-vacancy centers". In: *arXiv:2402.19372* (Feb. 2024). URL: https://arxiv.org/abs/2402.19372.

[44] M. J. Burek, C. Meuwly, R. E. Evans, M. K. Bhaskar, A. Sipahigil, S. Meesala, B. MacHielse, D. D. Sukachev, C. T. Nguyen, J. L. Pacheco, E. Bielejec, M. D. Lukin, and M. Lončar. "Fiber-coupled diamond quantum nanophotonic interface". In: *Physical Review Applied* 8.2 (Aug. 2017). ISSN: 23317019. DOI: 10.1103/PhysRevApplied.8.024026.

[45] S. Gröblacher, J. T. Hill, A. H. Safavi-Naeini, J. Chan, and O. Painter. "Highly efficient coupling from an optical fiber to a nanoscale silicon optomechanical cavity". In: *Applied Physics Letters* 103.18 (Oct. 2013). ISSN: 00036951. DOI: 10.1063/1.4826924.

[46] T. G. Tiecke, K. P. Nayak, J. D. Thompson, T. Peyronel, N. P. de Leon, V. Vuletić, and M. D. Lukin. "Efficient fiber-optical interface for nanophotonic devices". In: *Optica* 2.2 (Feb. 2015), p. 70. ISSN: 23342536. DOI: 10.1364/optica.2.000070.

[47] L. Magrini, R. A. Norte, R. Riedinger, I. Marinković, D. Grass, U. Delić, S. Gröblacher, S. Hong, and M. Aspelmeyer. "Near-field coupling of a levitated nanoparticle to a photonic crystal cavity". In: *Optica* 5.12 (Dec. 2018), p. 1597. ISSN: 23342536. DOI: 10.1364/optica.5.001597.

[48] A. W. Snyder and J. D. Love. *Optical Waveguide Theory*. Chapman and Hall, 1983. ISBN: 0 412 09950 0.

3

Fabrication of diamond nanobeams

What we thought was for all time was momentary.

loml · Taylor Swift

Abstract

As the first step towards fiber-based scanning NV magnetometry, we discuss in this chapter the fabrication of NV-hosting diamond nanobeams. The discussion is divided into two major parts: the nano-fabrication process to create the nanobeam structure (section 3.1), and the placement of NV centers in these nanobeams (section 3.2). We discuss in detail our workflow based on reactive ion etching of diamond, and the novel strategy of angled ion implantation. Their combination allows us to fabricate diamond nanobeams out of a single-crystal bulk diamond, and deterministically create NV centers only at the end facets of the nanobeams in the same workflow.

Introduction

As concluded in section 2.4, combining fiber-optics with scanning-NV magnetometry can be a promising approach towards high resolution and sensitivity measurements in hard-to-reach environments. From this chapter on, we dive into the experimental details towards realizing fiber-based scanning-NV magnetometry using diamond nanobeam probes. Naturally, the creation of NV-hosting diamond nanobeam probes forms the foundation of this project.

In this chapter, we divide the process of diamond nanobeam fabrication into two parts: patterning the diamond into nanobeams based on reactive ion etching (section 3.1), and creating NV centers within the nanobeams based on ion implantation (section 3.2). The detailed procedure for both parts will be explained.

3.1. Workflow of diamond nanobeam fabrication

3.1.1. Overview of the quasi-isotropic diamond etch method

Our fabrication workflow is based on the quasi-isotropic diamond etch method. First demonstrated in ref.[1], it is nowadays one of the established approaches to fabricate free-standing nanostructures out of single-crystal bulk diamond [2–6]. Before going into the details, in this section we first provide a general overview to justify the choice and highlight the key points of this method.

The general strategy of fabricating such free-standing diamond structures can be divided into two major parts: *patterning* in which the geometry of the structure is defined, and *undercutting* in which the structure is released from the substrate. In our workflow, both are achieved via O_2-based reactive ion etching (RIE), one of the most common approaches for scalable nanofabrication of single-crystal diamond [7]. Specifically, the patterning of nanobeams is realized via an *anisotropic* RIE step, where we etch vertically into the diamond substrate that is covered by a patterned hard mask. And the undercutting of nanobeams is achieved by an *isotropic* RIE step.

The key challenge of the entire workflow lies in the undercutting part: similar undercut for fabricating Si or SiN waveguides [8] is usually achieved by selectively removing the sacrificial material underneath the layer of the target material. However, having a uniform, sub-micrometer thick single-crystal diamond layer on top of a different material is already a significant research challenge by itself [1].

Therefore, various methods of undercutting nanostructures from a *bulk* single crystal diamond have been developed. One option is angled O_2 RIE, where a Faraday cage is used to control the etching direction, resulting in a triangular cross-section of nanobeams [10, 11]. The quasi-isotropic etch that we use is another option, where we undercut the devices by (quasi-)isotropically etching the entire bulk diamond, with the patterned devices protected on the top surface and sidewalls with extra layers of mask. This will result in a rectangular cross section for the nanobeams, potentially better suited for both the fiber-coupling procedure that will be discussed in chapter 4 and possible future integration with nanophotonic structures.

---

[1]Nevertheless, it is not impossible: There are also research efforts to fabricate diamond nanophotonic devices by first creating high-quality diamond thin membranes [9].

The step-by-step overview of the nanobeam fabrication flow (*excluding* ion implantation, which will be discussed separately in section 3.2) is listed in table 3.1. The key parameters and implementation details of each step will be discussed in the following sections.

Step	Key Details
Surface polishing	Almax Easylab, $R_a < 2\,\text{nm}$
Surface cleaning	Fuming HNO_3, 10-15 min
Surface strain-relief etch	ICP-RIE with Ar/Cl_2 (10 sccm/20 sccm) then O_2 (50 sccm), removes $\sim 5\,\mu\text{m}$ from the surface
Hard mask deposition	$\sim 200\,\text{nm}$ Si_3N_4 with PECVD/ICPECVD
Spin-coating of resist	AR-P-6200.13 (CSAR-13) at 4000 rpm ($\sim 400\,\text{nm}$) followed by Electra-92 at 4000 rpm ($\sim 30\,\text{nm}$)
E-beam lithography	Beam dose $320\,\mu\text{C/cm}^2$, spot size $\sim 21\,\text{nm}$ and current $\sim 500\,\text{pA}$
Resist development	90 s in Pentylacetate, 60 s in 1:1 mixed MIBK & IPA, 60 s in IPA
Si_3N_4 etch	ICP-RIE with CHF_3/O_2 (60 sccm/6 sccm) at 20 °C
Resist removal	10 min DMF followed by 10 min piranha cleaning (96% H_2SO_4 and 31% H_2O_2, 3:1 mixed at 80 °C)
Anisotropic diamond etch	ICP-RIE with O_2 (50 sccm and 90 W RF), etches $\sim 600\,\text{nm}$ into the diamond
Sidewall protection	$\sim 20\,\text{nm}$ of Al_2O_3 deposition with ALD
Top-surface Al_2O_3 removal	ICP-RIE with BCl_3/Cl_2 (45 sccm/5 sccm) at 20 °C
Optional 2nd anisotropic diamond etch	ICP-RIE with O_2 (50 sccm and 90 W RF), etches $\sim 200\,\text{nm}$ into the diamond
Quasi-isotropic undercut	ICP-RIE with O_2 (50 sccm and 0 W RF) at 65 °C
Mask removal	10 min in 40% HF

Table 3.1 - **Workflow of diamond nanobeam fabrication**, with some of the key parameter details of each step.

3.1.2. Choice of the diamond substrate

We use the single-crystal, CVD-grown diamonds from Element-six for nanobeam fabrication. Throughout this thesis, two types of diamonds are used: the DNV-B14 diamond with a high NV concentration (4.5 ppm [12]) for nanobeams containing uniform ensemble NVs, and the EL SC plates with low nitrogen concentration (< 5 ppb) for nanobeams with post-implanted NVs. As received, the ensemble NV diamonds are $3\,mm \times 3\,mm \times 0.5\,mm$ pieces and the low nitrogen concentration diamonds are $4\,mm \times 4\,mm \times 0.5\,mm$, and both top surfaces are oriented to the {100} crystal plane. For both diamonds, the parameters for fabrication are identical (apart from the size of the substrate). Therefore in this section, we will use our fabrication process of the low nitrogen concentration diamond as an example. Unless mentioned otherwise, all the pictures are taken with the same low nitrogen concentration diamond.

3.1.3. Polishing and cleaning of diamond surface

Since our workflow follows a top-down approach from the surface of the diamond substrate, all the imperfections on the surface such as roughness, defects and contamination will eventually be translated into imperfections in fabricated devices. Therefore, in this chapter we discuss the pre-fabrication surface treatments of the diamond substrate, in order to make sure that the surface is smooth and contamination-free.

After receiving the diamond substrate, we slice the substrate into 8 membranes of $2\,mm \times 2\,mm \times 0.05\,mm$ and polish them on both sides mechanically (Almax EasyLab). For each batch of fabrication, only one of such membranes is used. Both surfaces of the membrane are polished down to a roughness of $R_a < 2\,nm$, and an additional cut on the corner is created so that it's possible to tell the two sides apart upon optical microscope inspection.

The membrane is then cleaned with fuming HNO_3 for 10-15 min to remove the contaminant from the slicing and polishing process. After the acid treatment, the diamond is rinsed with deionized (DI) water followed by an extra rinsing step in isopropanol (IPA), in order to minimize the dry stains that could form on the surface while blow-drying.

Since the mechanical polishing induces damage on the diamond surface, an inductively-coupled plasma reative ion etching (ICP-RIE) process using Ar/Cl_2 plasma is performed to remove about $1\sim 2\,\mu m$ from the polished diamond surface (Oxford Instruments Plasmalab 100), followed by an O_2 ICP-RIE to remove another $5\sim 6\,\mu m$ of diamond surface that could contain chlorine contamination [13]. The parameters used for this process is listed in table 3.2 [14]. During the etch, the diamond membrane is glued to a quartz carrier wafer (using a small droplet of e-beam resist PMMA495A4 as the glue) to remain stable, and the quartz wafer has a layer of titanium evaporated on the back side to avoid charge accumulation during the etch.

The Ar/Cl_2-O_2 etch is crucial if NV centers are to be implanted near the surface, as the properties of NV centers can be largely subject to nearby lattice defects. In this case the implantation should be carried out *after* the surface relieving etch. The

Etch step	Gas flow	RF power	ICP power	Temperature	Etch time
1. Ar/Cl$_2$ etch	10/20 sccm	200 W	500 W	30 °C	30 min
2. O$_2$ etch	50 sccm	90 W	1100 W	20 °C	20 min

Table 3.2 - **Parameters for the surface relieving etch,** using an Ar/Cl$_2$ etch followed by an O$_2$ etch.

nanobeams with uniform ensemble NVs, however, are fabricated without this step and yet still yield good readout of NV signal, primarily due to the very high NV concentration and a major contribution from NVs further away from the surface.

3.1.4. Creating the nanobeam patterns in a hard mask

As the first step in the fabrication, in this section we discuss the creation of the nanobeam pattern, through electron-beam (e-beam) lithography over a hard mask layer deposited on top of the diamond surface.

The necessity of an extra "hard" mask layer, instead of directly patterning a layer of e-beam resist on the diamond surface, is discussed in detail in ref. [4], along with the reason for choosing Si$_3$N$_4$ as the hard mask material among other candidates. The most important reason is that during the oxygen-based diamond etching later in the workflow, Si$_3$N$_4$ has a much higher selectivity (about 38 according to ref. [4], i.e. the etch rate of Si$_3$N$_4$ in O$_2$ ICP-RIE is 38 times slower than that of diamond) compared to e-beam resists. This allows the mask layer to be much thinner, beneficial for the fabrication of finer structures. A mask that is resilient against the oxygen plasma etch will also minimize mask erosion during the etch, as well as subsequent pattern distortion and rounding effects.

To create the hard mask layer, we deposit ∼ 200 nm of Si$_3$N$_4$ with chemical vapour deposition (CVD). The first generation of recipe uses plasma-enhanced chemical vapour deposition (PECVD, Oxford Instruments Plasmalab 80 Plus) to deposit Si$_3$N$_4$ at 300 °C. Later on, we switched to the inductively-coupled plasma enhanced chemical vapour deposition (ICPECVD, Oxford Instruments PlasmaPro 100) as it becomes available in Kavli Nanolab Delft. Apart from increased thickness uniformity across the sample, the new device also allows us to deposit at a much lower temperature (85 °C), thereby allowing the diamond membrane to be glued to a silicon carrier chip during the deposition. This greatly relieves the practical difficulty and risk involved in directly manipulating the 50 µm-thin membranes with tweezers over the 300 °C hot plate, as in the previous case. The relevant parameters for both processes are listed in table 3.3.

In practice, another dummy silicon chip is usually deposited alongside the diamond substrate in the same run in order to determine the actual thickness of deposited Si$_3$N$_4$ layer with an ellipsometer (Woollam M-2000)[2]. In practice, this

[2]The thickness of the native oxide layer of this dummy chip should also be measured before deposition in order to obtain optimal accuracy.

Device	Gas flow	Temp.	Dep. rate
PECVD	20 sccm SiH_4/20 sccm NH_3/980 sccm N_2	300 °C	~ 12 nm/min
ICPECVD	26 sccm SiH_4/25 sccm N_2	85 °C	~ 44 nm/min

Table 3.3 - **Parameters for PECVD and ICPECVD deposition of Si_3N_4 hard mask.**

dummy chip can also be the carrier chip on which the diamond is glued. This will be important at the later step of determining the thickness of the ALD Al_2O_3 layer: for ellipsometry measurements, tracking the thicknesses layer by layer on a reference sample provides much more accuracy over directly measuring an entire stack of material on a small, transparent diamond substrate (if this is possible at all).

E-beam lithography is then used to pattern the hard mask. The nanobeam patterns are written on a ~ 400 nm layer of positive resist AR-P-6200.13 (also referred to as CSAR-13) spin coated on top of the hard mask. Due to the insulating nature of diamond, an additional layer of conductive coating Electra-92 is further spin coated after baking the resist, to prevent charging of the substrate during exposure. The parameters for spin coating are listed in table 3.4. In practice, it's recommended to spin-coat the resists *in the same day* after the hard mask deposition, as exposing the hard mask in air for a longer time can result in deteriorated adhesion of the resist, probably because of surface chemistry changes[3].

Chemical	Spin speed & time	Expected thickness	Baking temp. & time
CSAR-13	4000 rpm, 1 min	~ 400 nm	150 °C, 3 min
Electra-92	4000 rpm, 1 min	~ 40 nm	90 °C, 2 min

Table 3.4 - **Parameters for spin coating the e-beam resists.**

The lithography pattern for each nanobeam consists of the nanobeam itself, the surrounding "cutout" area and a thin connection between the nanobeam and the rest of the bulk diamond where the breaking of the beam will happen. The specific geometrical dimensions and requirements of the fabricated nanobeams are discussed in the corresponding sections of chapter 4, and one example of the pattern design is shown in fig. 3.1 (a).

The parameters for e-beam exposure (Raith EBPG5200) are listed in table 3.5. Here a weak current is used to ensure the writing quality of the fine structures such as the connection area. Also because of the small feature sizes in this area, it is important that the writing order (shown in fig. 3.1(b)) is consecutive within each pattern. This is because beam distortion due to charging can still be present despite applying the extra conductive layer, causing stitching artifacts if the writing order is switching

---

[3]One possible remedy in case this happens is a brief oxygen descum (100 W RF and 200 sccm O_2 for 2 min, PVA Tepla 300) of the sample.
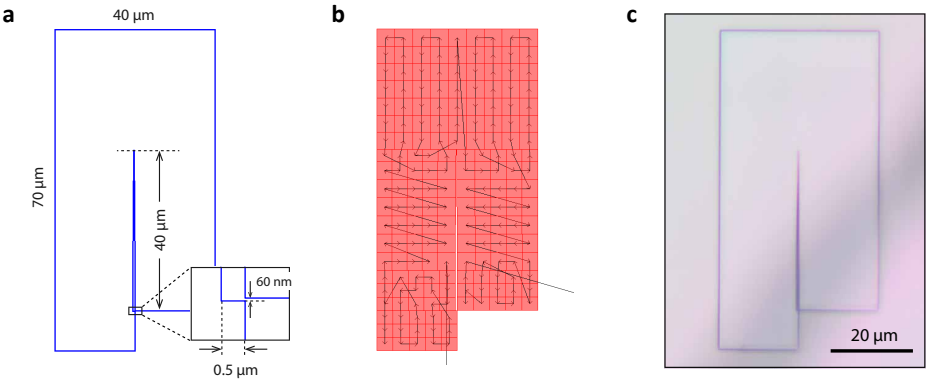
Figure 3.1 - **An exemplar nanobeam pattern for e-beam lithography.** **(a)** Original design in CAD. Bottom right inset shows the zoom-in view of the connection part. **(b)** Fracturing scheme (red blocks) and writing order (black arrows) determined in BEAMER, the e-beam pattern generation software. The writing order needs to follow the geometry of the pattern to avoid stitching artifacts. **(c)** Optical microscope image of one nanobeam pattern after e-beam exposure and development.

Beam spot size	Current	Dose	Aperture diameter
21 nm	538 pA	320 μC/cm^2	400 μm

Table 3.5 - **Parameters for e-beam exposure with Raith EBPG5200.**

back and forth between distant features.

After the exposure, we develop the resist in pentylacetate for 90 s, followed by 60 s in 1:1 mixture of MIBK (methyl isobutyl ketone) and IPA (isopropanol) and another 60 s rinsing in IPA. The optical microscope image of the pattern after development is shown in fig. 3.1(c).

We use an ICP-RIE with CHF_3/O_2 plasma (AMS 100 I-speeder) to transfer the pattern into the hard mask. The parameter details are listed in table 3.6. In practice, we mount the diamond carrier chip on a silicon carrier wafer using thermal paste, both as an adhesive and to ensure good thermal contact between the sample and the carrier. We run the etch for 3 minutes to *overetch* the hard mask, in order to make sure that the written area is completely etched away.

To further ensure the mask-free area is free of residual e-beam resist, we first use dimethylformamide (DMF) to dissolve the remaining e-beam resist (10 min). Normally this is not sufficient to remove all the resist, and residuals of resist will remain on the sample surface in the form of flakes or particles (one such example is marked in fig. 3.2(b)). We therefore further clean the sample in boiling piranha solution (96% H_2SO_4 and 31% H_2O_2, 3:1 mixed at 80 °C) for 10 minutes, which will

Process	Gas flow	RF power	ICP power	Temp.	Etch rate
CHF$_3$/O$_2$ etch	60/6 sccm	50 W	500 W	20 $^\circ$C	~ 110 nm/min

Table 3.6 - **Parameters for etching the Si$_3$N$_4$ hard mask.**
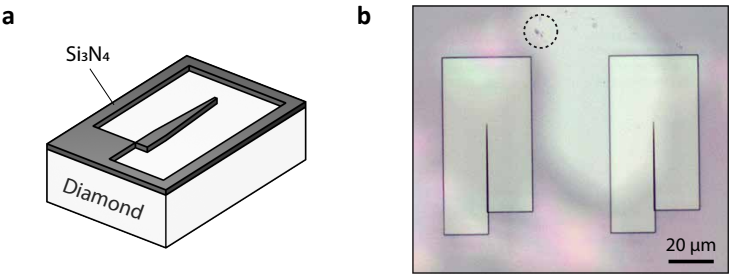
Figure 3.2 - **CHF$_3$/O$_2$ etch of the Si$_3$N$_4$ hard mask. (a)** Schematics of hard mask patterning. **(b)** Optical microscope image after hard mask etching and cleaning with DMF. A difference in color is visible between the hard mask covered area (light purple shade) and the exposed diamond surface. The black dashed circle encloses a piece of residual resist after DMF cleaning.

remove most of the residual resist from the sample surface. An alternative (and simpler) solution is to sonicate the sample in DMF for another 5-10 minutes at low power. For our nanobeam patterns this method usually also works well in terms of cleaning the resist, while more risk is indeed involved if the pattern contains more fine structures that could suffer from distortion during the sonication process.

3.1.5. Transferring the nanobeam pattern into the diamond

With the patterned hard mask on top of the diamond substrate, in this section we discuss the transfer of the nanobeam pattern into the diamond using reactive ion etching.

The pattern in the hard mask is transferred to the diamond substrate via another ICP-RIE step with O$_2$ plasma (Oxford Instruments Plasmalab 100). Here the term "anisotropic" refers to the directionality of the etch, i.e. the diamond will be etched vertically as a result of the voltage bias between the plasma source and the carrier substrate (controlled by the RF power applied in the recipe)[4]. This sets the difference between this step and the later step of (quasi-)*isotropic* etch which is also based on O$_2$ ICP-RIE. The recipe parameters are listed in table 3.7. For this step and all the following etch steps, we use a silicon carrier wafer with a thick (2 ~ 3 µm) layer

---

[4]Therefore the previously mentioned surface relief etch and hard mask etch are also anisotropic.

of thermal oxide termination, to make sure there's no etching and redeposition of silicon from the carrier wafer during the process.

Process	Gas flow	RF power	ICP power	Temp.	Etch rate
Aniso. O$_2$ etch	50 sccm	90 W	1100 W	20 °C	~ 300 nm/min

Table 3.7 - **Parameters for the anisotropic diamond etch.**
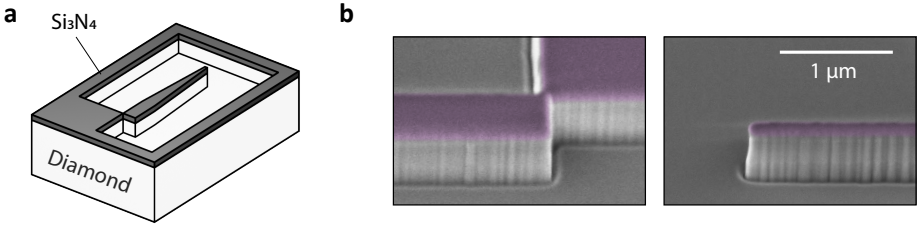
Figure 3.3 - **Anisotropic diamond etch.** **(a)** Schematics of the anisotropic diamond etch. **(b)** SEM images of the nanobeam pattern after the anisotropic etch (under 45° tilting angle). Left panel shows the connection area and right panel shows the tail of the nanobeam. The Si$_3$N$_4$ hard mask is false colored in purple.

The sample is inspected using a scanning electron microscope (SEM, Hitachi S-4800) after the etch. Figure 3.3(b) shows the resulting vertical sidewalls of the nanobeams. In this specific sample, we etch around 600 nm into the diamond, slightly more than the target final beam thickness (500 nm in this case) to allow for the upward etch during the undercut. On top of the vertical sidewalls, the roughness is also visible in the form of vertical stripes: these originate from the roughness of the e-beam resist on the pattern edges after development. Possible ways to mitigate this effect will be discussed in the outlook section. Besides, sections of slightly different slopes on the sidewalls are visible in the right panel, likely due to the change in the hard mask sidewall profile during the etch.

As a side note: Once the etch performance has been characterized, it is best to avoid SEM inspection at this stage of fabrication, as the hydrocarbon deposition induced by the electron beam [15] can be an extra source of unwanted micro-masking in the subsequent etch steps.

3.1.6. Protecting nanobeam sidewalls prior to undercutting

As briefly explained in section 3.1, the strategy to undercut the structure created in previous steps is to etch in all directions with the nanobeam itself protected. Since the sidewalls of the nanobeams are still exposed after the pattern transfer, extra protection of the sidewalls is needed to make sure the nanobeams themselves don't

get etched away during the undercut. In practice, the protection of nanobeams is accomplished in two steps.

- **Atomic layer deposition (ALD) of Al$_2$O$_3$:** In the first step, we create a uniform protection layer over the entire diamond substrate. We do so by using atomic layer deposition (ALD) to deposit a ~20 nm layer of Al$_2$O$_3$ (280 cycles at 105 °C, Oxford Instruments FlexAL). The reference chip (section 3.1.4) is also deposited in the same run, and is then used to precisely determine the thickness of deposited Al$_2$O$_3$ with ellipsometry. This is necessary for determining the correct etch time of the subsequent Al$_2$O$_3$ etch. Since the deposition rate (as in nm per cycle) of our specific ALD machine is subject to change over time, characterizing the layer thickness is necessary for us in each fabrication run.

- **Re-open the top surface with anisotropic Al$_2$O$_3$ etch:** Since the ALD process covers the sample uniformly, we need to re-open the top-side diamond surface to be able to etch it, while leaving the sidewalls of the nanobeams protected. This is achieved with another *anisotropic* ICP-RIE with BCl$_3$/Cl$_2$ plasma (Oxford Instruments Plasmalab 100). The parameters are listed in table 3.8.

Process	Gas flow	RF power	ICP power	Temp.	Etch rate
BCl$_3$/Cl$_2$ etch	45/5 sccm	10 W	600 W	20 °C	~30 nm/min

Table 3.8 - **Parameters for etching Al$_2$O$_3$.**

As discussed before, the etch time is determined through the previous measurement of the Al$_2$O$_3$ thickness, and usually includes a small amount of overetch again to make sure the mask is completely opened on the top surface. For example, for the specific sample in fig. 3.3(b) we measured 21.7 nm of Al$_2$O$_3$, considering the estimated ~30 nm/min etch rate (which could also be subject to change over time), we ran the etch for 50 s to ensure overetching. In practice, we also do 5-10 min of chamber preconditioning before the actual etch (i.e. running the same recipe using the same carrier wafer but without the sample). This ensures the smooth ignition of plasma, as possible glitches or failures of plasma ignition at the start of the etch can also have a non-negligible effect on the etch given its short duration.

3.1.7. Undercutting the nanobeams using quasi-isotropic RIE

After the previous step, the top side and sidewalls of the nanobeams are both protected (by Si$_3$N$_4$ and Al$_2$O$_3$ respectively), while the diamond surfaces in the cutout area around the nanobeams are exposed. We are then ready to perform the quasi-isotropic etch to undercut the nanobeams (Oxford Plasmalab 100), using the parameters listed in table 3.9.

The key difference compared to the previous O$_2$ etch is that RF power is set to 0, so no external voltage bias is applied to the oxygen plasma. This way, the directional

physical etching via ion bombardment on the substrate is suppressed, and the effect of *chemical* etching becomes more significant. In this regime, the diamond is etched in all directions though not fully isotropic, as the chemical etch rate is different for different crystallographic orientations. This has been systematically studied in ref. [16], and under our etching conditions the undercut is dominated by the downward etch along the {100} plane and the etch going "sideways" along the {111} orientations.

Process	Gas flow	RF power	ICP power	Temperature
Quasi-iso. O_2 etch	50 sccm	0 W	2500 W	65 °C

Table 3.9 - **Parameters for the quasi-isotropic diamond etch.**
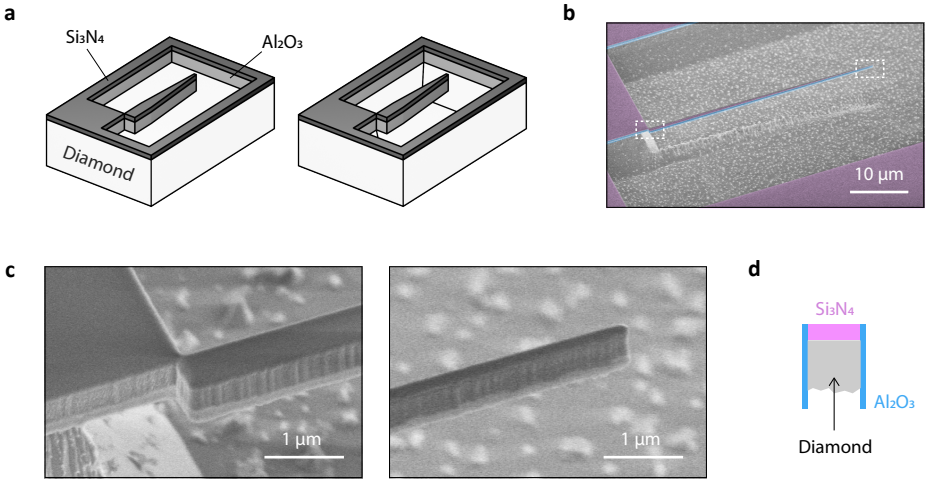
Figure 3.4 - **Quasi-isotropic diamond etch. (a)** Schematics of before (left) and after (right) quasi-isotropic etching **(b)** SEM image of a nanobeam after a 7-hour quasi-isotropic etch (inspected under 45° tilting angle). The Si_3N_4 hard mask and Al_2O_3 sidewall protection are false colored in purple and blue respectively. **(c)** Zoom-in SEM images of the connection (left) and tail (right) of the nanobeam, as marked in white dashed rectangles in (b). **(d)** Cross-section schematic of the nanobeam after the undercut.

Figure 3.4(b), (c) shows the SEM images after a 7-hour undercut. We discuss the following aspects of this process:

- **Second anisotropic etch:** For the sample in fig. 3.4, we did a second anisotropic etch before the quasi-isotropic etch. This etches about 250 nm further into the diamond and therefore creates a new section of "sidewall"

below the Al_2O_3 covered area. In practice, we found this step is optional as the nanobeams will still be undercut without this step, but it could possibly decrease the time needed for the nanobeams to be completely released: for samples without the second anisotropic etch, it can take 12~14 hours to fully undercut nanobeams of the same dimensions. There is, however, no quantitative characterization yet of how the etch rate depends on the second anisotropic etch, as the etch time is also largely affected by the sample and chamber condition and therefore varies across different fabrication runs.

- **Upward etching:** After the nanobeams are released, they will keep being etched upwards from their exposed bottom side [1]. This is visible in fig. 3.4(c): under SEM inspection, the thin alumina layer on the sidewalls are electron-transparent, allowing us to see through the mask and identify the remaining diamond as the darker gray part of the sidewall. The schematic of the beam cross section at this stage is illustrated in fig. 3.4(d), indicating the diamond is further etched upwards from the bottom of the alumina mask.

- **SEM inspection of etch status:** In practice, since the etch rate can vary for each fabrication run, we usually split the entire undercut process into 2 or 3 sessions and briefly inspect with SEM in between. This is to estimate the time still needed to complete the undercut, or fine-tune the beam thickness after undercutting and avoid over-etching. For example, the 7-hour undercut for the sample in fig. 3.4 is actually split into 4+3 hours. As mentioned before, here it is also important to limit the hydrocarbon deposition in the SEM, by only zooming in on a few devices and limiting the time of exposure.

- **Etching temperature:** We perform the quasi-isotropic etch at 65 °C because this is the maximum available temperature in our Oxford Plasmalab 100 system. This is also the reason for the long etch time in our process. By increasing the temperature to > 200°C[1, 2], the chemical etch rate can be increased, resulting in both decreased etch time and increased "isotropy". As of 2023, a new ICP-RIE system (Oxford PlasmaPro 100 Cobra) becomes available in Kavli Nanolab Delft, and is capable of reaching up to 250 °C. Initial tests on the new device see a significant decrease in undercut time down to around 2 hours with improved etching isotropy. Further tests and migration of diamond etching recipes are to be expected in the future.

After the quasi-isotropic etch, we clean the sample for 10 mins in 40% HF (hydrofluoric acid) to remove the Si_3N_4 and Al_2O_3 masks, and again inspect the end result with SEM, as shown in fig. 3.5.

During the acid cleaning, some nanobeams will already break from the connection point and can eventually land on the flat surface area of the diamond substrate. These beams make it possible to also inspect the bottom side of the nanobeams. As is visible in fig. 3.5 (d-f), the bottom side created from the undercut is much rougher compared to the polished top surface. This could be a limiting factor on the optical coupling efficiency, and minimizing the bottom roughness requires further effort on optimizing the undercut recipe.
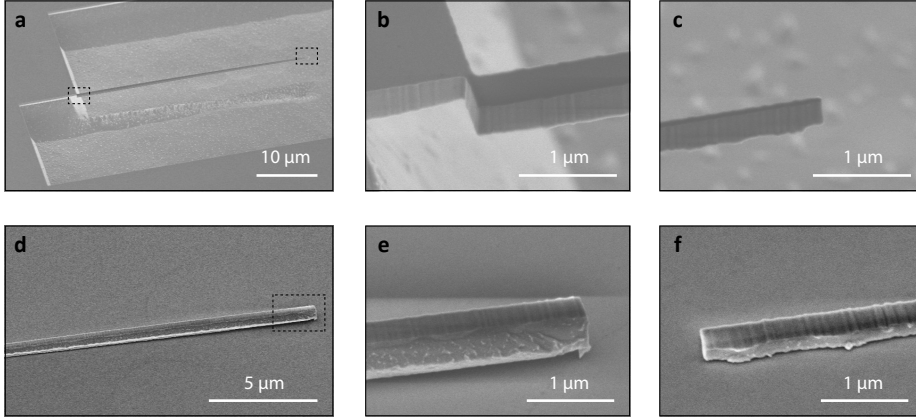
Figure 3.5 - **SEM images of nanobeams after mask removal with HF, under** $45°$
tilting angle. (a-c) A free-hanging nanobeam attached to the bulk of
diamond, with (b) and (c) the zoom-in views of the connection and tail
area respectively (dashed rectangle in (a)). **(d-f)** A detached nanobeam
lying on the diamond surface, with the sidewall facing up and bottom
side facing sideways. (e) and (f) are zoom-in views of both ends of the
nanobeam.

3.2. Creation and deterministic placement of NV centers

The creation of NV centers inside the diamond nanobeams is another crucial aspect
towards using the nanobeams as magnetometers. One of the most widely-used
approach of NV creation is ion implantation: nitrogen ions are implanted into the
surface of the diamond, and combine with the lattice vacancies in the subsequent
annealing process [17] to form NV centers. However, ion implantation is a
wafer-scale technique per se, while in order to realize a 2D scanning probe with the
nanobeams, the NV centers need to be located at the end of the nanobeams *only*.

Therefore, the deterministic placement of NV centers with respect to nanostructures
becomes a necessity. One possible approach of achieving this is to locate the
pre-implanted NVs with a marker system [18]: Before fabricating the nanostructures,
a marker system can be patterned on the diamond surface in order to precisely
determine the location of individual NV centers through their photoluminescence.
The nanostructures are then fabricated around the desired coordinates. Another
strategy is to implant nitrogen ions locally, enabled by a dedicated implantation
mask [19–21].

For our specific nanobeam geometry, however, we develop a novel strategy
that does not involve extra fabrication complexity in either alignment markers
or dedicated implantation mask. Utilizing the fact that the "end facets" of the
nanobeams are actually part of the sidewalls during the fabrication, we implant the
nitrogen ions directly into the sidewalls *halfway* in the fabrication process when

the top surface is still protected by the existing Si_3N_4 hard mask. This way, the implanted NVs will be self-aligned with the nanobeams and reside only at the desired end facets. The details of this process will be discussed in following sections.

3.2.1. Angled ion implantation

In this section we discuss the process details of the angled ion implantation, and its integration in the nanobeam fabrication workflow explained in the previous section. The angled ion implantation process follows after the first anisotropic diamond etch (section 3.1.5): We implant ^{14}N ion (INNOViON Corp.) with 50 keV energy and 1×10^{13} cm^{-2} fluence, oriented towards the end facet of the nanobeam with a large 80º tilt with respect to the surface normal, as shown in fig. 3.6(a). This way, the nanobeams will only be implanted on their end facets which are facing the implantation, while the top surface will be shielded by the Si_3N_4 hard mask. The implanted nitrogen atoms are expected to be centered at around 60 nm from the end facet according to SRIM simulations [22], larger than commonly found NV-surface distance in diamond scanning probes in order to minimize the potential effect of the nanobeam sidewall roughness. This will be discussed in more details in section 7.2.3.
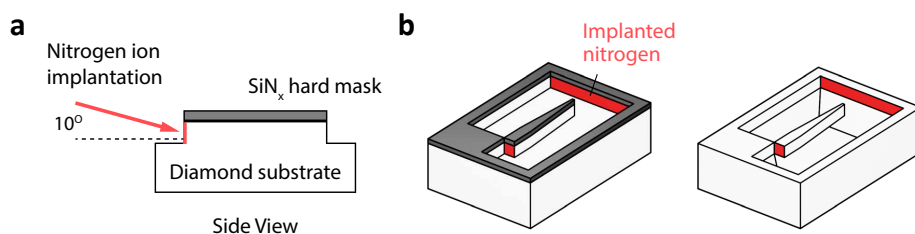
Figure 3.6 - **Angled ion implantation.** **(a)** Side view of the implantation scheme. Nitrogen ions are implanted at 10° shearing angle with respect to the sample surface, and aligned with the nanobeam orientation. **(b)** 3D view of the diamond after the implantation (left) and at the end of the fabrication flow (right). The implanted sidewalls are marked in red.

After receiving the implanted diamond, we do another boiling piranha cleaning to clean the surface, then proceed with ALD and continue the fabrication process. As also mentioned in section 3.1.7, a second anisotropic diamond etch is performed after re-opening the diamond top surface. This is because the unmasked top surface of the diamond is also exposed to ion implantation (at a 10° shearing angle), and the implantation induced surface damage or graphitization could possibly affect the subsequent undercut process. Removing the surface layer ensures that the undercut can start from a clean crystalline diamond surface.

3.2.2. Post-implantation processes: Annealing and tri-acid cleaning

After the implantation, the implanted nitrogen can only combine with the lattice vacancies created during the implantation and form NV centers through a subsequent high-temperature annealing process [17, 23]. During the annealing, the lattice vacancies become mobile at high temperature, and can therefore combine with nearby nitrogen to form NV centers. The details of our annealing procedure will be discussed in this section.

Temperature (°C)	RT $\rightarrow$ 60	60 $\rightarrow$ 400	400	400 $\rightarrow$ 800	800	800 $\rightarrow$ RT
Time (h)	12	6	4	6	2	~4

Table 3.10 - **Temperature protocol for diamond annealing.**

The full temperature protocol we use for annealing was developed in ref. [14] and is listed in table 3.10. The annealing oven (Nabertherm) is pumped down to $\sim 4 \times 10^{-6}$ mbar during the annealing process. Very importantly, for the angled ion implantation workflow, we perform the annealing only *after* the final mask removal step instead of directly after implantation, to ensure a clean diamond surface and avoid any possible side-effect from the mask materials at high temperature.

The non-ideal vacuum condition during the annealing results in a graphitized layer on the diamond surface, which could be an extra source of surface noise on the NV centers [24], and therefore needs to be removed with tri-acid cleaning [25]. We note that, however, in the fabrication of our angle-implanted nanobeams we *did not* tri-acid clean the chip: This is mainly due to the significant practical difficulty of handling the thin diamond substrate throughout the cleaning process without losing the free-hanging nanobeams by e.g. accidentally scratching on the surface with tweezers. We do still get decent NV signal readout as will be discussed in chapter 5, probably due to their relatively high density. A way of properly handling the diamond substrate with nanostructures will be needed (e.g. a dedicated holder to keep it fixed during acid clean) in order to completely clean the remaining non-diamond carbon layer on the sidewalls facing implantation.

Nevertheless, since tri-acid cleaning is still a standard procedure for our diamond fabrication in general, we discuss its details in the following paragraphs. In this process, a boiling mixture of 60% perchloric acid ($HClO_4$), 65% nitric acid (HNO_3)[5] and 96% sulphuric acid (H_2SO_4) is used to selectively remove the graphitized layer. Due to the explosive perchlorate salt that could form from condensing perchloric vapour, dedicated glassware and setup is needed in order to perform the tri-acid cleaning safely in a standard wet bench.

The setup is illustrated in fig. 3.7[6]. The air-tight configuration makes sure the acid vapour stays inside the system. We load the diamond substrate(s) in a dedicated teflon holder and dip the holder into the acid mixture inside the reaction flask. After

---

[5]Instead of fuming nitric acid commonly used for general acid cleaning.
[6]This setup is designed and constructed by E. Straver of Kavli Nanolab Delft.
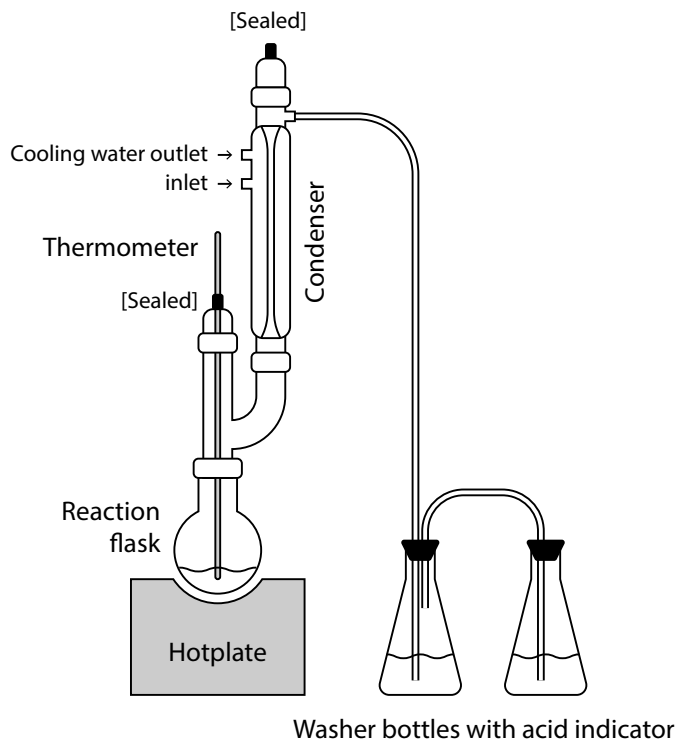
Figure 3.7 - **Setup for triacid cleaning.** 1:1:1 mixture of the three acids are heated up in the reaction flask, and the evaporated acid vapours are cooled down in the condenser and will flow back into the reaction flask. The entire glassware set is sealed so no acid vapour can escape into the wet bench, minimizing the risk of perchlorate salt formation. A thermometer is directly dipped into the liquid to monitor its temperature.

assembling the setup, the acid is then slowly heated up until boiling, marked by the bubbling of the liquid and the temperature no longer increasing. We keep the liquid boiling for ~1h, and then turn off the hot plate to allow cooling back down to room temperature.

The maximum temperature we can reach in this process is around $120 \sim 130\,^{\circ}$C, which is essentially the boiling temperature of 65% nitric acid. This limit is set by the configuration of our setup: the evaporated acid is cooled down in the condenser and flows back into the reaction flask, eventually keeping the temperature from increasing further to >200 $^{\circ}$C as reported in e.g. ref.[25] where the acid vapour is recondensed in a different flask. This could potentially reduce the effectiveness of the cleaning. One possible way of reaching higher temperature without a re-design of the entire setup is to heat up only perchloric and sulphuric acid (as they are the effective components for removing graphitized diamond), and do nitric acid cleaning

to remove organic contaminants as a separate step beforehand. The first test run sees an increasing of boiling temperature to around 190 °C, and the effectiveness remains to be systematically characterized.

3.2.3. Photoluminescence characterization using a scanning confocal microscope
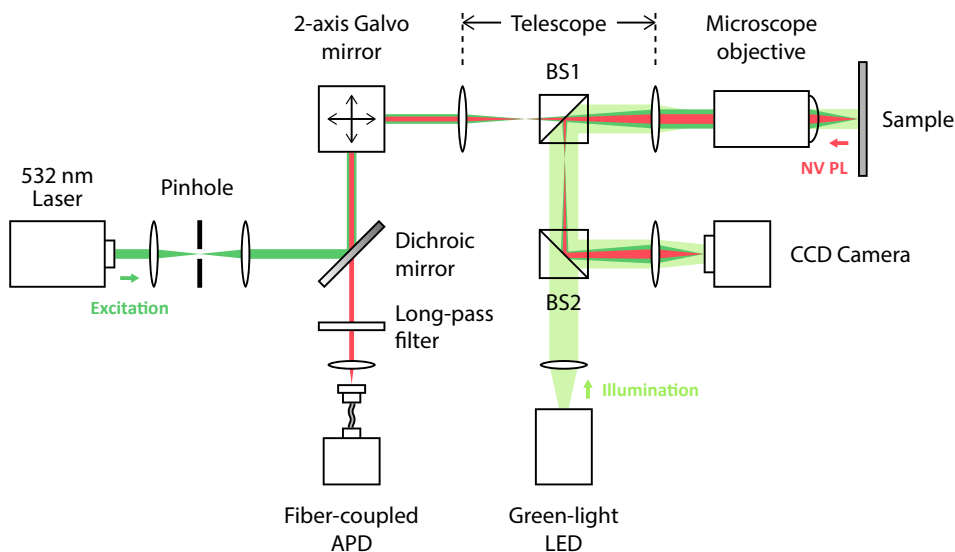
Figure 3.8 - **Simplified schematics of the scanning confocal microscope.** A 532 nm excitation laser and a green light illumination LED is sent through the microscope objective (50×) and shines on the sample surface. The lenses in the path are arranged such that the excitation laser is focused on the sample surface while the LED light is collimated for homogeneous wide-field illumination. The telescope system adjusts the scanning range of the laser spot. The pinhole combined with two lenses filters out unwanted noise modes from the laser source.

Before proceeding with coupling the fabricated nanobeams to tapered fibers, we first check the distribution of implanted NV centers with a free-space scanning confocal microscope to confirm the existence of NVs at the tip of the fabricated nanobeams.

The simplified schematic of this setup is illustrated in fig. 3.8. The sample is mounted on a 3-axis micro-positioner (Mad City Labs). A CCD camera and a green light LED allow illumination and navigation over the sample surface before performing a scan (when the LED will be turned off to avoid extra background). A 2-axis galvo mirror (Thorlabs GVS212) is used to to steer the excitation laser beam so that the focused laser spot is scanned in 2D over the sample surface, and the

photoluminescence at the laser spot is collected by the avalanche photodiode (APD) after filtering out the reflected laser using a dichroic mirror and a 600 nm long-pass filter.
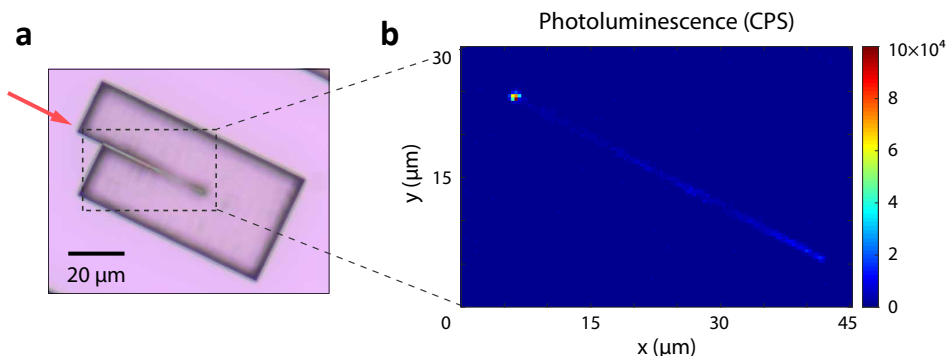
Figure 3.9 - **Photoluminescence intensity map of a nanobeam after annealing. (a)** Optical microscope image of one nanobeam device after the fabrication flow. The red arrow indicates the direction of implantation. **(b)** PL map of the black dashed area in (a). A laser power of 1.5 μW is used to perform the confocal scan. The bright spot indicates the existence of NV photoluminescence at the end of the beam.

This allows us to visualize the distribution of implanted NV centers through a photoluminescence map, as illustrated in fig. 3.9(b). The PL map shows a distinct bright spot at one end of the beam, indicating the presence of an NV ensemble as expected from the implantation direction. Furthermore, the nanobeam shape is outlined by an above-background photoluminescence level, and this is most likely a combined effect of light scattering on the nanostructure, and the presence of implantation along the sidewalls of the nanobeam due to the misalignment between the implantation direction and the nanobeam orientation. Further confirmation and analysis of the sidewall implantation will be discussed in section 5.3.2.

As a further confirmation of the implantation direction, fig. 3.10 shows the PL map of two test structures, measured under the same conditions. These structures are patterned on the same diamond substrate alongside the nanobeams, and receive the same implantation. For the circular cutout in fig. 3.10(a-c), we observe a gradient of PL intensity on one side of the circle, as expected for implantation at shearing angle. Figure 3.10(d-f) shows a series of linear trenches perpendicular to the implantation direction, with varying widths ranging from 1000 nm to 400 nm. As illustrated in fig. 3.10(f), the sidewall implantation will be shadowed and the size of implanted area decreases with decreasing trench width. This is confirmed by the decreasing PL intensity in fig. 3.10(a).
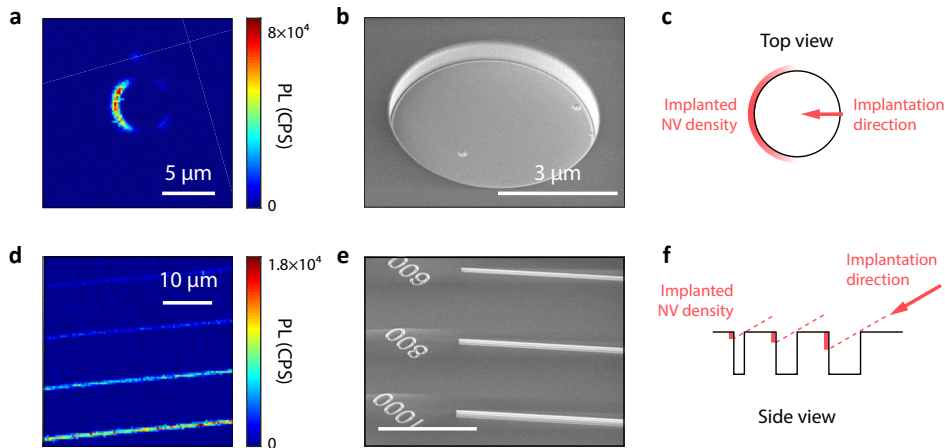
Figure 3.10 - **Photoluminescence intensity map of test tructures fabricated alongside the nanobeams. (a)** PL map of a circular cutout, indicating NV distribution only on one side of the circle. **(b)** SEM image of the circular cutout (with 45° tilt), taken after the first anisotropic etch. **(c)** Illustration of the implantation scheme. A gradient of NV density distribution along the sidewall facing implantation is expected. **(d-f)** PL map, SEM image and schematic illustration of linear trenches with varying width (indicated in nm by the numbers visible in (e)). Decreasing NV density, and therefore decreaing PL level, is expected and observed with decreasing trench width. The scale bar in (e) is 10 μm.

Acknowledgment

References

[1]   B. Khanaliloo, M. Mitchell, A. C. Hryciw, and P. E. Barclay. "High-Q/V monolithic diamond microdisks fabricated with quasi-isotropic etching". In: *Nano Letters* 15.8 (Aug. 2015), pp. 5131–5136. ISSN: 15306992. DOI: 10.1021/acs.nanolett.5b01346.

[2]   S. Mouradian, N. H. Wan, T. Schröder, and D. Englund. "Rectangular photonic crystal nanobeam cavities in bulk diamond". In: *Applied Physics Letters* 111.2 (July 2017). ISSN: 00036951. DOI: 10.1063/1.4992118.

[3]   N. H. Wan, T. J. Lu, K. C. Chen, M. P. Walsh, M. E. Trusheim, L. De Santis, E. A. Bersin, I. B. Harris, S. L. Mouradian, I. R. Christen, E. S. Bielejec, and D. Englund. "Large-scale integration of artificial atoms in hybrid photonic circuits". In: *Nature* 583.7815 (July 2020), pp. 226–231. ISSN: 14764687. DOI: 10.1038/s41586-020-2441-3.

[4]   M. Ruf. "Cavity-enhanced quantum network nodes in diamond". PhD thesis. TU Delft, 2021.

[5]   M. Pasini, N. Codreanu, T. Turan, A. Riera Moral, C. F. Primavera, L. De Santis, H. K. C. Beukers, J. M. Brevoord, C. Waas, J. Borregaard, and R. Hanson. "Nonlinear quantum photonics with a tin-vacancy center coupled to a one-dimensional diamond waveguide". In: *Physical Review Letters* 133.2 (July 2024), p. 023603. ISSN: 0031-9007. DOI: 10.1103/PhysRevLett.133.023603.

[6]   T. Pregnolato, M. E. Stucki, J. M. Bopp, M. H. v. d. Hoeven, A. Gokhale, O. Krüger, and T. Schröder. "Fabrication of Sawfish photonic crystal cavities in bulk diamond". In: *APL Photonics* 9.3 (Mar. 2024). ISSN: 2378-0967. DOI: 10.1063/5.0186509.

[7]   A. Toros, M. Kiss, T. Graziosi, S. Mi, R. Berrazouane, M. Naamoun, J. Vukajlovic Plestina, P. Gallo, and N. Quack. "Reactive ion etching of single crystal diamond by inductively coupled plasma: State of the art and catalog of recipes". In: *Diamond and Related Materials* 108 (Oct. 2020). ISSN: 09259635. DOI: 10.1016/j.diamond.2020.107839.

[8]   L. Magrini, R. A. Norte, R. Riedinger, I. Marinković, D. Grass, U. Delić, S. Gröblacher, S. Hong, and M. Aspelmeyer. "Near-field coupling of a levitated nanoparticle to a photonic crystal cavity". In: *Optica* 5.12 (Dec. 2018), p. 1597. ISSN: 23342536. DOI: 10.1364/optica.5.001597.

[9]   S. W. Ding, M. Haas, X. Guo, K. Kuruma, C. Jin, Z. Li, D. D. Awschalom, N. Delegan, F. J. Heremans, A. High, and M. Loncar. "High-Q cavity interface for color centers in thin film diamond". In: *arXiv:2402.05811* (Feb. 2024). URL: doi.org/10.48550/arXiv.2402.05811.

[10]   M. J. Burek, N. P. De Leon, B. J. Shields, B. J. Hausmann, Y. Chu, Q. Quan, A. S. Zibrov, H. Park, M. D. Lukin, and M. Lončar. "Free-standing mechanical and photonic nanostructures in single-crystal diamond". In: *Nano Letters* 12.12 (Dec. 2012), pp. 6084–6089. ISSN: 15306984. DOI: 10.1021/nl302541e.

[11]   M. J. Burek, Y. Chu, M. S. Liddy, P. Patel, J. Rochman, S. Meesala, W. Hong, Q. Quan, M. D. Lukin, and M. Loncar. "High quality-factor optical nanocavities in bulk single-crystal diamond". In: *Nature Communications* 5 (2014). ISSN: 20411723. DOI: 10.1038/ncomms6718.

[12]   Element Six. *DNV Series Datasheet*. 2021. URL: https://e6cvd.com/uk/material/single-crystalline/dnv-b14-%203-0mmx3-0mm-0-5mm.html.

[13]   P. Appel, E. Neu, M. Ganzhorn, A. Barfuss, M. Batzer, M. Gratz, A. Tschöpe, and P. Maletinsky. "Fabrication of all diamond scanning probes for nanoscale magnetometry". In: *Review of Scientific Instruments* 87.6 (June 2016), p. 063703. ISSN: 0034-6748. DOI: 10.1063/1.4952953.

[14]   B. Simon. "Building a platform for magnetic imaging of spin waves". PhD thesis. TU Delft, 2023.

[15]   R. Egerton, P. Li, and M. Malac. "Radiation damage in the TEM and SEM". In: *Micron* 35.6 (Aug. 2004), pp. 399–409. ISSN: 09684328. DOI: 10.1016/j.micron.2004.02.003.

[16]   L. Xie, T. X. Zhou, R. J. Stöhr, and A. Yacoby. "Crystallographic orientation dependent reactive ion etching in single crystal diamond". In: *Advanced Materials* 30.11 (Mar. 2018). ISSN: 0935-6648. DOI: 10.1002/adma.201705501.

[17]   S. Pezzagna, D. Rogalla, D. Wildanger, J. Meijer, and A. Zaitsev. "Creation and nature of optical centres in diamond for single-photon emission—overview and critical remarks". In: *New Journal of Physics* 13.3 (Mar. 2011), p. 035024. ISSN: 1367-2630. DOI: 10.1088/1367-2630/13/3/035024.

[18]   N. H. Wan, B. J. Shields, D. Kim, S. Mouradian, B. Lienhard, M. Walsh, H. Bakhru, T. Schröder, and D. Englund. "Efficient extraction of light from a nitrogen-vacancy center in a diamond parabolic reflector". In: *Nano Letters* 18.5 (May 2018), pp. 2787–2793. ISSN: 1530-6984. DOI: 10.1021/acs.nanolett.7b04684.

[19]   D. M. Toyli, C. D. Weis, G. D. Fuchs, T. Schenkel, and D. D. Awschalom. "Chip-scale nanofabrication of single spins and spin arrays in diamond". In: *Nano Letters* 10.8 (Aug. 2010), pp. 3168–3172. ISSN: 1530-6984. DOI: 10.1021/nl102066q.

[20]   P. Spinicelli, A. Dréau, L. Rondin, F. Silva, J. Achard, S. Xavier, S. Bansropun, T. Debuisschert, S. Pezzagna, J. Meijer, V. Jacques, and J.-F. Roch. "Engineered arrays of nitrogen-vacancy color centers in diamond based on implantation of CN- molecules through nanoapertures". In: *New Journal of Physics* 13.2 (Feb. 2011), p. 025014. ISSN: 1367-2630. DOI: 10.1088/1367-2630/13/2/025014.

[21]   M. Schukraft, J. Zheng, T. Schröder, S. L. Mouradian, M. Walsh, M. E. Trusheim, H. Bakhru, and D. R. Englund. "Precision nanoimplantation of nitrogen vacancy centers into diamond photonic crystal cavities and waveguides". In: *APL Photonics* 1.2 (May 2016). ISSN: 23780967. DOI: 10.1063/1.4948746.

[22]   J. Ziegler. *SRIM-2013*. 2013. URL: http://www.srim.org/.

[23]   L. Allers, A. T. Collins, and J. Hiscock. "The annealing of interstitial-related optical centres in type II natural and CVD diamond". In: *Diamond and Related Materials* 7.2-5 (Feb. 1998), pp. 228–232. ISSN: 09259635. DOI: 10.1016/S0925-9635(97)00161-1.

[24]   S. Sangtawesin, B. L. Dwyer, S. Srinivasan, J. J. Allred, L. V. H. Rodgers, K. De Greve, A. Stacey, N. Dontschuk, K. M. O'Donnell, D. Hu, D. A. Evans, C. Jaye, D. A. Fischer, M. L. Markham, D. J. Twitchen, H. Park, M. D. Lukin, and N. P. de Leon. "Origins of diamond surface noise probed by correlating single-spin measurements with surface spectroscopy". In: *Physical Review X* 9.3 (Sept. 2019), p. 031052. ISSN: 2160-3308. DOI: 10.1103/PhysRevX.9.031052.

[25]   K. J. Brown, E. Chartier, E. M. Sweet, D. A. Hopper, and L. C. Bassett. "Cleaning diamond surfaces using boiling acid treatment in a standard laboratory chemical hood". In: *Journal of Chemical Health & Safety* 26.6 (Nov. 2019), pp. 40–44. ISSN: 1871-5532. DOI: 10.1016/j.jchas.2019.06.001.

3

4

Coupling diamond nanobeams to tapered optical fibers

Birds of a feather,
we should stick together

BIRDS OF A FEATHER · Billie Eilish

Abstract

After the fabrication flow, the diamond nanobeams remain attached to the diamond substrate through the thin connection point. In this chapter, we discuss the process of breaking the nanobeams off the substrate, and subsequently coupling them to tapered optical fibers. We first explain the fabrication of tapered fibers and the setup we use to manipulate the nanobeams in section 4.1 and section 4.2 respectively. We then discuss two strategies for coupling nanobeams to tapered fibers: breaking the nanobeams off the substrate using the fiber itself and coupling via van der Waals forces (section 4.3), and using optical glue for a more robust assembly (section 4.4). With the latter, we show that we can realize a robust and transportable assembly, ready to be used as an all-fiber scanning NV magnetometer.

Introduction

The optical coupling between the tapered fiber and the diamond nanobeam is crucial as it directly determines the readout efficiency and therefore the sensitivity of the probe [1]. In order to properly couple the fabricated diamond nanobeams to the tip of the tapered fibers, experimental methods need to be developed to address two major challenges:

- **Breaking the nanobeams from the bulk diamond substrate:** As discussed in the previous chapter, at the end of the fabrication flow, the nanobeams are free-hanging from the diamond substrate except for the connection point (will be referred to as the "tether" for the rest of the thesis). We designed the nanobeam patterns in such a way that the tether is thin (< 100 nm) to facilitate the breaking process, yet it is still non-trivial due to the difficulty of breaking diamond on the nanoscale as will be shown in section 4.3.

- **Optimizing the readout:** Specifically, readout optimization is achieved in practice by fine tuning the relative position between the tapered fiber and the diamond nanobeam while monitoring the readout counts. While the optimization is straightforward per se, another implicit challenge lies in *maintaining* the optimized readout after the beams are broken off the substrate and during actual scanning-probe operation.

Two experimental methods of fiber-nanobeam coupling will be discussed in this chapter. In section 4.3, we address the above two aspects in one single step, by directly using the tapered fiber itself to break the nanobeams and utilizing purely the van der Waals adhesion for the coupling. The simplicity of this method comes at the cost of reduced stability of the fiber-nanobeam coupling and less control over their relative position after breaking. Therefore in section 4.4 we describe the second method where the two challenges are addressed in separate steps. By applying adhesive to the assembly, the robustness and stability of readout efficiency can be greatly improved.

4.1. Preparation of the tapered fibers

Creating a gradual taper at the end of an optical fiber is crucial for the efficient adiabatic mode coupling (section 2.4.1). The tapered fibers used through the rest of the thesis are fabricated in-house by chemically etching the commercial single-mode optical fibers (S630-HP) using hydrofluoric acid [2, 3].

We choose the S630-HP fiber because its pure-silica core has significantly lower autofluorescence compared to the common germanium-doped silica core fibers. This can be elaborated in fig. 4.1, where the autofluorescence distribution at the fiber end-facet is imaged using a CCD camera (Thorlabs CS165MU). It is clearly visible that for the germanium-doped core SM600 fiber, the autofluorescence is distinctly concentrated at the core, and will therefore overlap spatially with the actual NV signal that is also confined in the core. While for the pure-silica core S630-HP fiber,

the autofluorescence is more homogeneously distributed across the end-facet and the intensity at the core is significantly lower. More quantitative analysis on how the fiber autofluorescence compares to the NV signal will be explained in chapter 5.
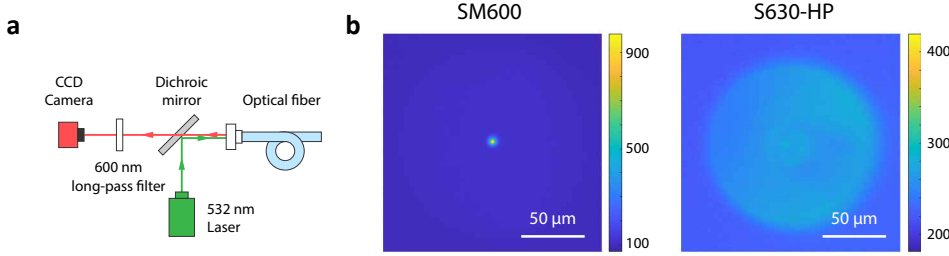
Figure 4.1 - **Autofluorescence characterization of two single-mode fibers. (a)** Optical setup for visualizing the autofluorescence distribution of single-mode fibers. 532 nm excitation laser is coupled into the fiber, and the end-facet of the fiber is imaged using a CCD camera, with a dichroic mirror and a 600 nm long-pass filter to remove the reflected excitation laser. **(b)** Autofluorescence distribution on the end facet of an SM600 fiber (left) and an S630-HP fiber (right). Both images are taken under 1 mW excitation power measured before the fiber input, and the exposure time of the S630-HP fiber measurement (150 ms) is double the time of the SM600 measurement (75 ms).

The experimental procedure of tapering the fibers is illustrated in fig. 4.2(a): We remove the plastic coating on one end of the fibers, and dip the exposed silica part into 40% HF. The fibers are fixed onto a motorized stage (Thorlabs MTS50-Z8), which allows us to pull out the fibers at a constant velocity (set to $\sim 0.4\,\mu\mathrm{m\,s^{-1}}$ in our setup). As a result of the linearly increasing etch time towards the end of the fiber, a linearly tapered profile is created with a sharp $\sim 3°$ taper angle (determined by the ratio between etch rate of silica in HF and the pulling speed). A microscope image of the tapered fiber is shown in fig. 4.2(b).

4.2. Experimental setup for fiber-nanobeam coupling

The need to accurately manipulate the nanobeams and align them with respect to the tapered fibers requires control over their relative position at nanoscale precision. To do so, we construct the setup illustrated in fig. 4.3.

The tapered end of the optical fiber is mounted on a 3-axis coarse positioning stage, and the other end is spliced to an FC-APC connector for the in-coupling of the excitation laser from free space. Fine tuning of the relative position between the fiber tip and the diamond substrate is achieved with a 3-axis slip-stick positioner (Mechonics MX-35) where the substrate is mounted. The positioner is further mounted on a manual rotational stage to enable adjustments of the relative angle between the fiber and the nanobeams. To monitor the manipulation process, a
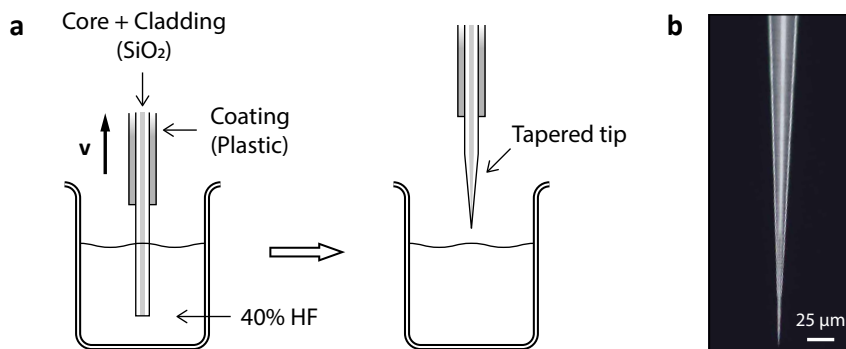
Figure 4.2 - **Fabrication of tapered optical fibers.** **(a)** Schematics of the tapering process using 40% hydrofluoric acid. After removing a section of plastic coating from the end of the fiber, we dip the stripped end into the HF and pull it out with a motorized stage. The pull-out process takes about 1h and the resulting tapered section is $1 \sim 2\,\text{mm}$ in length. In practice, a thin layer of xylene is added on top of the HF to prevent its evaporation. **(b)** Optical microscope image of a tapered optical fiber after the pull-out process.
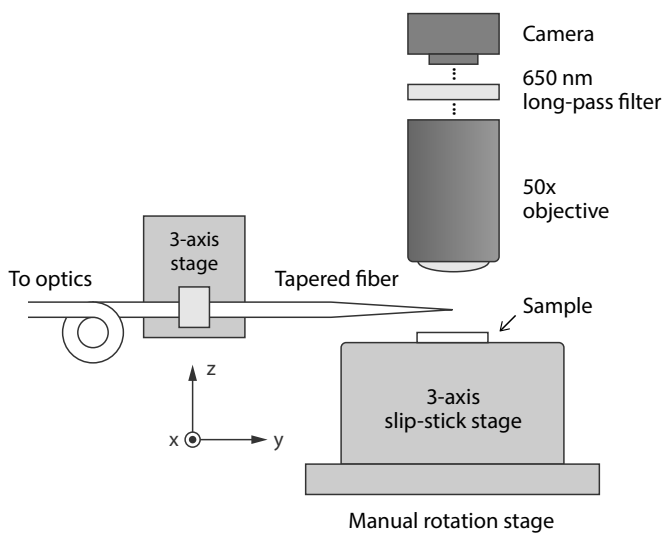
Figure 4.3 - **Schematics of the nanobeam manipulation setup.** The sample is mounted on a 3-axis slip-stick positioner, and the tapered fiber on a manual 3-axis coarse positioning stage. The manipulation process is monitored through the microscope system above the sample stage.

microscope system is assembled on top of the sample, consisting of a long working distance 50× objective (Mitutoyo M Plan Apo HR), a 650 nm long pass filter to filter out the excitation laser, and a CMOS camera (Thorlabs CS165MU).

In practice, we fix the position of the microscope, and start the manipulation process by placing the end of the fiber taper into focus using the coarse stage. We keep the x and y position of the fiber fixed during the rest of the process, and only use the motorized z axis of the fiber holder to bring the fiber tip in and out of focus during sample stage movement. We then temporarily lift the fiber tip, and use the slip-stick positioner to in turn bring the diamond substrate into focus. After navigating to the vicinity of a nanobeam, we bring the fiber tip back into focus, and proceed with the nanobeam manipulation procedure described in the following sections.

4

4.3. Direct breaking and coupling of nanobeams using the tapered fiber

In this section, we discuss our first successful strategy to break off individual tapered diamond nanobeams and attach them to tapered optical fibers, by directly pushing the fiber against the nanobeams and attaching them through presumably[1] van der Waals force [2, 4]. This method relies on the geometry of nanobeam design: By designing nanobeams with large aspect ratios and nanometer-scale tethers, we can overcome the large yield strength and the strong elastic deformation of diamond nanostructures caused by the applied force, which enables us to break off the beam while simultaneously attaching it to the fiber.

4.3.1. Breaking nanobeams off the substrate

To couple the nanobeams to a tapered optical fiber, we mount the nanobeam chip on the slip-stick positioner. Monitoring through the microscope objective, we push the fiber against the nanobeam by moving the stage perpendicularly to the beam until the connection point breaks and the nanobeam sticks to the fiber. The sticking is presumably due to van der Waals force. The process and end result are illustrated in fig. 4.4.

4.3.2. Requirements on geometrical parameters

Compared to similar strategies of picking up nanophotonic structures made from other materials, such as Si or SiN [2, 4, 5], the main challenge lies in the significantly larger yield strength of diamond compared to glass [6]. Also, single crystal diamond on the nanoscale is known to exhibit large elastic deformation before fracturing when pressure is applied [7], as we also observe while pushing on the beam with the fiber in fig. 4.4(b). The resulting abrupt motion when the beam breaks makes it challenging to stick the beam to the optical fiber.

---

[1]As there could also be a contribution from electrostatic forces.
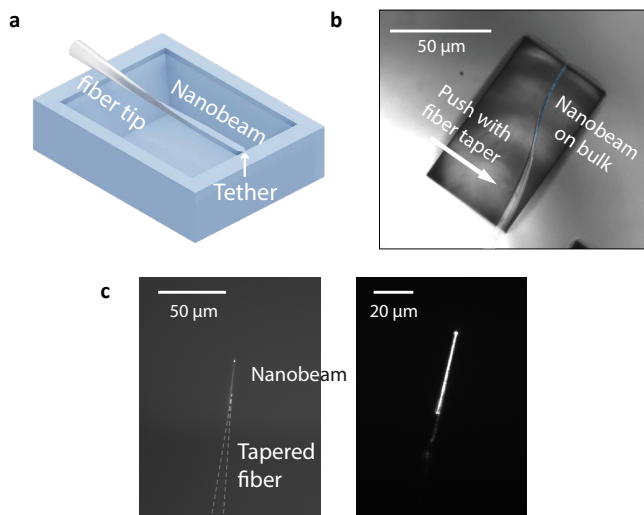
Figure 4.4 - **Assembly process of a fiber-coupled diamond nanobeam sensor. (a)** Schematic illustration of a tapered fiber brought into contact with a nanobeam, fabricated using DNV-B14 diamond containing uniformly distributed ensemble NVs. **(b)** Microscope image of the fiber pushing sideways on the nanobeam (artificially colored in blue) to break the ~ 70 nm-wide connection to the diamond chip. Both beam and fiber bend strongly before breaking. **(c)** After breaking off, the beam sticks to the fiber (outlined with the dashed line). Through-fiber green-laser excitation causes the bright NV photoluminescence along the entire nanobeam visible in this camera image. The image is taken with a 650 nm long-pass filter to block the excitation light. Right panel is a zoom-in view and with higher excitation power, highlighting the NV photoluminescence in the beam.

To overcome this challenge, we found it crucial to design beams that are at least 30 µm in length, which also ensures the adiabatic change of the effective refraction index according to ref.[8]. We also minimize the width of the tether by fabricating an array of devices with varying tether widths, and use the beams with the thinnest tethers that survived the fabrication process. Furthermore, the area of the open region around the beam should be large enough (in our design 70 µm × 40 µm) to allow for the beam displacement during the breaking process. With these parameters, we can fit more than 200 nanobeams devices on a 2 × 2 mm diamond substrate and complete the fabrication process in 4~5 days of net cleanroom processing time. After the fabrication, we are able to apply a large enough torque on the tether to break the nanobeam off the bulk with a tapered optical fiber, and couple the beam to the fiber in the same process. We find tether widths of 60-80 nm to be optimal, where around 60% of the beams remain attached to the bulk after the undercut and

subsequent acid cleaning. These nanobeams can then be picked up by the tapered fiber with a success rate of 50% (five out of ten beams).

4.3.3. Limitations in position control and transportation

One major limitation of this workflow lies in the control over the angle and position when attaching the nanobeam to the fiber. While we found that we can consistently break off the beams and attach them to a fiber, their relative position after the breaking process is not entirely under control due to the abrupt motion of the fiber-nanobeam when the tether breaks. We expect that reducing the tether width further, or reducing the nanobeam surface roughness via improved etching or ion-based polishing [9], could improve the coupling efficiency.

Additionally, transporting the fiber-nanobeam probes assembled through this method is challenging due to vibration and/or static electricity that cause the nanobeam to detach. We found that the nanobeams stay attached to the fiber as long as the devices are kept fixed in the setup. For instance, our nanobeams can remain attached to the fiber in the setup for more than two months. The outstanding challenge is the development of a method for dismounting the nanobeam-fiber assembly and transporting it to a different setup for either scanning measurements or further processes of enhancing adhesion.

4.4. Robust fiber-nanobeam assembly using optical glue

Given all the limitations discussed above, we need a more deterministic approach of attaching the nanobeam robustly to the fiber with optimized optical readout. This is crucial for realizing a sensor that is transportable to different setups and that does not break upon probe-sample contact during scanning-probe measurements.

We therefore developed a new workflow of nanobeam coupling based the method demonstrated in ref.[10]. Compared to the previous workflow, the major difference (also the key idea) lies in the following two aspects:

- **Splitting the "break" and the "stick":** Instead of relying on the proper alignment of nanobeams directly at the breaking of tethers, we now break the nanobeams off the bulk and place them on another carrier before sticking them to the tapered fibers. On the one hand, this allows the use of a separate, less flexible tip so that the breaking process is more under control. On the other hand, this also dissociates the readout optimization process from the abrupt motion at the breaking point and thereby allows the optimized coupling to be maintained after sticking.

- **Using an adhesive:** In the most straightforward way, using an extra adhesive solves the instability of the fiber-nanobeam coupling upon external interrogation. The challenge here lies in the potential background fluorescence from the adhesive. We therefore need to limit the amount of adhesive applied to nanoscale, so that we don't get excessive background or a drastic change in

the optical modes from e.g. the formation of glue droplets in the coupling region.

The details of the above aspects will be illustrated in the workflow discussed in the following sections, where we demonstrate the fiber-coupling process of the angle-implanted nanobeams discussed in section 3.2.

4.4.1. Workflow of gluing the nanobeam to the tapered fiber

To glue the nanobeam to the fiber, we first mount the diamond with the free-hanging nanobeams (fig. 3.5) onto the slip-stick positioner and bring a nanobeam into contact with a blunt glass tip (tip radius ∼ 5 μm) attached in place of the tapered fiber. We drive the positioner such that the tip pushes the nanobeam sideways until it breaks off and sticks to the tip (fig. 4.5(a), i). We then remove the diamond substrate, replace it with a silicon carrier chip, and temporarily place the nanobeam on the chip edge (fig. 4.5(a), ii).

To apply the glue, we replace the blunt tip with the tapered fiber and the nanobeam carrier chip with a chip carrying a small (∼mm-size) droplet of glue (Norland Optical Adhesive 86H). Monitoring through the objective, we dip the fiber into the droplet and then pull it out at a speed of about 1 μm/s (fig. 4.5a, iii).

While this speed is not a precise, quantitative requirement, we note that it is crucial to keep the pullout speed *low*. This is to ensure that only a thin layer of glue forms on the fiber. Specifically, the effect of different pulling speed out of the glue droplet is illustrated in fig. 4.6: at about 50 μm/s, micron-scale glue droplets are clearly visible along the fiber taper.

We then glue the fiber to the nanobeam in a way that aims to maximize the optical coupling efficiency: We re-mount the nanobeam-carrier chip and bring the glue-covered fiber into contact with the nanobeam lying on the chip edge (fig. 4.5(a), iv). At this stage, the large contact area between nanobeam and carrier causes the beam to remain stuck to the carrier chip. This enables adjusting the relative position between fiber and nanobeam while monitoring the NV photoluminescence that we excite and detect through the fiber (fig. 4.5(b)).

When the detected photoluminescence is maximal, we fix the fiber position and illuminate the fiber-nanobeam assembly with a UV lamp (Thorlabs CS2010) to cure the glue. After curing, the bonding between the fiber and the nanobeam is sufficiently strong to overcome the adhesion to the carrier, such that we can detach the glued assembly (fig. 4.5(a), v). White-light and through-fiber-excited-photoluminescence images show the resulting fiber-coupled nanobeam sensor with the NV centers embedded at the tip (fig. 4.5(c)). To further enhance the gluing stability, we unmount the device and bake it (along with the holder it is mounted onto) on a hot plate for about 8 hours at 80 °C.

We find that the glued connection is sufficiently robust to remain intact upon vertical contact with e.g. a sample surface and subsequent micron-scale elastic deformation of the fiber, up until the limit when the fiber tip itself breaks due to
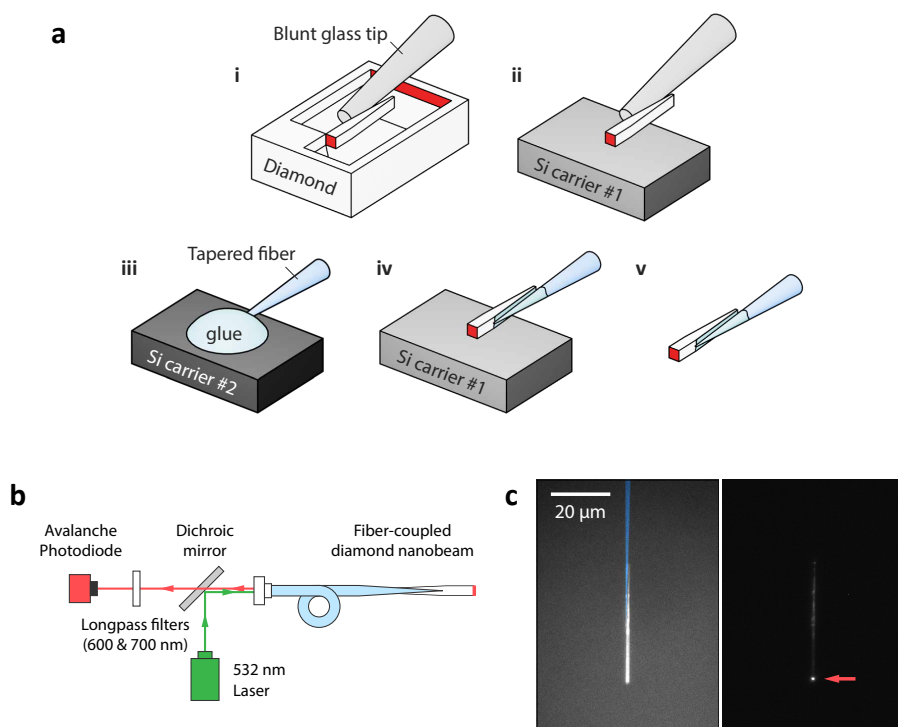
Figure 4.5 - **Assembling the glued fiber-coupled nanobeam sensor with optimized photon collection efficiency. (a)** Assembly workflow using optical glue: (i) A blunt glass tip is used to break the nanobeams off the diamond substrate; (ii) The blunt tip places the nanobeam at the edge of a silicon carrier; (iii) Optical glue is applied to the tapered fiber by dipping the fiber tip into a glue droplet on another carrier chip, and then retracting the fiber; (iv) The glue-covered tapered fiber is brought into contact with the nanobeam on the edge, and the glue is cured with UV illumination after optimizing the coupling between the fiber and the nanobeam; (v) The glued fiber-nanobeam is retracted from the carrier edge. **(b)** Simplified schematics of the optical setup. Two long-pass filters at 600 nm and 700 nm are placed in front of the photodiode to reduce background photoluminescence. **(c)** Microscope image of the glued fiber-nanobeam assembly under ambient illumination (left, the fiber is false colored in blue) and with through-fiber 532 nm laser excitation (right, with the red arrow indicating the end of the beam). Both images are taken with a 650 nm long pass filter in front of the camera to block the excitation laser.
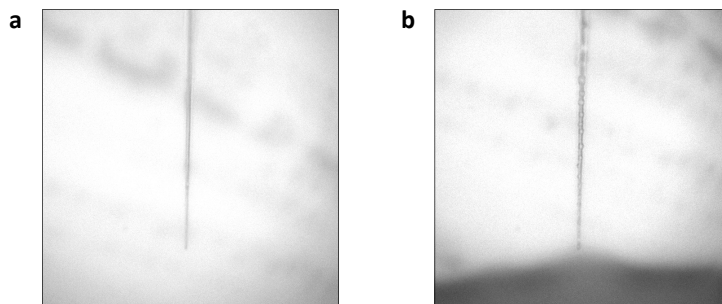
Figure 4.6 - **Microscope images of the tapered fiber after dipping into and retracting from the glue. (a)** Retracting with a speed of ~ 1 μm/s. **(b)** Retracting with a speed of ~ 50 μm/s. Micron-scale droplets are clearly visible.

excessive deformation[2]. This makes it possible to be used as a scanning-probe for in-contact operation or potentially inside biological tissues.

4.4.2. Behavior of background fluorescence

Despite the effort of limiting the amount of glue applied, we *do* still observe a distinct background autofluorescence after curing the glue. At the same time, we also observe the bleaching of this background upon continuous illumination. Although the attempt of quantifying the bleaching behavior did not yield any conclusive result, probably due to its dependence on other varying environmental parameters, the observations are still discussed here to provide practical insight.

A typical time trace of measured photoluminescence upon continuous laser illumination is shown in fig. 4.7, where a distinct decay behavior is visible. Yet this decay curve cannot be fitted accurately to a simple exponential decay, but rather a sum of *two* exponential decays with different time constants. This could indicate the existence of multiple factors affecting the collected PL: the bleaching of glue fluorescence and fiber autoluminescence, the drift of coupling efficiency, change in room temperature, etc. We also note that the values of fitted parameters in fig. 4.7 are not reproducible over measurements repeated at different times, probably also due to the complicated dependence on various environmental parameters.

Nevertheless, we can still conclude that the background fluorescence can be suppressed by continuous bleaching. Therefore, for all the characterization and imaging measurements that will be discussed in section 5.3 and section 6.2, the device has already been continuously illuminated with green laser light for days to ensure the maximal bleaching of background before running the actual

---

[2]Since the tapered fiber tip is still extremely fragile from a macroscopic perspective, handling of these devices (mounting, unmounting, transporting, etc.) should still be carried out with extreme caution.
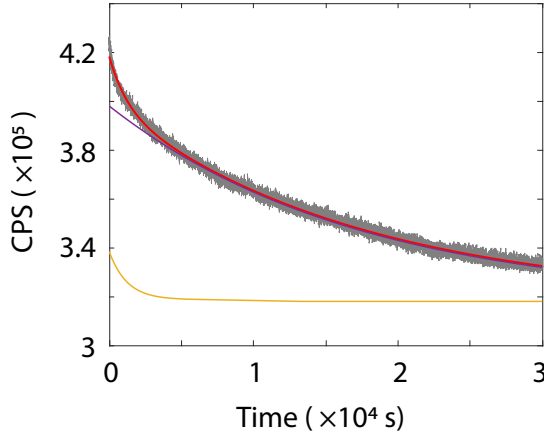
Figure 4.7 - **Photoluminescence time trace measured from a glued fiber-nanobeam assembly upon continuous laser illumination.** $100\,\mu W$ laser is sent into the fiber, and the photoluminescence (long-pass filtered at $600\,nm$) is measured through the course of $\sim 8\,h$ and plotted in grey. Red curve plots the double exponential fit. The two components are plotted in yellow and purple, with corresponding time constants of $1.2 \times 10^3\,s$ and $1.7 \times 10^4\,s$ (i.e. $\sim 20\,min$ and $\sim 4.8\,h$) respectively.

measurement. The further characterization of the remaining background under such conditions will be discussed in section 5.3.1.

4.5. Alternative approach: Nanobeam manipulation with focused ion beam (FIB)

Aside from gluing, we also spent some time exploring alternative, glue-free approaches of deterministic and robust fiber-nanobeam coupling, so that no extra background is introduced. One of these attempts is to use a focused ion beam (FIB) system due to its ability of sample manipulation on the nanoscale under live SEM monitoring, as widely used in the preparation of TEM lamellas [11]. We will elaborate in this section why we did *not* proceed with this approach in the end, yet we do not fully exclude the potential to eventually realize glue-free robust coupling using FIB. Therefore the efforts we made will still be briefly discussed for possible future reference.

Two approaches of nanobeam manipulation are tested with a FIB-SEM system (FEI Helios G4 CX, operating with Ga^+ ion at $30\,kV$) and illustrated in fig. 4.8. In the first approach (fig. 4.8(a),(b)), we mount both the diamond substrate and the tapered fiber into the FIB chamber. Inspired by the TEM lamella preparation process, we tried to approach the nanobeam with the built-in nanomanipulator (Thermo Scientific EasyLift EX), and pick up the nanobeam by first using ion-beam induced
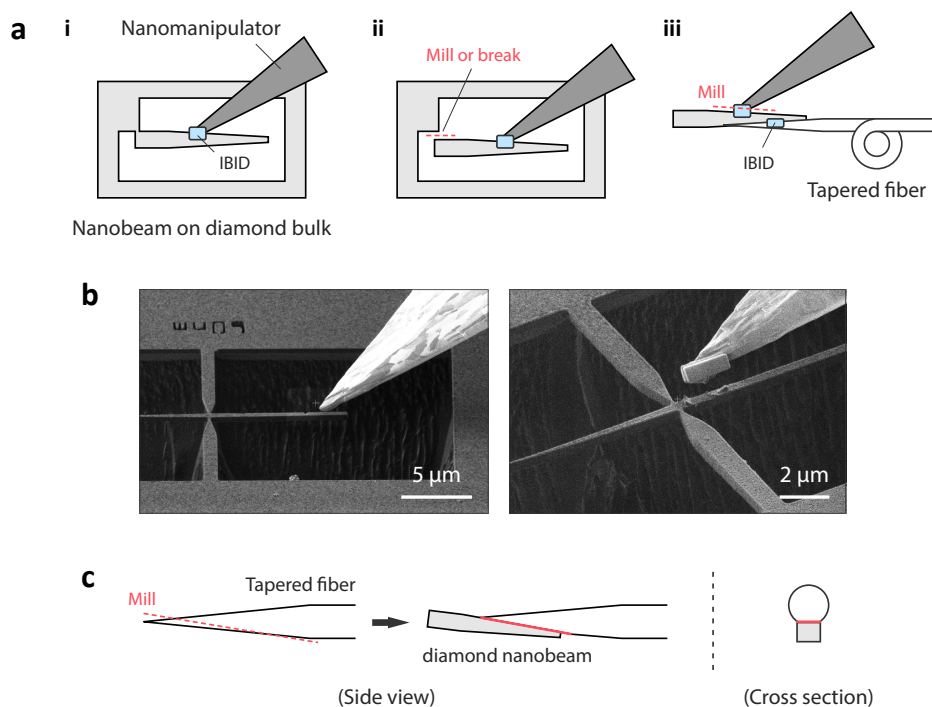
Figure 4.8 - **Attempt to couple the nanobeams to tapered fibers using focused ion beam (FIB). (a)** Schematics of envisioned nanobeam manipulation process with the nanomanipulator. (i) The nanomanipulator is fixed to the diamond nanobeam with ion beam induced deposition (IBID) at the contact point. (ii) The nanobeam is broken off the diamond substrate by either ion beam milling at the tether or directly pushing with the manipulator. (iii) The nanomanipulator brings the nanobeam in contact with the tapered fiber which is also mounted in the FIB chamber. After adjusting their relative position under SEM inspection, IBID again fixes the nanobeam to the tapered fiber, and the nanomanipulater can then be detached by milling away the first IBID area. **(b)** SEM images taken during a trial run, showing the nanomanipulator approaching the nanobeam (left) and an unsuccessful attempt of fixing the nanobeam to the manipulator using IBID platinum (right, the rectangular structure at the manipulator tip is the deposited platinum). **(c)** Schematics of envisioned cut-fiber approach. Ion beam milling is used to remove part of the fiber taper and create a flat surface for larger contact area between the nanobeam and the fiber. The cut surface is marked with the red line.

deposition (IBID) of platinum as a "glue" to fix the nanobeam to the manipulator tip, then break the tether either mechanically or by ion beam milling. Once the nanobeam is picked up, it can then be aligned and fixed to the tapered fiber under SEM inspection also using IBID (fig. 4.8(a), iii). The second approach, on the other hand, is simpler and only involves the tapered fiber: We tried to use ion beam milling to shape the fiber tip such that it maintains a gradually tapered profile, yet a flat surface is created to function as the contact area between the fiber and the nanobeam. This way the adhesion can potentially by increased by the significantly larger contact area.

In reality, however, the main reason to make both methods practically unfavorable is the complication to deal with charge-induced distortion during milling or IBID. Since both the diamond and the fiber are insulators, conductive coating (gold in our case) is needed to make FIB operation possible on the desired sub-micron length scale. Yet such complicated nanostructures are not trivial to be coated uniformly, and might still suffer from charging after coating due to the free-hanging geometry. Also, in order not to introduce extra effects on the optical readout, the coating will need to be removed afterwards, which is again not trivial given the fragility of the assembly.

The other potential risk of these methods is the gallium ion implantation and SEM-induced hydrocarbon deposition near the NV centers in the nanobeam. Although in principle neither approach requires ion beam milling or IBID directly at the NV location, the range at which the ion implantation diffuses and their possible proximity effect on NV centers need to be characterized. As such, the above mentioned practical complications render the FIB approaches unfavourable compared to the gluing workflow.

Acknowledgment

References

[1] A. Dréau, M. Lesik, L. Rondin, P. Spinicelli, O. Arcizet, J. F. Roch, and V. Jacques. "Avoiding power broadening in optically detected magnetic resonance of single NV defects for enhanced dc magnetic field sensitivity". In: *Physical Review B* 84.19 (Nov. 2011), p. 195204. ISSN: 1550235X. DOI: 10.1103/PhysRevB.84.195204.

[2] J. D. Thompson, T. G. Tiecke, N. P. de Leon, J. Feist, A. V. Akimov, M. Gullans, A. S. Zibrov, V. Vuletić, and M. D. Lukin. "Coupling a single trapped atom to a nanoscale optical cavity". In: *Science* 340.6137 (June 2013), pp. 1202–1205. ISSN: 0036-8075. DOI: 10.1126/science.1237125.

[3] I. Marinkovic. " Optomechanical devices in the quantum regime". PhD thesis. TU Delft, 2019.

[4] L. Magrini, R. A. Norte, R. Riedinger, I. Marinković, D. Grass, U. Delić, S. Gröblacher, S. Hong, and M. Aspelmeyer. "Near-field coupling of a levitated nanoparticle to a photonic crystal cavity". In: *Optica* 5.12 (Dec. 2018), p. 1597. ISSN: 23342536. DOI: 10.1364/optica.5.001597.

[5] I. Marinković, M. Drimmer, B. Hensen, and S. Gröblacher. "Hybrid integration of silicon photonic devices on lithium niobate for optomechanical wavelength conversion". In: *Nano Letters* 21.1 (Jan. 2021), pp. 529–535. ISSN: 15306992. DOI: 10.1021/acs.nanolett.0c03980.

[6] A. L. Ruoff. "On the yield strength of diamond". In: *Journal of Applied Physics* 50.5 (May 1979), pp. 3354–3356. ISSN: 0021-8979. DOI: 10.1063/1.326378.

[7] A. Banerjee, D. Bernoulli, H. Zhang, M. F. Yuen, J. Liu, J. Dong, F. Ding, J. Lu, M. Dao, W. Zhang, Y. Lu, and S. Suresh. "Ultralarge elastic deformation of nanoscale diamond". In: *Science* 360.6386 (Apr. 2018), pp. 300–302. ISSN: 10959203. DOI: 10.1126/science.aar4165.

[8] M. J. Burek, C. Meuwly, R. E. Evans, M. K. Bhaskar, A. Sipahigil, S. Meesala, B. MacHielse, D. D. Sukachev, C. T. Nguyen, J. L. Pacheco, E. Bielejec, M. D. Lukin, and M. Lončar. "Fiber-coupled diamond quantum nanophotonic interface". In: *Physical Review Applied* 8.2 (Aug. 2017). ISSN: 23317019. DOI: 10.1103/PhysRevApplied.8.024026.

[9] S. Mi, A. Toros, T. Graziosi, and N. Quack. "Non-contact polishing of single crystal diamond by ion beam etching". In: *Diamond and Related Materials* 92 (Feb. 2019), pp. 248–252. ISSN: 09259635. DOI: 10.1016/j.diamond.2019.01.007.

[10] R. A. Parker, J. Arjona Martínez, K. C. Chen, A. M. Stramma, I. B. Harris, C. P. Michaels, M. E. Trusheim, M. Hayhurst Appel, C. M. Purser, W. G. Roth, D. Englund, and M. Atatüre. "A diamond nanophotonic interface with an optically accessible deterministic electronuclear spin register". In: *Nature Photonics* 18.2 (Feb. 2024), pp. 156–161. ISSN: 1749-4885. DOI: 10.1038/s41566-023-01332-8.

[11] J. Mayer, L. A. Giannuzzi, T. Kamino, and J. Michael. "TEM sample preparation and FIB-induced damage". In: *MRS Bulletin* 32.5 (May 2007), pp. 400–407. ISSN: 0883-7694. DOI: 10.1557/mrs2007.63.

4

5

Characterization of the fiber-coupled diamond nanobeam probes

🎵 ·|||·|·||·|·|||··

It was multidirectional,
wasn't there to determine why.
It was plainly invisible,
like the depth of the blue sky.

Interdimensional · Cosmo Sheldrake

Abstract

In this chapter, we demonstrate through-fiber readout of the NV centers in the assembled nanobeam devices and benchmark their performances. For the nanobeams with homogeneous NVs and coupled via van der Waals forces, we demonstrate through-fiber NV-ESR measurements in section 5.2, and apply two independent methods on the same device to estimate the fiber-nanobeam coupling efficiency. A similar characterization and coupling efficiency estimation is carried out for angle-implanted nanobeams in section 5.3. Also in this section, we further identify the effect of NV centers residing along the sidewalls of the nanobeams as a result of implantation misalignment. We show that we can read out the end-facet NVs with decent efficiency and isolate their contribution, enabling the determination of magnetic field at the beam end-facet in scanning magnetometry measurements.

Introduction

The ability to excite and readout the NV spins inside the diamond nanobeams lies at the basis of their application in magnetometry. Throughout this thesis, two generations of fiber-coupled nanobeam probes have been developed: one with ensemble NVs across the nanobeam and coupled using direct van der Waals forces, and one with angle-implanted NVs at the tip of the beam and coupled using optical glue. From this chapter on, we will refer to the two generations as the *homogeneous-NV* probes and the *tip-NV* probes. Their performance in terms of NV properties and readout efficiencies will be characterized in this chapter.

Specifically, the estimation of optical coupling efficiencies will be discussed in detail, as it directly determines the magnetic sensitivity of our devices. Near-unity coupling efficiencies for such adiabatic coupling interfaces have been demonstrated in previous works through both simulation and measurements [1, 2], yet the presence of the nanobeam end facet and the NV centers being close to the end facet introduce extra complication for our devices. On the one hand, it limits the theoretical maximum efficiency of NV readout as part of the photoluminescence emission is in the opposite direction to the fiber. On the other hand, it is not possible to measure the coupling efficiency through transmission or reflection of excitation laser. We therefore use methods such as the optical saturation of NVs and absorption cross-section to give a reasonable estimation, discussed in the sections below.

5.1. Optical setup for characterizing fiber-coupled diamond nanobeams

The optics for addressing NV centers in general consist of two parts: the green path for excitation and the red path for detection. The only difference for our fiber-based device is that both paths will be coupled into (or out of) a single-mode fiber. This is illustrated in the simplified schematics in fig. 5.1, and the same optical setup is used for all the optical measurements in the rest of the thesis.

The 532 nm excitation laser is sent through a single mode (SM) fiber (S630-HP, same as the tapered fiber) for mode filtering, and further short-pass filtered at 550 nm to eliminate the residual 1064 nm components from the laser emission. A dichroic mirror (567 nm short pass) then directs the excitation laser light towards the fiber coupler and separates it from the photoluminescence coming from the fiber. This photoluminescence is further long-pass filtered at 600 nm to get rid of the remaining green laser reflected from the fiber coupler, and detected using a fiber-coupled avalanche photodiode (APD, Laser Component COUNT-500N-FC). For the measurements discussed in section 5.2, ND filters are added for the ensemble NV photoluminescence to stay within the measurement range of our APD. The effect of adding an extra 700 nm long-pass filter will be discussed in section 5.3.

For the rest of this chapter, the input optical power is measured with a power meter in front of the fiber coupler, denoted as P_1 in fig. 5.1. The actual optical power coupled into the fiber is denoted as P_2 and will be characterized separately
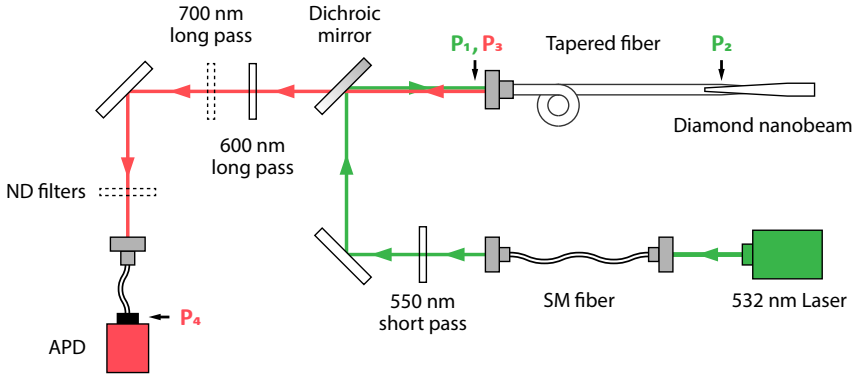
Figure 5.1 - **Optical setup (simplified) for characterizing fiber-coupled diamond nanobeams.** Components in dashed outline are present only in certain measurements, specified in the corresponding sections of the thesis. $P_1 \sim P_4$ represents the power of excitation laser or red photoluminescence (marked by the font color) used to determine efficiencies in the optical path, measured at locations indicated by the arrow.

in the estimation of fiber-nanobeam coupling efficiencies, along with the collection efficiency of red photoluminescence P_4/P_3.

5.2. Characterization of the homogeneous-NV nanobeam probes

In this section, we discuss the readout and coupling efficiency characterization of the homogeneous-NV nanobeam probes. These nanobeams are fabricated using ensemble NV diamond (Element-six DNV-B14), with an estimated NV concentration of 4.5 ppm [3], corresponding to $N \approx 4.5 \times 10^6$ NVs per nanobeam (40 μm long, maximum cross section 0.5×0.5 μm^2 and tapered down to $\sim 0.1 \times 0.5$ μm^2 over 37 μm length).

5.2.1. NV-ESR readout and background fluorescence

To confirm that the photoluminescence we collect through the fiber is indeed from the NV centers in the nanobeams, we first apply microwaves to the nanobeam and perform continuous-wave ESR measurements. Furthermore, it is also important to gain insight on possible sources of non-NV photoluminescence in order to characterize and potentially improve the signal-to-background ratio of our measurement. For the fiber-coupled nanobeams we discuss in this section, the non-NV contribution is mainly the autoluminescence from the fiber itself. We therefore also characterize the power dependence of the fiber autoluminescence.

We apply microwaves (Windfreak SynthHD) through a co-planar waveguide (placed
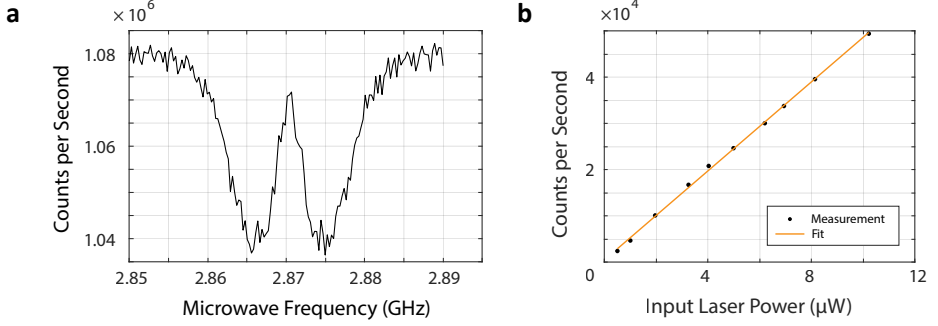
Figure 5.2 - **Through-fiber ESR measurement and background characterization. (a)** NV electron spin resonance (ESR) measurement at zero magnetic field, measured using the setup discussed in section 5.1. 30 nW of excitation laser is sent into the fiber and the photoluminescence response as a function of applied microwave frequency is plotted. **(b)** Characterization of fiber autoluminescence in our experiment. Photoluminescence from a section of S630-HP fiber without nanobeams attached is measured as a function of input laser power. The length of the fiber is kept the same as the tapered fiber coupled to nanobeams. A linear fit gives an autoluminescence rate of $\Gamma_{\text{fiber}} = 4.8 \times 10^3 \, \text{s}^{-1} \mu\text{W}^{-1}$.

~ 50 μm below the nanobeam, with 19 dBm power at the source output) to drive the electron-spin resonance (ESR) of the NV centers. Figure 5.2(a) shows a characteristic ESR spectrum measured through-fiber from our device, where the dips result from the microwave-driven transition between NV spin states $|m_S = 0\rangle \rightarrow |m_S = \pm 1\rangle$. Due to the high NV density, we record the ESR signal with only 30 nW of excitation power. Following the methodology in Ref.[4], we estimate from the ESR spectrum the shot-noise limited magnetic field sensitivity to be $4.2(3) \, \mu\text{T/Hz}^{1/2}$. This value is also limited by the collection efficiency of our optical setup.

Comparing the low-power NV photoluminescence rate of $3.7 \times 10^7 \, \text{s}^{-1} \mu\text{W}^{-1}$ (fig. 5.2(a)) to the independently measured fiber autoluminescence rate of $4.8 \times 10^3 \, \text{s}^{-1} \mu\text{W}^{-1}$ (fig. 5.2(b)) shows that our signal is dominated by the NV photoluminescence, with a signal-to-background ratio of 8×10^3. By normalizing the photon count in fig. 5.2(a) to the total number of NVs N, we estimate the collected photoluminescence rate of a single NV center to be $\Gamma_{\text{NV}}/N = 8.1 \, \text{s}^{-1} \mu\text{W}^{-1} \ll \Gamma_{\text{fiber}}$. Therefore in order to achieve efficient single NV readout where $\Gamma_{\text{NV}}/N \sim \Gamma_{\text{fiber}}$, further effort is needed on both reducing the fiber autoluminescence and increasing the NV photon collection efficiency.

5.2.2. Coupling efficiency estimation: the optical saturation approach

In the geometry of our fiber-nanobeam assembly, we do not have a way to determine the photon coupling efficiency at the nanobeam-fiber interface η_{nf} through the

transmission or reflection of the excitation laser light, as commonly used to characterize such devices [2]. Therefore we adopt two approaches of estimating η_{nf}, discussed in this section and the next. The philosophy of both methods is to estimate the collection efficiency by comparing the measured NV photoluminescence to the *theoretical* expectation based on the intrinsic properties of NV centers.

The first approach is based on the optical saturation behavior of NV centers: As the photon emission of NV centers is essentially from a two-level system (i.e. the same m_S states of the ground state and excited state), the theoretical maximum emission rate of an NV center is fundamentally limited by the finite lifetime of the excited state, and will exhibit saturation behavior with increasing excitation power. Therefore, the collection efficiency of the system can be estimated as the ratio of measured saturated PL intensity and the theoretical value.
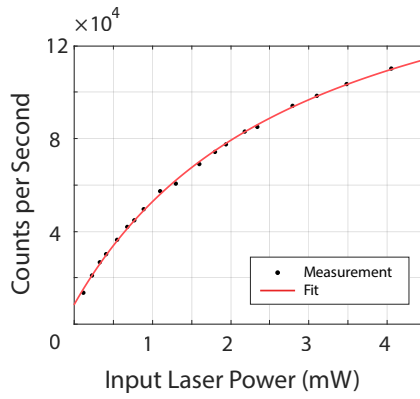
Figure 5.3 - **NV photoluminescence as a function of optical excitation power**, fitted with eq. (5.1) (red curve). The count rate on the y-axis is after neutral-density (ND) filtering by a factor of 6×10^6. Error bars of the data points are not indicated as they are smaller than the dot size.

In practice, we measure the the NV photoluminescence as a function of the optical excitation power P in fig. 5.3. Assuming a simple two-level model for the NV photodynamics, the NV photoluminescence is limited by the NV's spontaneous emission rate $\gamma = 1/(13 \text{ ns})$ [5]. As such, the photon count rate Γ detected by our APD can be described by:

$$\Gamma = \eta N \gamma \frac{P}{P + P_{\text{sat}}} + \Gamma_{\text{dark}}. \tag{5.1}$$

Here, η is the fraction of total number of photons emitted by the NVs that is detected by our APD, P_{sat} is the optical saturation power [4], and Γ_{dark} is a power-independent background rate (including e.g. APD dark counts). Because of the strong NV luminescence (fig. 5.3 and fig. 5.2(b)), we can omit the contribution of fiber autoluminescence and fit eq. (5.1) to the data in fig. 5.3. We extract $\eta = 5.0(2) \times 10^{-10}$. Writing $\eta = \eta_{\text{ND}} \eta_{\text{D}} \eta_{\text{nf}}$, where $\eta_{\text{ND}} = 1.6 \times 10^{-7}$ is the neutral-density

(ND) filtering factor (fig. 5.1, in order to avoid over-saturating the APD) and $\eta_D = 3.5 \times 10^{-2}$ is the optical efficiency of the other parts of our setup (characterized separately, see section 5.1), we extract the photon coupling efficiency at the fiber-nanobeam interface $\eta_{nf} = 8.6(4)\%$. We note that the relatively small error here derives from the fit uncertainty of η. However, other systematic uncertainties are likely to play a more important role. For example, the two-photon-induced ionization of the NV centers to the neutral charge state could affect the detected photon rate due to the different spectrum of NV^0 centers [6, 7]. We therefore use a second approach to estimate η_{nf}.

5.2.3. Coupling efficiency estimation: the absorption cross section approach

In the second approach, we estimate η_{nf} from the detected NV photoluminescence using a literature value for the NV's absorption cross section for 532 nm laser excitation. Well below saturation power, this approach estimates the theoretically expected PL intensity by estimating the rate of photons falling within the absorption cross section area of all the NVs.

Consider a single NV center inside a diamond nanobeam. If the area of the optical mode cross section inside the beam is approximately the cross section of the nanobeam itself A_{beam}, then the probability for an NV center to absorb a single photon and trigger an excitation will be

$$\mathscr{P} = \frac{\sigma}{A_{beam}} \tag{5.2}$$

where $\sigma = 3.1(8) \times 10^{-21}\,\mathrm{m}^2$ is the absorption cross section of the NV center [8]. Therefore when a total of N_{ph} photons enter a beam containing N_{NV} NVs, the total number of excitations (thus total number of emitted photons) will be

$$N_{PL} = \frac{N_{ph} N_{NV} \sigma}{A_{beam}}. \tag{5.3}$$

Note that the effect of saturation discussed previously is not taken into account here, thus the optical power needs to stay well below saturation for this equation to hold.

Now consider a power of P being sent into the fiber with a fiber-coupling efficiency of η_f. The rate of excitation photons that eventually end up in the beam mode will then be

$$\Gamma_{exc} = \frac{P}{\hbar\omega} \eta_f \eta_{nf} \tag{5.4}$$

where η_{nf} is the nanobeam-fiber coupling efficiency, taking into account the light coupling efficiency at the coupling interface and the efficiency of NV emission coupling into the guided mode (averaged, as this could vary depending on the location of the NV within the nanobeam). Thus the photoluminescence rate will be

$$\Gamma_{PL} = \frac{P}{\hbar\omega} \frac{N_{NV}\sigma}{A_{beam}} \eta_f \eta_{nf} \tag{5.5}$$

and the measured photon rate is (assuming coupling efficiency at the fiber-nanobeam interface is equal for both directions)

$$\Gamma_{\text{meas}} = \frac{P}{\hbar\omega} \frac{N_{\text{NV}}\sigma}{A_{\text{beam}}} \eta_{\text{f}} \eta_{\text{nf}}^2 \eta_{\text{D}} \tag{5.6}$$

where η_{D} is the fraction of photons exiting the fiber that are eventually detected by the APD.

Therefore from eq. (5.6) one can estimate η_{nf} from P and Γ_{meas}, both of which are measured experimentally. For the device mentioned in section 5.2.1, we measured $\Gamma_{\text{meas}} = 1.08 \times 10^6\,\text{s}^{-1}$ at $P = 30\,\text{nW}$. To experimentally determine η_{f}, we connect a non-tapered fiber (same model as the tapered one) in place of the nanobeam-coupled tapered fiber, send in a green laser with power P_1 measured in front of the coupler (fig. 5.1), measure the power P_2 at the output of the fiber and determine $\eta_{\text{f}} = P_2/P_1 \approx 0.35$. For η_{D}, we send in a red laser through the same non-tapered fiber, measure the powers at fiber output (P_3) and the APD fiber output (P_4), and determine $\eta_{\text{D}} = P_3/P_4 \approx 0.035$. Substituting all the numbers into eq. (5.6), we can calculate the coupling efficiency at the interface

$$\eta_{\text{nf}} = 14(2)\%. \tag{5.7}$$

In contrast with the first approach, this approach does not require saturating the NV photoluminescence response and can thus be conducted at very low (nW) laser power. This reduces the potential influence of two-photon-induced ionization of the NV centers to the neutral charge state [6, 7].

5.2.4. Additional characterization of different devices

The coupling efficiency of our device is sensitive to the alignment of the tapered fiber and the diamond nanobeam. The precise alignment is hindered by the abrupt motion of the fiber-nanobeam when the tether breaks, thus inducing a variation of coupling efficiency across different devices. To illustrate this, aside from the device characterized previously, in fig. 5.4 we show ESR measurements on four different nanobeams from the same fabrication batch and coupled to the same tapered fiber. The coupling efficiencies for these devices are estimated using the absorption cross section method, exhibiting a variation between 9% and 19%.

Furthermore, as a reference measurement, we also measured the ESR of the nanobeams that are still attached to the bulk. Without the breaking process, this allows optimizing the relative position between the fiber and the nanobeam, by monitoring the photon count while adjusting the positioning of the fiber tip, and thereby providing an estimation on the *optimal* coupling efficiency. Such a measurement is performed on a 30 μm beam (maximum cross section $0.5 \times 0.5\,\mu\text{m}^2$, tapered down to $\sim 0.1 \times 0.5\,\mu\text{m}^2$ over 27 μm length) attached to the bulk, with optimized photon counts (fig. 5.5(a)). This measurement yields $\eta_{\text{nf}} = 19(3)\%$.

As an additional note, in order to identify the origin of the ESR dip splitting present in all measurements (in the absence of external field), we also measured the ESR spectrum on the bulk of the same diamond through free space confocal
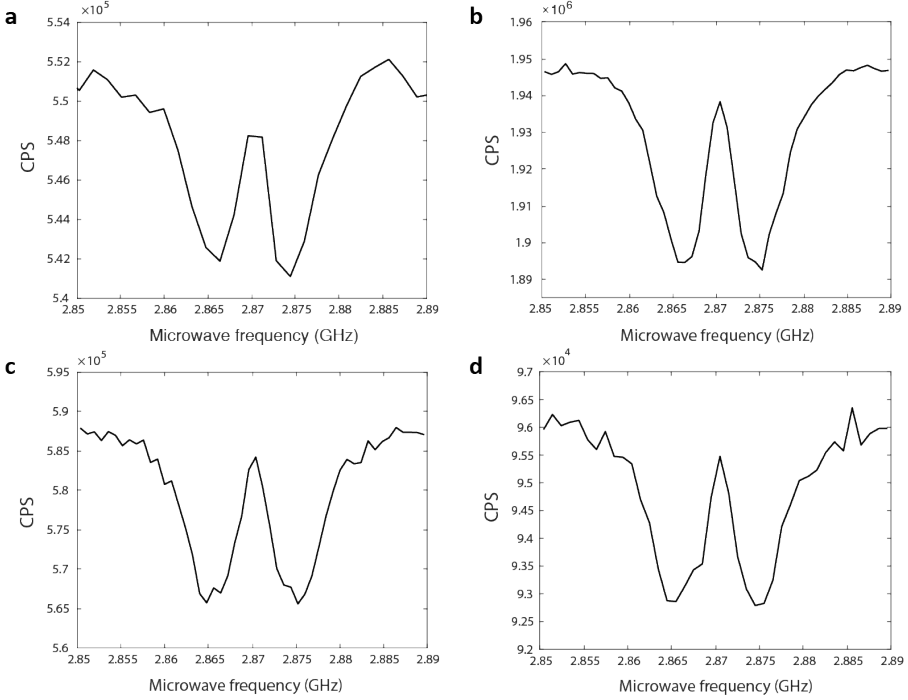
Figure 5.4 - **Through-fiber ESR spectrum of four different nanobeam devices**, measured at excitation power of (a) 35 nW; (b) 30 nW; (c) 25 nW; (d) 40 nW. The measured photoluminescence is after ND 1.3 filtering. Using the absorption cross section method explained in the previous section, coupling efficiencies on the fiber-nanobeam interfaces are estimated to be (a) 9(1)% (b) 19(3)% (c) 11(2)% (d) 16(2)%.

illumination and collection, shown in fig. 5.5(b). Here we also observe the same splitting, indicating that this is intrinsic to the specific diamond we use rather than the nanobeam geometry. Actually, the splitting of ESR resonance at zero external magnetic field is known to occur for such high-density NV ensembles, induced by the random local *electric* field of the ensemble. This is thoroughly studied in ref.[9].

5.2.5. Discussion on the efficiency estimations

We expect the found values for η_{nf} to be conservative estimates of the nanobeam-fiber coupling efficiencies due to the assumptions that all NV-emitted photons are radiated into the beam and towards the nanobeam-fiber interface, and because our two-level model neglects the non-radiative decay path via the singlet state that reduces the total photon emission rate [10]. Also, since the optical lifetime of NV centers depends on the electromagnetic environment, the lifetime of NV centers in
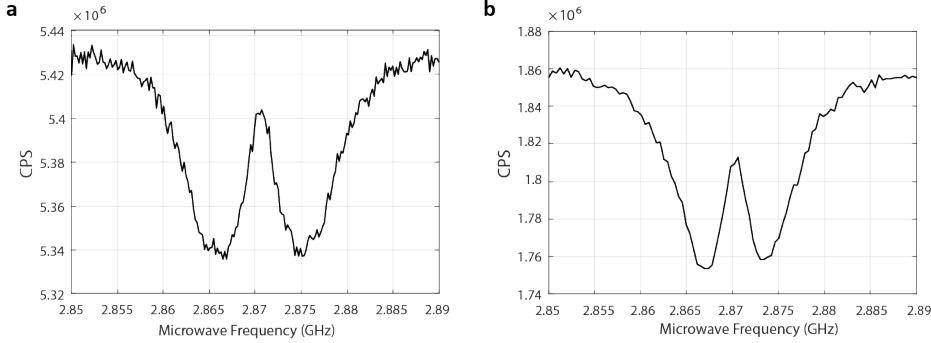
Figure 5.5 - **Reference ESR measurements for identifying the effect of the bulk substrate.** **(a)** ESR spectrum of a nanobeam that remains attached to the bulk of the diamond, measured at excitation power of 31 nW. This beam has a total length of 30 μm instead of 40 μm for the beams measured in figs. 5.2 and 5.4, and for this measurement we have a different $\eta_D = 0.042$ due to switching of the collection fiber in front of the APD. The efficiency on the fiber-nanobeam interface is estimated to be 19(3)%. **(b)** ESR spectrum measured on the bulk of the same diamond. Free space laser excitation of 350 nW is focused on the surface of the diamond via a 50× microscope objective in a confocal microscope, and NV photoluminescence is also collected using the same objective.

our nanobeams could be longer than that of NV centers in bulk diamond due to the lower refractive index of air [11]. By using the bulk lifetime, we obtain an estimation of the collection efficiency on the conservative side.

Compared to the state-of-the-art $\eta_{nf} > 90\%$ reported in Refs. [1, 2] for single-wavelength (sub-nm spectral width) readout, an important difference in our device is the wide-band spectrum (bandwidth ∼ 200 nm) of the collected NV photoluminescence. Also, as discussed previously, the precise alignment of the fiber tip required to optimize the coupling efficiency is affected by the abrupt motion of the nanobeam when the tether breaks. Other factors that reduce the efficiency include the roughness on the sidewalls and bottom side of the nanobeams, which can be improved by optimizing the fabrication process, for instance by ion-based polishing of the nanobeam sidewall [12] or improved diamond etching.

We note that for these devices, the fiber autoluminescence would still exceed the single-NV photoluminescence by about an order of magnitude even in the limit $\eta_{nf} \to 1$ (according to eq. (5.6), $\Gamma_{NV,max}/N = 4.1 \times 10^2 \, s^{-1} \, \mu W^{-1}$). This indicates that single-NV sensing will only be possible if the fiber autoluminescence can be further reduced, as will be discussed in section 5.3.1.

5.3. Characterization of the tip-NV nanobeam probes

In this section, we use similar methods to characterize the NV-readout properties of the tip-NV nanobeam probes. For these probes, a small ensemble (~1000) of NV centers is deterministically implanted to the nanobeam tip, and the nanobeam is robustly glued to the tapered fiber with a thin layer of UV-curing optical glue.

5.3.1. Characterization of through-fiber NV photoluminescence readout
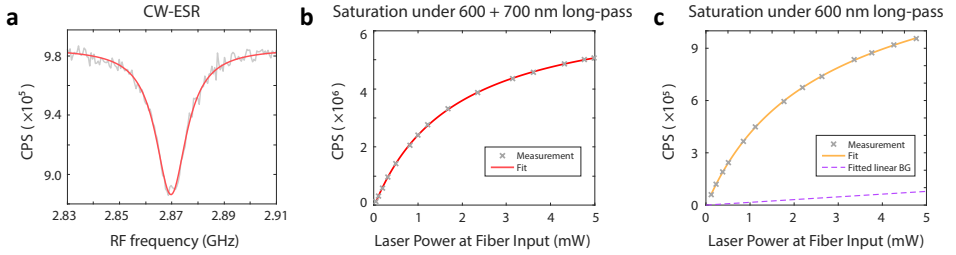
Figure 5.6 - **Characterizing the through-fiber NV photoluminescence readout.** **(a)** Electron spin resonance (ESR) signal of the NV centers in the nanobeam measured through the fiber, measured with 30 μW of laser excitation (measured in free space in front of the fiber coupler) at zero external magnetic field, under 600 nm + 700 nm long-pass filtering. A Lorentzian fit (red curve) yields a contrast of 10.0(2)% and a 7.1(3) MHz zero-field full width half maximum. **(b)** Optical saturation of measured photoluminescence, measured under 600 nm + 700 nm long-pass filtering. Additional neutral density filtering of ND1.5 is applied before the APD, in order for the PL to stay within the measurement range of our APD. Measured data (grey cross) are fitted with eq. (5.8) (red curve). **(c)** Optical saturation measured under 600 nm long-pass filtering, and the fit using eq. (5.8) (orange curve). Additional neutral density filtering of ND3 is applied. The non-zero linear background extracted from the fit is plotted as the purple dashed line.

Compared to the van der Waals-coupled homogeneous-NV probes, the extra gluing step could result in an extra source of background photoluminescence. Therefore, aside from the optical saturation measurement, we perform further analysis on saturation and ESR measurements under different color filtering regimes to quantify the effect of background photoluminescence.

Similar to the previous section, we first confirm the existence of NV photoluminescence through the ESR spectrum of the fiber-coupled nanobeam sensor (fig. 4.5(b)). Here we use a much higher 30 μW excitation power compared to the previous section as the number of NVs is orders of magnitude lower. We drive the ESR by applying a microwave current through a stripline on a chip positioned

$\sim 50\,\mu\text{m}$ below the nanobeam. We find that adding a 700 nm long-pass filter in the detection path yields a 10.0(2)% ESR contrast (fig. 5.6(a)), which is 60% larger than when filtering with only a 600 nm long-pass filter (fig. 5.7). This indicates a strong background photoluminescence in the $600 \sim 700\,\text{nm}$ range.

To determine the origin of this background, we measure the optical saturation under two filtering conditions: 600 nm + 700 nm long-pass filters for the first measurement (fig. 5.6(b)), and a single 600 nm long-pass filter for the second measurement (fig. 5.6(c)). We fit both datasets to the model

$$I(P) = I_{\text{sat}}\frac{P}{P + P_{\text{sat}}} + kP + I_0. \tag{5.8}$$

As discussed previously, the first term models the optical saturation of NV centers [4], characterized by a saturation power P_{sat} and an asymptotic intensity I_{sat}. The second term accounts for background photoluminescence, produced by e.g. the fiber or the glue, which we assume to be linear with laser power with proportionality constant k [13]. The final term I_0 represents the dark count rate of our detector.

For the 600 nm+700 nm filtered measurement, the fit yields $k = -0.01(7) \times 10^6\,\text{s}^{-1}\,\text{mW}^{-1}$, or $k = 0$ if we bound k to $k > 0$ (fig. 5.6(b)). We conclude that the detected fiber or glue autoluminescence above 700 nm is insignificant compared to the NV luminescence, indicating potential for reaching the single-spin regime. For the 600 nm filtered measurement, the fit yields $k = 0.016 \pm 0.015 \times 10^6\,\text{s}^{-1}\,\text{mW}^{-1}$ (fig. 5.6(c)). As such, the ratio between the NV signal and the background is still $I_{\text{sat}}/kP_{\text{sat}} \approx 37 \gg 1$ for the low powers $P \ll P_{\text{sat}}$ used in our measurements. Therefore, this small linear background PL cannot explain the observed difference in ESR contrast between the two filtering regimes (fig. 5.6(a)).

Therefore to further identify the composition of the measured photoluminescence, we analyze two ESR measurements with the same laser ($P = 11\,\mu\text{W} \ll P_{\text{sat}}$ at fiber input) and microwave power (19 dBm at output). The only difference between the two measurements is the presence/absence of an extra 700 nm filter. The normalized spectra are plotted in fig. 5.7.

Under the assumption that the background PL from the fiber and the glue are both linear to input laser power, the previous saturation measurement can already exclude their contribution for the low-power measurement. We therefore attribute this increase in contrast to the fluorescence from NV^0 charge state, which does not contribute to the ESR contrast and has a different spectral distribution. In this case the total PL consists only of the NV^- contribution I_- and NV^0 contribution I_0, and the ESR contrast can be expressed as

$$C_i = \frac{rC_-I_{-,i}}{rI_{-,i} + (1-r)I_{0,i}}, \quad i = 1,2 \tag{5.9}$$

in which $C_1 = 8.7(3)\%$, $C_2 = 5.5(1)\%$ are the measured contrast under the two filtering regimes, C_- denotes the intrinsic ESR contrast of NV^- independent of filtering, and r is the fraction of NV^- PL in the total PL ($0 < r < 1$).

We can calculate the normalized PL intensities I_- and I_0 from the spectral density
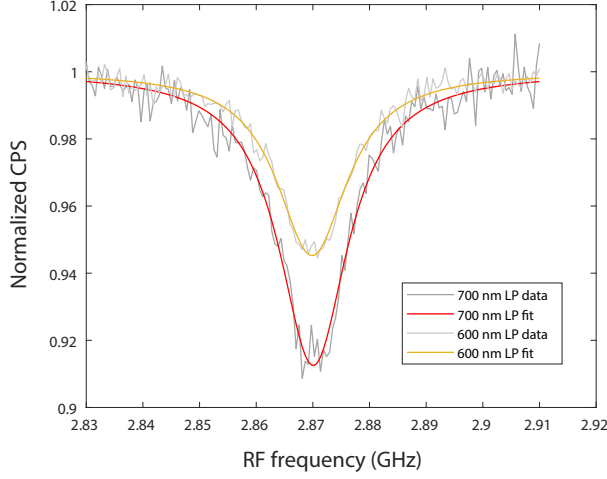
Figure 5.7 - **Normalized through-fiber ESR measurement at two different filtering regimes.** Both measurements are taken on the same device under the same input laser and microwave power, with the only difference being the presence/absence of the extra 700 nm long-pass filter. Lorentzian fits are performed for both spectra, yielding contrasts of 8.8% for 600 nm+700 nm filtering (red), and 5.5% for 600 nm filtering (orange).

distribution $P(\lambda)$ of NV^- and NV^0:

$$I_{-,i} = \int_{\lambda_i}^{\infty} P_-(\lambda)\,d\lambda, \quad I_{0,i} = \int_{\lambda_i}^{\infty} P_0(\lambda)\,d\lambda, \quad i = 1,2 \tag{5.10}$$

Using the spectrum data from ref.[14], we have

$$I_{-,1} = 0.45(9); \quad I_{-,2} = 0.98(1); \quad I_{0,1} = 0.10(5); \quad I_{0,2} = 0.68(7) \tag{5.11}$$

where the relative uncertainties are estimated from the discrepancy between spectra reported in refs. [14–16], possibly due to the sample and measurement conditions. Substituting these values into eq. (5.9) allows us to solve for C_- and r:

$$r = 0.4(2), \quad C_- = 0.12(3). \tag{5.12}$$

The relatively low NV^- concentration obtained here could be because of the presence of NVs in the sidewalls along the nanobeam, which will be discussed in the next section. These NVs are closer to surface, and are therefore more prone to ionization upon surface defect. The value of r could also be underestimated if part of the non-NV background also has a non-linear power dependence.

We thereby conclude that the background photoluminescence originates predominantly from neutral NV centers in the diamond nanobeam. Increasing the NV^- to NV^0 ratio, for instance by diamond surface treatments [17], is therefore of primary importance for future improvements of our fiber coupled sensors.

5.3.2. Identifying implantation misalignment through scanning magnetometry

Another extra complication involved compared to the homogeneous-NV probes is the angled implantation process. Although in section 3.2.3 we confirmed the spatial distribution of PL is concentrated at the beam tip, we cannot rule out the possible distribution of low-density NVs *along* the nanobeam as a result of finite misalignment between the implantation and the nanobeam orientations (which is almost inevitable). Therefore in this section, we perform a scanning magnetometry measurement using the tip-NV probe, and elaborate on the effect of misaligned implantation.
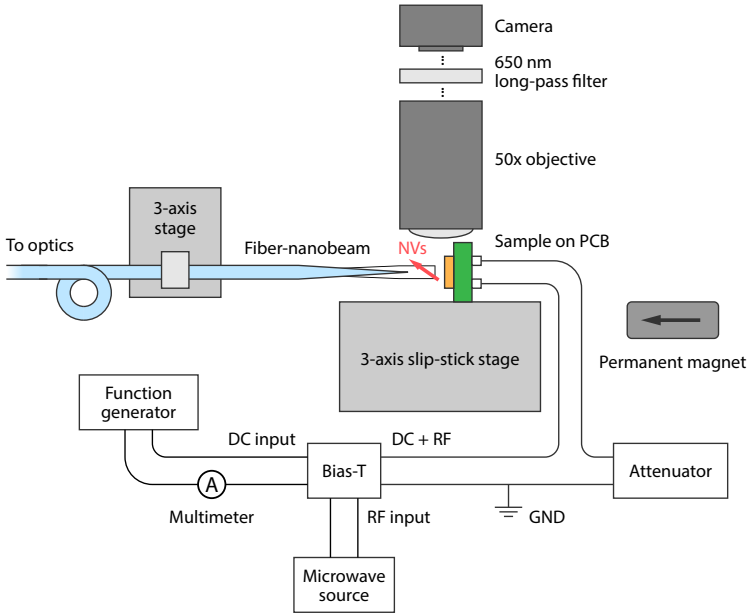
Figure 5.8 - **Schematics of the scanning magnetometry setup using fiber-coupled nanobeams.** It is based on the nanobeam manipulation setup shown in fig. 4.3. The gold-on-silicon sample is wire-bonded to a PCB and mounted vertically underneath the microscope objective. Both DC current and microwave signal are applied to the microstrip through a bias-T. A permanent magnet is mounted next to the positioner and adjusted so that the external field aligns with one of the NV orientations.

We use our fiber-coupled nanobeam sensor to measure the magnetic field generated by a DC electric current in a microstrip on a chip. The setup we use to perform scanning magnetometry using the fiber-coupled diamond nanobeams (fig. 5.8) is based on the nanobeam manipulation setup in fig. 4.3: The 3-axis slip-stick stage is used to position the sample, and the fiber-nanobeam is fixed to the

separate 3-axis stage for independent coarse positioning. The 50× objective provides free-space visual access to monitor the probe-sample distance during the scanning measurements when the sample is mounted vertically underneath the objective.

The sample consists of gold strips patterned on top of a silicon substrate via evaporation (5 nm titanium + 100 nm gold, Temescal FC-2000) and lift-off. The DC current is applied using a function generator (Tektronix AFG1062) and read out by a digital multimeter wired in series with the sample. We apply the RF signal for driving the NV centers through the same strip, using a bias-T (Mini-Circuits ZFBT-6GW-FT+) to combine the RF and DC signal.

We mount the chip vertically with respect to the nanobeam and apply an external magnetic field B_0 along one of the four possible crystallographic orientations of the NV centers to isolate their ESR transition (fig. 5.9(a)). To measure the field generated by the DC current, we first position the beam at about 1 μm above an edge of the strip. While we expected the ESR resonance to shift with respect to its value at B_0 because of the microstrip field, we surprisingly observed that the ESR dip splits (fig. 5.9(c)). By measuring the NV ESR spectrum in a line scan across the strip, we observe the evolution of this split peak in the changing strip field (fig. 5.9(e)). A strongly shifting dip and a weakly shifting dip are clearly visible.

The observed splitting of the ESR response indicates the presence of two sub-ensembles of NV centers in our nanobeam that experience different magnetic fields. Assuming the strongly shifting dip corresponds to the NVs at the nanobeam tip (as these NVs should experience the largest magnetic field from the wire), we can fit the magnetic field extracted from this dip to the calculated wire field at a distance h above the sample. We find an accurate match with the data for $h = 1.8(2)$ μm. From the same fit, we can extract the NV angle θ_z (fig. 5.9(a)), as this angle leads to a spatial asymmetry of the signal. We find $\theta_z = 43(3)°$. The difference from the 35° angle expected from the crystal orientation indicates a small tilt of the fiber-nanobeam with respect to sample surface. We conclude that, despite the presence of a weakly shifting ESR resonance, we can accurately extract the surface magnetic field using the NV ensemble at the tip.

We attribute the weakly shifting resonance to NVs that were spuriously implanted into an unprotected beam sidewall because of a small misalignment during implantation (fig. 5.9(b)). SRIM simulations of 50 keV nitrogen implantation at a $\alpha = 1°$ misalignment angle with respect to the diamond surface yield an average implantation depth of ∼ 10 nm, sufficient to form a low-density, optically addressable NV layer along the 40 μm-long beam sidewall. To check the validity of this assumption, we model the measured ESR spectra $I(f, x)$ by integrating the ESR response of NV centers that are partially located at the end facet and partially distributed homogeneously along the beam sidewall:

$$I(f,x) = \frac{1}{1+\beta}\left(I_0(f, B(x,h)) + \frac{\beta}{L}\int_h^{h+L} I_0(f, B(x,z))\,dz\right). \tag{5.13}$$

Here, $I_0(f, B)$ is the normalized PL intensity of a single NV center, $B(x, z)$ is the magnetic field in the nanobeam, $h = 1.8$ μm denotes the tip-sample distance determined previously, and $L = 40$ μm is the length of the nanobeam. We assume all
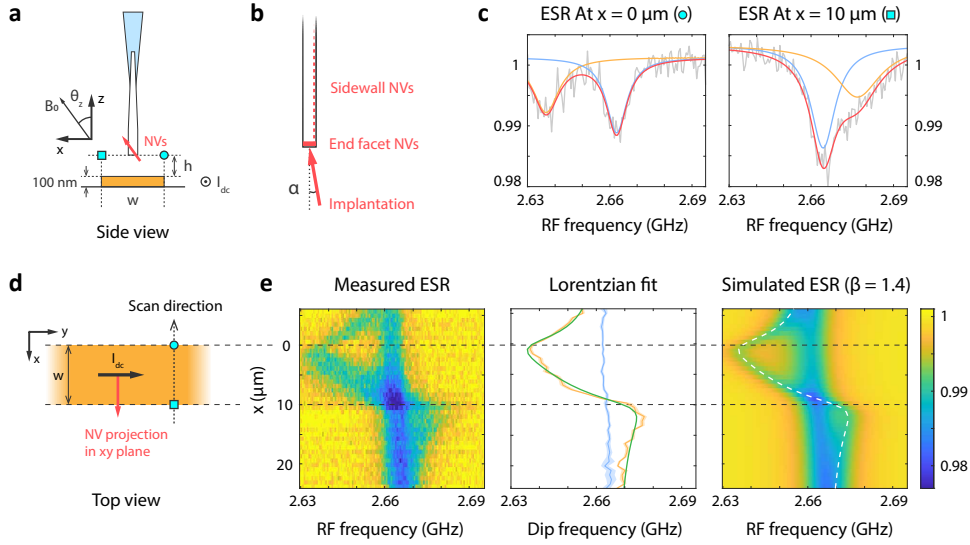
Figure 5.9 - **Characterizing the NV distribution in a tip-NV nanobeam by imaging the magnetic field of a current-carrying wire.** **(a)** Side view of the measurement scheme. The nanobeam is scanned above a 100 nm-thick, 10 μm wide gold strip on a silicon substrate. $I_{dc} = 20$ mA is applied through the gold strip along with the microwave signal used to drive ESR. An external magnetic field $B_0 = 7.31(6)$ mT is applied along one of the four crystallographic NV orientations, at 35° with respect to the beam axis ($\langle 110 \rangle$) and perpendicular to the strip. We use the lower ESR frequency of this NV orientation in subsequent magnetometry measurements. **(b)** Illustration of how a small misalignment α during nitrogen implantation can lead to NVs distributed along the beam sidewall. **(c)** ESR spectrum measured at $x = 0$ μm (left, cyan circle in (a)) and $x = 10$ μm (right, cyan square in (a)). The data (light grey) is fitted with a double Lorentzian (red) to extract the contribution from the end-facet (orange) and sidewall NVs (blue). **(d)** Top view of the measurement scheme. **(e)** *Left*: Normalized ESR spectra measured across the strip (dotted arrow in (d)). *Middle*: ESR frequencies extracted via a double Lorentzian fit. We fit the extracted end-facet ESR frequencies (orange curve) using a model of the wire magnetic field (green). Free parameters are the offset and scaling in x, the lift height h and NV orientation θ_z. The fit yields $h = 1.8(2)$ μm and $\theta_z = 43(3)°$. Right: Calculated ESR line shape across the strip based on eq. (5.13). The ESR frequencies at the end facet (white dashed curve, same as the green curve in the middle panel) are superimposed on the plot for reference.

NV centers have equal contrast and linewidth. We weigh the relative contribution of the sidewall NVs by a factor β, which parametrizes their different number and coupling efficiency to the optical mode in the fiber. This model accurately reproduces the measured split-dip ESR spectra (fig. 5.9(e), right) for $\beta = 1.4$.

Reducing the number of sidewall-implanted NVs would improve the signal-to-background ratio and thereby the magnetometry sensitivity. We anticipate this can be achieved by performing the angled ion implantation after the atomic layer deposition step (section 3.1.6): With a 20 nm layer of alumina uniformly covering the sample, one could set the implantation energy such that the nitrogen ions would be implanted into the diamond under the near-normal incidence at the end facet, but would get trapped in the alumina for the grazing-angle incidence at the beam sidewalls.

5.3.3. Estimating the coupling efficiency for end-facet NVs

Now that we are aware of the existence of sidewall NVs in the nanobeam, we can go back to the optical saturation measurement in section 5.3, and estimate the coupling efficiency of *solely* the end-facet NVs, as these are the ones that are useful for magnetometry measurements.

The fraction of the end-facet NV contribution in the total measured PL can be estimated from the contrast ratio extracted from fig. 5.9(c) left (where the dips are most split):

$$\beta_{\mathrm{E}} = \frac{I_{\mathrm{E}}}{I_{\mathrm{tot}}} = \frac{C_{\mathrm{E}}}{C_{\mathrm{E}} + C_{\mathrm{S}}} = 0.43(7) \tag{5.14}$$

where the subscripts E and S stand for the end-facet and sidewall contribution respectively (Note that β_{E} is different from the sidewall NV contribution β discussed previously). We then scale the 600 nm filtered saturation curve in fig. 5.9(c) with β_{E} to extract the saturation intensity of the end-facet NVs

$$I_{\mathrm{sat,E}} = \beta_{\mathrm{E}} I_{\mathrm{sat,600nm}} = (5.6 \pm 1.1) \times 10^5 \, \mathrm{s}^{-1}, \tag{5.15}$$

from which the total collection efficiency of the end-facet NVs can be estimated as the ratio of the detected saturation intensity and the theoretically expected saturation emission rate:

$$\eta_{\mathrm{E}} = \frac{I_{\mathrm{sat,E}}}{N_{\mathrm{E}} \Gamma}, \tag{5.16}$$

where N_{E} denotes the number of end-facet NVs, and $\Gamma = 1/(13 \, \mathrm{ns})$ [5] is the expected saturation photon emission rate of a single NV. In our measurement setup, η_{E} can be expressed as the product of the fiber-nanobeam coupling efficiency $\eta_{\mathrm{E,f}}$, ND filtering $\eta_{\mathrm{ND}} = 1 \times 10^{-3}$ and the total detection efficiency of the optical path $\eta_{\mathrm{D}} = 0.14(2)$ (including the loss through the optical elements and detection efficiency of the APD).

Here, the major uncertainty in estimating the fiber-nanobeam coupling efficiency $\eta_{\mathrm{E,f}}$ lies in the NV number N_{E}, due to the large uncertainty in the conversion efficiency of the implanted nitrogen ions to NV centers. Taking the data from ref.[18] as a reference and further considering the possible deviation from this dataset caused by the presence of nanostructures, we assume the conversion efficiency to be between 1%~10%. This results in $\eta_{\mathrm{E,f}} = 2\% \sim 26\%$.

References

[1] S. Gröblacher, J. T. Hill, A. H. Safavi-Naeini, J. Chan, and O. Painter. "Highly efficient coupling from an optical fiber to a nanoscale silicon optomechanical cavity". In: *Applied Physics Letters* 103.18 (Oct. 2013). ISSN: 00036951. DOI: 10.1063/1.4826924.

[2] M. J. Burek, C. Meuwly, R. E. Evans, M. K. Bhaskar, A. Sipahigil, S. Meesala, B. MacHielse, D. D. Sukachev, C. T. Nguyen, J. L. Pacheco, E. Bielejec, M. D. Lukin, and M. Lončar. "Fiber-coupled diamond quantum nanophotonic interface". In: *Physical Review Applied* 8.2 (Aug. 2017). ISSN: 23317019. DOI: 10.1103/PhysRevApplied.8.024026.

[3] Element Six. *DNV Series Datasheet*. 2021. URL: https://e6cvd.com/uk/material/single-crystalline/dnv-b14-%203-0mmx3-0mm-0-5mm.html.

[4] A. Dréau, M. Lesik, L. Rondin, P. Spinicelli, O. Arcizet, J. F. Roch, and V. Jacques. "Avoiding power broadening in optically detected magnetic resonance of single NV defects for enhanced dc magnetic field sensitivity". In: *Physical Review B* 84.19 (Nov. 2011), p. 195204. ISSN: 1550235X. DOI: 10.1103/PhysRevB.84.195204.

[5] N. B. Manson, J. P. Harrison, and M. J. Sellars. "Nitrogen-vacancy center in diamond: Model of the electronic structure and associated dynamics". In: *Physical Review B* 74.10 (2006), p. 104303. ISSN: 10980121. DOI: 10.1103/PhysRevB.74.104303.

[6] N. Aslam, G. Waldherr, P. Neumann, F. Jelezko, and J. Wrachtrup. "Photo-induced ionization dynamics of the nitrogen vacancy defect in diamond investigated by single-shot charge state detection". In: *New Journal of Physics* 15 (Jan. 2013). ISSN: 13672630. DOI: 10.1088/1367-2630/15/1/013064.

[7] P. Siyushev, M. Nesladek, E. Bourgeois, M. Gulka, J. Hruby, T. Yamamoto, M. Trupke, T. Teraji, J. Isoya, and F. Jelezko. "Photoelectrical imaging and coherent spin-state readout of single nitrogen-vacancy centers in diamond". In: *Science* 363.6428 (Feb. 2019), pp. 728–731. ISSN: 0036-8075. DOI: 10.1126/science.aav2789.

[8] T. L. Wee, Y. K. Tzeng, C. C. Han, H. C. Chang, W. Fann, J. H. Hsu, K. M. Chen, and E. C. Yu. "Two-photon excited fluorescence of nitrogen-vacancy centers in proton-irradiated type Ib diamond". In: *Journal of Physical Chemistry A* 111.38 (Sept. 2007), pp. 9379–9386. ISSN: 10895639. DOI: 10.1021/jp073938o.

[9] T. Mittiga, S. Hsieh, C. Zu, B. Kobrin, F. Machado, P. Bhattacharyya, N. Z. Rui, A. Jarmola, S. Choi, D. Budker, and N. Y. Yao. "Imaging the local charge environment of nitrogen-vacancy centers in diamond". In: *Physical Review Letters* 121.24 (Dec. 2018). ISSN: 10797114. DOI: 10.1103/PhysRevLett.121.246402.

[10] L. Robledo, L. Childress, H. Bernien, B. Hensen, P. F. Alkemade, and R. Hanson. "High-fidelity projective read-out of a solid-state spin quantum register". In: *Nature* 477.7366 (Sept. 2011), pp. 574–578. ISSN: 00280836. DOI: 10.1038/nature10401.

[11] A. Beveratos, R. Brouri, T. Gacoin, J.-P. Poizat, and P. Grangier. "Nonclassical radiation from diamond nanocrystals". In: *Physical Review A* 64.6 (Nov. 2001), p. 061802. ISSN: 1050-2947. DOI: 10.1103/PhysRevA.64.061802.

[12] S. Mi, A. Toros, T. Graziosi, and N. Quack. "Non-contact polishing of single crystal diamond by ion beam etching". In: *Diamond and Related Materials* 92 (Feb. 2019), pp. 248–252. ISSN: 09259635. DOI: 10.1016/j.diamond.2019.01.007.

[13] Y. Li, F. A. Gerritsma, S. Kurdi, N. Codreanu, S. Gröblacher, R. Hanson, R. Norte, and T. van der Sar. "A fiber-coupled scanning magnetometer with nitrogen-vacancy spins in a diamond nanobeam". In: *ACS Photonics* 10.6 (June 2023), pp. 1859–1865. ISSN: 2330-4022. DOI: 10.1021/acsphotonics.3c00259.

[14] A. Savvin, A. Dormidonov, E. Smetanina, V. Mitrokhin, E. Lipatov, D. Genin, S. Potanin, A. Yelisseyev, and V. Vins. "NV– diamond laser". In: *Nature Communications* 12.1 (Dec. 2021), p. 7118. ISSN: 2041-1723. DOI: 10.1038/s41467-021-27470-7.

[15] I. Cardoso Barbosa, J. Gutsche, and A. Widera. "Impact of charge conversion on NV-center relaxometry". In: *Physical Review B* 108.7 (Aug. 2023), p. 075411. ISSN: 2469-9950. DOI: 10.1103/PhysRevB.108.075411.

[16] S. T. Alsid, J. F. Barry, L. M. Pham, J. M. Schloss, M. F. O'Keeffe, P. Cappellaro, and D. A. Braje. "Photoluminescence decomposition analysis: A technique to characterize N-V creation in diamond". In: *Physical Review Applied* 12.4 (Oct. 2019), p. 044003. ISSN: 2331-7019. DOI: 10.1103/PhysRevApplied.12.044003.

[17] W. Zheng, K. Bian, X. Chen, Y. Shen, S. Zhang, R. Stöhr, A. Denisenko, J. Wrachtrup, S. Yang, and Y. Jiang. "Coherence enhancement of solid-state qubits by local manipulation of the electron spin bath". In: *Nature Physics* 18.11 (Nov. 2022), pp. 1317–1323. ISSN: 1745-2473. DOI: 10.1038/s41567-022-01719-4.

[18] S. Pezzagna, B. Naydenov, F. Jelezko, J. Wrachtrup, and J. Meijer. "Creation efficiency of nitrogen-vacancy centres in diamond". In: *New Journal of Physics* 12 (June 2010). ISSN: 13672630. DOI: 10.1088/1367-2630/12/6/065017.

6

Scanning-probe magnetic imaging with fiber-coupled diamond nanobeams

🎵 ·|ı|ı|ıı·|||·|ı···

We walk backwards
say nothing
run for visions
at all.

Hailing Drums · Re-TROS

Abstract

Based on the through-fiber readout of NV centers in the diamond nanobeams, in this chapter we demonstrate magnetic imaging using our fiber-coupled diamond nanobeam probes. Two different scanning-probe configurations are used for the two types of nanobeams: In section 6.1, we discuss the 1D imaging of spin waves using the homogeneous-NV nanobeams, and in section 6.2 we use the tip-NV nanobeams to image the field profile of a current-carrying wire in 2D. For the latter, we also demonstrate lift-height control and surface imaging through probe-surface contact, enabling scanning-probe magnetometry without free-space optical access.

Introduction

Combining scanning-NV magnetometry with an all-fiber optical interface could open up new avenues for magnetic imaging in hard-to-reach environments, such as low-temperature [1] or biological systems [2, 3]. The through-fiber readout of NV spins characterized in the previous chapter has provided the basis for such measurements. In this chapter, we proceed to discuss the integration of our probes into scanning-probe configurations, and the realization of magnetic imaging. For the two generations of nanobeam probes, different scanning configurations are applied, and the details will be discussed in section 6.1 and section 6.2.

6.1. 1D imaging of spin waves in yttrium-iron-garnet (YIG)

For the first generation homogeneous-NV nanobeams, the through-fiber readout signal will be a (weighted) sum over all the NVs within the nanobeam. Therefore it is not possible to perform 2D magnetic imaging with a resolution below the the beam length. Nevertheless, we can still use these devices to realize 1D imaging with sub-micron spatial resolution by scanning the beam perpendicular to its orientation (as will be illustrated in fig. 6.1), and study magnetic field profiles that are also homogeneous along the beam. One such example is the stray field of *spin waves*: the wave-like excitations of spins in a magnetic material [4].

   In this section, we use the homogeneous-NV nanobeams to demonstrate the 1D imaging of spin waves in a ∼ 250 nm-thick film of yttrium iron garnet (YIG) [5]. In our specific configuration, the spin waves have a planar wavefront: This allows us to align our nanobeam parallel to these wavefronts and scan the nanobeam along the wave vector orientation, thereby spatially mapping out the wave profile. The details of this process are discussed below.

6.1.1. Spin wave dynamics

NV imaging of spin waves relies on resonantly driving the NV-ESR transition using the stray magnetic field generated by the spin waves. To better understand the latter and formulate the theoretical expectation of our measurement, here we first give a brief explanation on the modeling of spin dynamics in YIG, based on the discussion in ref. [6].

   We consider our YIG layer as an infinite film parallel to the xy plane, infinite in x and y with a thickness t in z direction, and the equilibrium magnetization points in y. We can calculate the dispersion of the spin waves using the Landau-Lifshitz-Gilbert (LLG) equation which governs the dynamics of magnetization

$$\dot{\mathbf{m}} = -\gamma \mathbf{m} \times (\mathbf{B}_{\mathrm{eff}} + \mathbf{B}_{\mathrm{AC}}) - \alpha \dot{\mathbf{m}} \times \mathbf{m} \tag{6.1}$$

in which $\mathbf{m}(\mathbf{r})$ is the unit vector in the direction of the magnetization $\mathbf{M}(\mathbf{r}) = M_s \mathbf{m}(\mathbf{r})$ (with M_s being the saturation magnetization), $\mathbf{B}_{\mathrm{AC}}$ is the AC driving field, γ is the gyromagnetic ratio and α is the Gilbert damping. The effective field $\mathbf{B}_{\mathrm{eff}}$ takes into account the static external magnetic field $\mathbf{B}_0$, the demagnetizing field $\mathbf{B}_d$ and the exchange interaction.

Since spin waves are propagating waves of spin precession around the magnetization axis in equilibrium, we are interested in the dynamics of the *transverse magnetization*

$$\mathbf{m}_\perp = \chi \mathbf{B}_{AC,\perp} \tag{6.2}$$

where $\mathbf{m}_\perp$ and $\mathbf{B}_{AC,\perp}$ are the components of the magnetization vector and AC drive field transverse to the equilibrium magnetization orientation, and χ is the *transverse susceptibility*. Following the formalism by Rustagi et al. [6], we can find χ by solving the LLG equation in k-space, and determine the spin wave dispersion $\omega_{sw}(\mathbf{k})$ by finding the singularity of χ, which eventually gives us

$$\omega_{sw}(\mathbf{k}) = \sqrt{\omega_2 \omega_3 - \omega_1^2}, \tag{6.3}$$

where $\mathbf{k} = (k_x, k_y)$ is the in-plane wave vector. Parameters $\omega_1 \sim \omega_3$ are in general functions of the equilibrium magnetization orientation, the direction of $\mathbf{k}$, effective static field $\mathbf{B}_{eff}$ and the film thickness t [6].

In our measurements, we apply the external magnetic field $\mathbf{B}_0 = B_0 \hat{\mathbf{y}}$ along the y direction, and excite the spin waves in the Damon-Eshbach (DE) regime where the wave vector $\mathbf{k} = k\hat{\mathbf{x}}$ is perpendicular to $\mathbf{B}_0$. Under these conditions, $\omega_1 \sim \omega_3$ are reduced to

$$\omega_1 = 0; \tag{6.4}$$

$$\omega_2 = \omega_B + \omega_D k^2 + \omega_M (1 - f); \tag{6.5}$$

$$\omega_3 = \omega_B + \omega_D k^2 + \omega_M f. \tag{6.6}$$

where we defined $\omega_B = \gamma B_0$, $\omega_D = \gamma D / M_s$ with D being the spin stiffness that characterizes the exchange interaction between spins, $\omega_M = \gamma \mu_0 M_s$, $f = 1 - (1 - e^{-kt})/kt$ with t being the film thickness.

6.1.2. Imaging spin waves with NV centers

The precession of magnetization around the equilibrium magnetization axis y generates a stray magnetic field that rotates in the xz plane at the spin wave frequency ω_{sw}. This AC magnetic field can be used to drive the ESR transition of NV centers in proximity of the YIG film when ω_{sw} matches the NV-ESR frequency under the static external bias field $\mathbf{B}_0$. As demonstrated in refs. [7, 8], the wavefronts of spin waves can be imaged through the *contrast* of the spin-wave-driven NV-ESR signal. This can be understood as follows (following the discussion in ref. [7]):

In our measurement (fig. 6.1(a)), we use a stripline parallel to the y direction to excite spin waves traveling in $+x$ direction (so $k > 0$) with a planar wavefront. Close to the stripline, we ignore the damping of spin waves, and write the stray field of the spin wave as [7]

$$\mathbf{B}_{sw}(x, t) = -\text{Re}\left(B_{sw,0} e^{i(kx - \omega_{sw}t)} (\hat{\mathbf{x}} + i\hat{\mathbf{z}}) \right) \equiv \text{Re}\left((B_x(x)\hat{\mathbf{x}} + B_z(x)\hat{\mathbf{z}}) e^{-i\omega_{sw}t} \right), \tag{6.7}$$

where the amplitude $B_{sw,0}$ depends on the saturation magnetization, propagation direction of the spin wave (i.e. sign(k)), ellipticity of the spin wave and the

distance away from the YIG film. When ω_{sw} is resonant with the NV-ESR transition, such a stray field drives the $|m_S = 0\rangle \rightarrow |m_s = \pm 1\rangle$ transition with a Rabi frequency determined by the amplitude and handedness of the field component transverse to the NV axis:

$$\Omega_R^{\pm}(x) = \frac{\gamma}{\sqrt{2}} |B_{x'}(x) \mp i B_{y'}(x)|. \tag{6.8}$$

Here we defined the local coordinates (x', y', z') of the NV center such that the NV orientation aligns with z'. For NV centers lying in the yz plane as in our measurements, we have $\hat{\mathbf{z}}' = \hat{\mathbf{n}}_{NV} = \hat{\mathbf{y}}\cos\phi + \hat{\mathbf{z}}\sin\phi$, leading to the coordinate transformation of $\mathbf{B}_{sw}$:

$$\begin{aligned} B_{x'}(x) &= B_x(x), \\ B_{y'}(x) &= B_y(x)\sin\phi - B_z(x)\cos\phi. \end{aligned} \tag{6.9}$$

Substituting back into eq. (6.8) yields

$$\begin{aligned} \Omega_R^-(x) &= \sqrt{2}\gamma B_{sw,0} \cos^2\frac{\phi}{2}, \\ \Omega_R^+(x) &= \sqrt{2}\gamma B_{sw,0} \sin^2\frac{\phi}{2}. \end{aligned} \tag{6.10}$$

The above results have two implications: As will be discussed in section 6.1.3, in our measurements we have $\phi = 35°$, leading to $\Omega_R^- \approx 10\Omega_R^+$ i.e. the spin wave drives predominantly the $|m_S = 0\rangle \rightarrow |m_s = -1\rangle$ transition. We will therefore focus on this transition for the rest of this section. Also, $\Omega_R^{\pm}$ are *spatially homogeneous*, and therefore do not contain any information about the spatial profile of the spin waves.

In order to image the spatial variation of $\mathbf{B}_{sw}$, we apply a spatially homogeneous reference field with the same frequency and phase $\mathbf{B}_{ref}(t)$ through a bonding wire located above the sample [7, 8]. In the NV coordinates, the reference field is written as

$$\mathbf{B}_{ref}(t) = \text{Re}\left((B_{ref,x'}\hat{\mathbf{x}}' + B_{ref,y'}\hat{\mathbf{y}}' + B_{ref,z'}\hat{\mathbf{z}}') e^{-i\omega_{sw}t} \right). \tag{6.11}$$

Under the superposition $\mathbf{B}_{sw}(x,t) + \mathbf{B}_{ref}(t)$, the Rabi frequency becomes

$$\Omega_R^-(x) = \frac{\gamma}{\sqrt{2}} \left| 2B_{sw,0}\cos^2\frac{\phi}{2} \cdot e^{ikx} + (B_{ref,x'} + iB_{ref,y'}) \right|, \tag{6.12}$$

which is periodic in x with the same period $2\pi/k$ as the spin-wave wavelength.

This allows the imaging of $\mathbf{B}_{sw}$ because the Rabi frequency directly determines the NV-ESR contrast C^-, through the relation[9]

$$C^-(x) \propto \frac{(\Omega_R^-(x))^2}{(\Omega_R^-(x))^2 + \Delta} \tag{6.13}$$

where the parameter Δ is determined by the optical excitation power of NV centers, therefore remains constant in our measurement scheme. As a result, the measured ESR contrast along the spin wave propagation direction also has the same periodicity as the spin wave itself, thereby enabling the imaging of spin wave through mapping out the ESR contrast.

6.1.3. Visualizing the planar wavefront with ensemble NVs in the diamond nanobeam
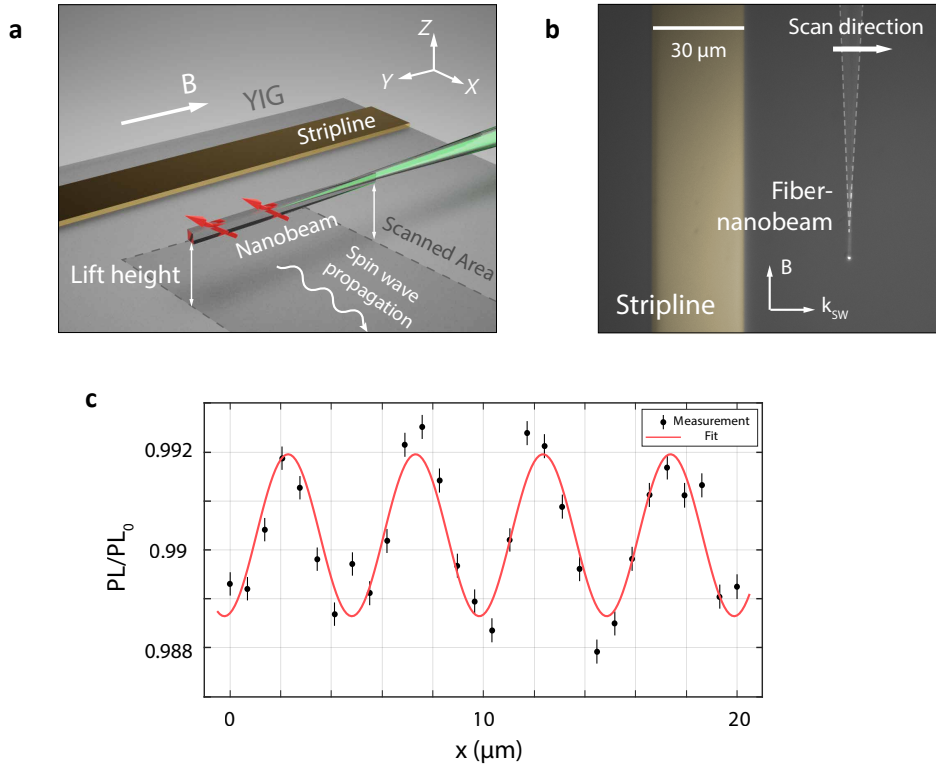
Figure 6.1 - **Proof-of-principle scanning NV magnetometry with a fiber-coupled diamond nanobeam.** **(a)** Experimental geometry: A fiber-coupled NV nanobeam is used to image spin waves in a 250-nm-thick film of yttrium iron garnet. The YIG-nanobeam distance is ~5 μm. The beam is scanned perpendicularly to the beam axis. The spin waves are excited by a microwave current in a gold stripline (3 mm × 30 μm). An auxiliary wire drawn across the chip (not shown) provides a reference field that interferes with the spin-wave stray field, creating a standing-wave pattern in the microwave magnetic-field amplitude [7]. A static magnetic field B is applied along the beam direction. **(b)** Microscope image of the experimental geometry. **(c)** Scanning-nanobeam imaging of a spin wave. The NV ESR contrast PL/PL_0 is measured by switching on and off the microwave drive at the NV ESR frequency. The error bars are estimated from assuming shot noise of the NV photoluminescence during the measurement time. A sinusoidal fit (red) gives the measured wavelength $\lambda = 5.0(1)\,\mu m$.

To implement the above discussed approach experimentally, we excite the spin wave by sending a microwave current through a gold stripline on the YIG (fig. 6.1(a)) under a static external magnetic field $B = 22\,\text{mT}$. As explained in the previous section, the spin wave generates a microwave magnetic stray field that drives the NV spins when its frequency matches the NV ESR frequency, and we apply an additional, spatially homogeneous reference field of the same microwave frequency using a wire above the chip to create the spatial standing-wave pattern that we can image via the NV ESR contrast. We scan the beam parallel to the sample surface and perpendicularly to the beam axis (fig. 6.1(a)(b)), and measure the NV ESR contrast by switching on and off the microwave drive at the ESR frequency $f = 2.439\,\text{GHz}$.

Figure 6.1(c) images the spin-wavefront in 1D with a resolution limited by the beam width and beam-sample distance. For each data point, the photoluminescence rates PL and PL_0 are measured intermittently, by switching the microwave frequency between f and f_0 at a fixed interval $\delta T = 0.01\,\text{s}$ for 4000 switching cycles, yielding a total measurement time of $T = 40\,\text{s}$ at each frequency. Because of the rapid switching, $1/f$ noise is suppressed and we expect photon shot noise to dominate the uncertainty. With the shot noise given by $\Delta(\text{PL}) = \sqrt{\text{PL}\cdot T}$ (same for PL_0), the error bars for the ratio of the photoluminescence rates plotted in fig. 6.1(c) are calculated using

$$\Delta\left(\frac{\text{PL}}{\text{PL}_0}\right) = \sqrt{\left(\frac{\Delta(\text{PL})}{\text{PL}_0}\right)^2 + \left(\frac{\text{PL}\Delta(\text{PL}_0)}{\text{PL}_0^2}\right)^2}. \tag{6.14}$$

From a simple sinusoidal fit, we observed a wavelength of $\lambda = 5.0(1)\,\mu\text{m}$. This agrees reasonably well with the 6μm expected from the spin-wave dispersion (eq. (6.3)), given the uncertainty in the angle of the applied magnetic field.

6.2. 2D imaging of the magnetic field of a current carrying strip

In section 5.3.2, we already showed the scanning measurement of the magnetic field across a current-carrying wire using the tip-NV nanobeams. Ultimately, these devices are developed for 2D magnetic imaging with sub-micron spatial resolution. Therefore in this section, we extend from the same scanning configuration (figs. 5.8 and 5.9) and discuss the experimental procedure of realizing 2D imaging using the tip-NV nanobeams.

6.2.1. Surface imaging and lift-height control using reflection at probe-surface contact

One important challenge towards 2D magnetometry is the control over the probe-sample distance: With the NV ensemble being confined within the sub-micron scale beam tip, the spatial resolution of the nanobeam probes also holds potential of reaching sub-micron scale. To fully exploit such potential, a mechanism for controlling the probe-sample distance becomes necessary, so that the NV ensemble

can be in sub-micron scale proximity to the sample. Besides, it is also crucial to maintain a fixed tip-sample distance in the presence of thermal drifts and sample tilts. As our setup does not have atomic force microscope feedback as in the scanning cantilever configuration [10], an alternative method needs to be developed. Another practical necessity specific to our fiber-based scanning measurements is the ability to locate and navigate to the region of interest in the absence of free-space imaging of the sample surface.

Here, we address both challenges by monitoring the photoluminescence at probe-surface contact. Specifically, we bring the tip in contact with the sample, and detect the point of contact through the increase of photoluminescence collection due to reflection over the sample surface. We find that this increase is highly
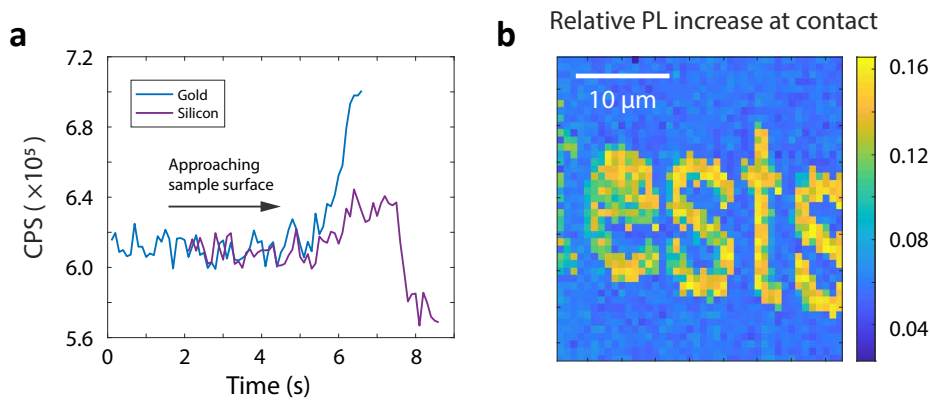
Figure 6.2 - **Surface imaging through photoluminescence at probe-surface contact.**
(a) Examples of recorded photoluminescence traces as the fiber-coupled nanobeam makes approach towards a silicon surface and a gold surface. The arrow indicates the point of contact, marked by an increase in measured counts. The decrease in the PL trace of silicon after contact results from the decreased coupling efficiency due to the elastic deformation of the fiber-nanobeam assembly. When the deformation is restored upon retracting the probe, the PL counts will also be restored. For clarity, the two traces have been shifted horizontally so the contact points align. **(b)** Relative PL increase at probe-surface contact mapped out on a gold-on-silicon sample surface. The letters are patterned in a 40 nm layer of gold on top of a silicon chip. At each pixel, a PL trace as in (a) is recorded as the nanobeam approaches sample surface. The relative increase of PL at contact is calculated as the difference between averaged CPS before and after contact, normalized by CPS before contact. The tilt in the image results from both drifting and a slight mismatch between the forward and backward step sizes of the sample stage.

sensitive to the local sample reflectivity (fig. 6.2(a)), enabling through-fiber imaging of the sample and thus precluding the need for free-space optics. One example of the surface image obtained with this method is shown in fig. 6.2(b).

Furthermore, based on the through-fiber detection of contact, we achieve lift-height control by retracting the tip by a fixed amount after contact is detected. Crucially, our sensor remains intact under the repetitive tip-sample contacts, highlighting the robust nature of the glued nanobeam-fiber assembly.

6.2.2. Visualizing magnetic field distribution in 2D

With height control and navigation in place, we demonstrate 2D imaging through characterizing the magnetic field generated by a direct current that is sent through an omega-shaped, 2 μm-wide gold strip (fig. 6.3a). We image the magnetic field of the strip by measuring the ESR frequency of the end-facet NVs. To do so, we retract the tip by ~ 1 μm after making tip-sample contact, measure the ESR spectrum and extract the end-facet NV ESR frequency using a double Lorentzian fit as described in fig. 5.9.
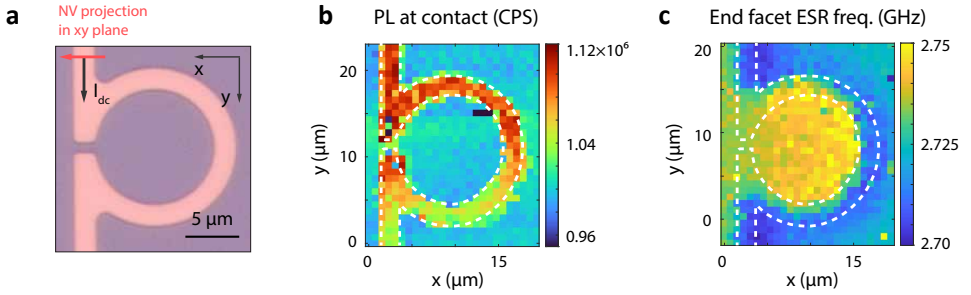
Figure 6.3 - **Magnetic imaging with electron spins in a fiber-coupled diamond nanobeam.** **(a)** Optical microscope image of the omega-shaped gold strip. The width of the strip is 2 μm. **(b)** Through-fiber microscopy of the omega-shaped strip. At each pixel, the nanobeam is moved towards the sample. The increased photoluminescence upon contact is shown in the image. **(c)** 2D map of the end-facet ESR frequency, with $B_0 = 5.0(2)$ mT, $I_{dc} = 10$ mA and $h \sim 1$ μm. At each pixel, the end-facet and sidewall ESR frequencies are extracted via a double Lorentzian fit with the sidewall ESR frequency fixed at 2.729 GHz. White dashed lines indicate the boundary of the gold strip inferred from (b). Both (b) and (c) are post-corrected for drift based on the known shape of the strip (see SI for the original drift-distorted image).

Due to limited signal to noise, we take the approximation to fix the frequency of sidewall NV dips to $f_0 = 2.729$ GHz, corresponding to the ESR frequency under the static bias field $B_0 = 5.0$ mT only. The extracted end-facet ESR frequencies encode the projection of the total magnetic field onto the NV axis. As plotted in fig. 6.3(c),

the expected near-uniform magnetic field within the ring and the magnetic field in the opposite direction outside the ring are clearly observed.

We note that fig. 6.3(b) and (c) have been corrected for spatial drifting during the scan. To illustrate this, we plot in fig. 6.4 the spatial map of fit parameters obtained from the double Lorentzian fit *before* drift correction. Distortion in the x axis is clearly visible in the plots, as a result of the drift of probe and sample position during the ∼ 12-hour scan, executed line by line in x. This distortion is corrected by manually aligning the left edge of the strip in the contact PL map, and applying the same transformation to the ESR frequency map.

The limiting factor of the spatial resolution in this measurement is two-fold: First, the NV ensemble implanted homogeneously into the $(0.5 \times 0.5\,\mu m^2)$ beam end-facet limits the spatial resolution. Low-nanoscale imaging therefore requires moving to

6
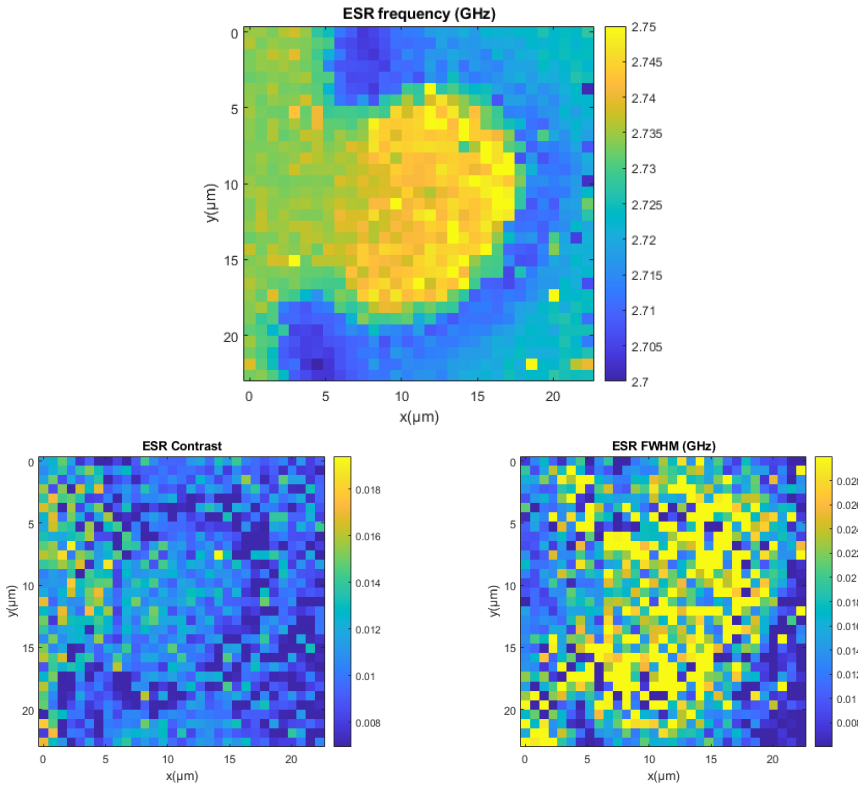
Figure 6.4 - **Spatial map of the double Lorentzian fitting parameters before drift correction.** At each pixel, an ESR spectrum is taken and fitted to a double Lorentzian as described in section 5.3.2, with the sidewall ESR frequency fixed at 2.729 GHz. The fitted ESR frequency (top), contrast (bottom left), full width half maximum (bottom right) of the end-facet NV dip is plotted.

single NV$^-$ regime. With the previous characterization of the negligible background contribution (fig. 5.6), we already showed that single NV readout is possible under 600 nm + 700 nm long-pass filtering. Second, the reflection-based height control we used in this work does not allow feedback control of the tip-sample distance below $h \sim 1\,\mu$m. To this end, we are working towards integrating our fiber probe in a tuning-fork based atomic force microscope (AFM) system [11], based on gluing the tip of the fiber to the tuning fork [12] or on keeping them in mechanical contact with a dedicated scan head design [1, 13].

Acknowledgment

6

References

[1] A. Uri, Y. Kim, K. Bagani, C. K. Lewandowski, S. Grover, N. Auerbach, E. O. Lachman, Y. Myasoedov, T. Taniguchi, K. Watanabe, J. Smet, and E. Zeldov. "Nanoscale imaging of equilibrium quantum Hall edge currents and of the magnetic monopole response in graphene". In: *Nature Physics* 16.2 (Feb. 2020), pp. 164–170. ISSN: 17452481. DOI: 10.1038/s41567-019-0713-3.

[2] D. Le Sage, K. Arai, D. R. Glenn, S. J. Devience, L. M. Pham, L. Rahn-Lee, M. D. Lukin, A. Yacoby, A. Komeili, and R. L. Walsworth. "Optical magnetic imaging of living cells". In: *Nature* 496.7446 (Apr. 2013), pp. 486–489. ISSN: 00280836. DOI: 10.1038/nature12072.

[3] S. Steinert, F. Ziem, L. T. Hall, A. Zappe, M. Schweikert, N. Götz, A. Aird, G. Balasubramanian, L. Hollenberg, and J. Wrachtrup. "Magnetic spin imaging under ambient conditions with sub-cellular resolution". In: *Nature Communications* 4 (2013). ISSN: 20411723. DOI: 10.1038/ncomms2588.

[4] A. V. Chumak, V. I. Vasyuchka, A. A. Serga, and B. Hillebrands. "Magnon spintronics". In: *Nature Physics* 11.6 (June 2015), pp. 453–461. ISSN: 17452481. DOI: 10.1038/nphys3347.

[5] A. A. Serga, A. V. Chumak, and B. Hillebrands. "YIG magnonics". In: *Journal of Physics D: Applied Physics* 43.26 (2010). ISSN: 00223727. DOI: 10.1088/0022-3727/43/26/264002.

[6] A. Rustagi, I. Bertelli, T. van der Sar, and P. Upadhyaya. "Sensing chiral magnetic noise via quantum impurity relaxometry". In: *Physical Review B* 102.22 (Dec. 2020), p. 220403. ISSN: 24699969. DOI: 10.1103/PhysRevB.102.220403.

[7] I. Bertelli, J. J. Carmiggelt, T. Yu, B. G. Simon, C. C. Pothoven, G. E. W. Bauer, Y. M. Blanter, J. Aarts, and T. Van Der Sar. "Magnetic resonance imaging of spin-wave transport and interference in a magnetic insulator". In: *Science Advances* 6 (2020), pp. 3556–3567. DOI: https://doi.org/10.1126/sciadv.abd3556.

[8] B. G. Simon, S. Kurdi, H. La, I. Bertelli, J. J. Carmiggelt, M. Ruf, N. De Jong, H. Van Den Berg, A. J. Katan, and T. Van Der Sar. "Directional excitation of a high-density magnon gas using coherently driven spin waves". In: *Nano Letters* 21.19 (Oct. 2021), pp. 8213–8219. ISSN: 15306992. DOI: 10.1021/acs.nanolett.1c02654.

[9] A. Dréau, M. Lesik, L. Rondin, P. Spinicelli, O. Arcizet, J. F. Roch, and V. Jacques. "Avoiding power broadening in optically detected magnetic resonance of single NV defects for enhanced dc magnetic field sensitivity". In: *Physical Review B* 84.19 (Nov. 2011), p. 195204. ISSN: 1550235X. DOI: 10.1103/PhysRevB.84.195204.

[10]   P. Maletinsky, S. Hong, M. S. Grinolds, B. Hausmann, M. D. Lukin,
       R. L. Walsworth, M. Loncar, and A. Yacoby. "A robust scanning diamond
       sensor for nanoscale imaging with single nitrogen-vacancy centres". In:
       Nature Nanotechnology 7.5 (2012), pp. 320–324. ISSN: 17483395. DOI:
       10.1038/nnano.2012.50.

[11]   V. T. Tung, S. A. Chizhik, V. V. Chikunov, and T. X. Hoai. "Tapping and
       shear-mode atomic force microscopy using a quartz tuning fork with high
       quality factor". In: *Twelfth International Workshop on Nanodesign Technology
       and Computer Simulations*. Vol. 7377. SPIE, July 2008, p. 73770L. ISBN:
       9780819476531. DOI: 10.1117/12.836902.

[12]   F. Gao, X. Li, J. Wang, and Y. Fu. "Dynamic behavior of tuning fork shear-force
       structures in a SNOM system". In: *Ultramicroscopy* 142 (2014), pp. 10–23. ISSN:
       18792723. DOI: 10.1016/j.ultramic.2014.03.011.

[13]   C. L. Tschirhart, M. Serlin, H. Polshyn, A. Shragai, Z. Xia, J. Zhu, Y. Zhang,
       K. Watanabe, T. Taniguchi, M. E. Huber, and A. F. Young. "Imaging orbital
       ferromagnetism in a moiré Chern insulator". In: *Science* 372.6548 (June 2021),
       pp. 1323–1327. ISSN: 10959203. DOI: 10.1126/science.abd3190.

6

7

Conclusion and outlook

没有答案，
There is no answer,

没有硝烟弥漫。
nor battle smoke filling the air.

许钧《29》
29 · Xu Jun

7.1. Conclusion

To conclude, in this thesis we demonstrated the fabrication, assembly, characterization and proof-of-principle application of scanning-probe NV magnetometers with fiber-coupled diamond nanobeams.

Specifically, we showed that we can fabricate diamond nanobeams using reactive ion etching of diamond. Combined with angled ion implantation, we are able to deterministically create ensemble NV centers at the end facet of the nanobeams. After the fabrication, we demonstrated two approaches of coupling the diamond nanobeams to tapered fibers, forming a fiber-based scannning-probe magnetometer. We showed that we can achieve through-fiber readout of NV centers inside the assembled probes, and characterized the readout efficiency of different fiber-nanobeam devices. Finally, we demonstrated proof-of-principle magnetic imaging using our probes, through the example of 1D spin wave imaging and 2D imaging of magnetic field generated by a current-carrying strip.

7.2. Outlook

As mentioned in the beginning of this thesis, our ultimate goal of developing the fiber-coupled diamond nanobeam magnetometers is realizing low-temperature, nanoscale scanning-probe magnetometry. From what we have achieved so far, there are still multiple challenges that remain to be tackled in the future. In this section, we will discuss the major foreseeable challenges towards low temperature and nanoscale measurements, and propose possible ways to tackle them based on our acquired knowledge.

The first three aspects that will be discussed are intended to bring the spatial resolution down to nanoscale, in order to facilitate mainly the study of nanoscale magnetism in condensed matter: We will discuss the possibilities of reading out a single NV center through the fiber, controlling the probe-sample distance with nanometer precision, and reducing the surface roughness on the beam end-facet so that the NV can be placed closer to surface. Besides, we will also discuss the magnetic sensing capabilities of tin-vacancy (SnV) centers in diamond, which offer better compatibility with low-temperature operation compared to NV centers.

7.2.1. Towards single-NV readout

Using a single NV center as the sensor ensures that the spatial resolution is not limited by the sensing volume. We discuss the possibilities of single-NV magnetometry with diamond nanobeams from the following two aspects:

Creating single NV centers within the nanobeams:

Our current angled ion implantation protocol should already allow the creation of single NV centers at the end of nanobeams. By lowering the implantation dose, an average of one single NV center per nanobeam end-facet area can be realized with a yield limited by statistical deviation. Because of the finite yield, it will be necessary to pre-select devices containing single NV with ideal brightness and contrast, either

via free-space photoluminescence characterization explained in section 3.2.3 or through-fiber readout before breaking and gluing the nanobeams.

Another possible way to deterministically create nanobeams with single NV centers at the tips is to locate pre-implanted single NVs with a scanning confocal microscope as in fig. 3.8, and pattern the nanobeams around these locations [1]. At the cost of an extra characterization step, this approach in principle allows placing the NV centers at ideal locations within the nanobeams where collection efficiency is maximized. The challenge here is in turn the precision of NV localization and nanofabrication: In order for the NV center to be within nanometer-scale proximity to the beam end-facet, the precision of NV localization will also need to reach nanometer-scale, which is non-trivial for an optical method. Also, the uncertainty in the position of e-beam patterning could also limit the eventual precision of NV placement.

Reading out single NV centers from the nanobeams:

Reading out single NV centers through the fiber interface, on the other hand, should also be already possible with our current setup. According to the data analysis in section 5.3.1, when filtered at 700 nm, the contribution of background PL is negligible. Therefore in principle, there should be nothing that fundamentally hinders the readout of a single NV center from a nanobeam. From the PL counts in fig. 5.6(a), we can actually estimate (with a large uncertainty) that under our current collection efficiency, the PL count for a single NV in our setup is on the order of $10^2 \, \text{s}^{-1} \, \mu\text{W}^{-1}$, assuming the number of NVs in the tip-NV nanobeams is on the order of 10^3. If the collection efficiency (both at the fiber-nanobeam interface and in the optical path) can be further improved, a single-NV count rate of $\sim 10^4 \, \text{s}^{-1}$ can be achieved with excitation power less than 100 μW, sufficient for ESR measurements considering the potentially higher contrast for single NVs.

Nevertheless, filtering at 700 nm is after all a compromising solution, removing the background at the cost of sacrificing also more than half of the actual NV signal. Therefore reducing the background fluorescence remains an important upcoming challenge in order to maximize the chance of realizing single-NV readout and improving the signal-to-noise ratio. It will be even more crucial when exploring the sensing capabilities of tin-vacancy (SnV) centers (section 7.2.4), since the wavelength of their photoluminescence is also below 700 nm.

And as the background fluorescence comes from mainly the glue and the fiber, the challenge to reduce it also needs to be tackled from both sides. The fiber autofluorescence can possibly be reduced by separating the excitation and detection port by splicing the tapered fiber to a 2×2 fiber coupler, or using a hollow-core photonic crystal fibers with one end spliced to a short section of tapered normal fiber as demonstrated in ref.[2]. For the glue autofluorescence, possibilities include replacing the optical glue by a low-autofluorescence photoresist [3, 4], or exploring further down the glue-free coupling path we briefly touched upon in section 4.5 with FIB methods.

7.2.2. Height feedback with tuning-fork AFM

In the single-NV regime, the spatial resolution of the scanning-probe measurements will be limited by the probe-sample distance. While in section 6.2.1 we showed that the probe-sample distance can be controlled by optically detecting the probe-sample contact and retracting the stage, the precision of this method is limited by the optical readout noise and is hard to reach further down to sub-micron scale without increasing the integration time. Also, having to make contact with the sample at every pixel can also cause damage to specific types of samples such as 2D materials. It is therefore necessary to implement a different mechanism for controlling the lift height of our nanobeam probe in order to realize nanoscale imaging.

As has been widely applied in scanning-probe NV magnetometry with diamond cantilevers [5], this is possible by incorporating the scanning probe into a tuning-fork atomic force microscope (AFM) structure. By fixing the probe to the prong of a tuning fork, the van der Waals force between the probe tip and the sample surface when they are in close proximity will modify the resonant frequency of the tuning fork, allowing the feedback control of the probe-sample distance through tracking the resonant frequency.
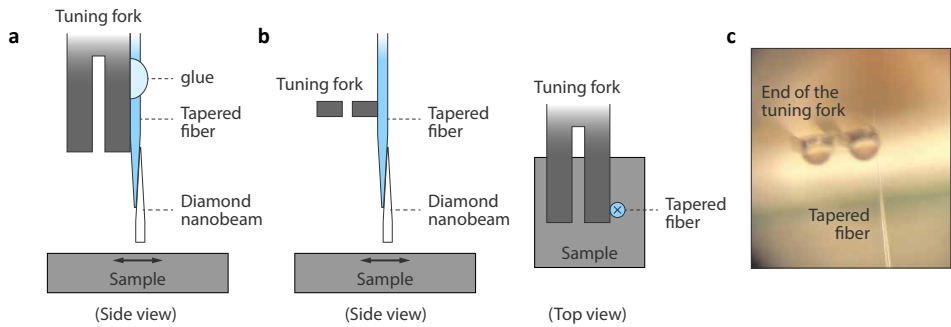
Figure 7.1 - **Envisioned schemes for implementing tuning-fork AFM on fiber-coupled diamond nanobeams. (a)** Schematics of gluing the tapered fiber parallel to the prong of the tuning fork. **(b)** Schematics of achieving lift-height feedback through the mechanical contact between the fiber and the tuning fork. The fiber is perpendicular to the tuning fork prongs in this regime. **(c)** Microscope image of a preliminary attempt of bringing a tapered fiber in contact with the tuning fork.

Here we propose two possible approaches to implement fiber-coupled diamond nanobeam sensors into a tuning-fork AFM structure, as illustrated in fig. 7.1. In the first approach, the tapered fiber is glued to one prong of the tuning fork [6], and the tuning fork can thus detect the tip-sample interaction through its resonance frequency. To realize such an assembly requires developing a workflow for the precise gluing of tapered fibers onto tuning forks, as well as designing a scan head to mount the structure on top of the sample. In the second approach, the lift-height control is instead realized through the mechanical contact between the tapered fiber

and the tuning fork, as has been used in scanning-SQUID measurements [7]. No precise gluing is needed for this approach, and it could be even possible to adjust the NV orientation *during* a measurement by rotating the fiber. The challenge again lies in the design of a dedicated scan head and ensuring the stability of the assembly in the absence of adhesive.

7.2.3. Surface roughness at the tip of the nanobeam

Compared to the diamond cantilever scanning probes, an important difference for the diamond nanobeam probes is that the NV centers need to be close to the sidewalls of the nanostructure, instead of the top surface of the diamond substrate. This is relevant because the sidewalls, created during the fabrication process, are much rougher than the diamond surface that is mechanically polished pre-fabrication, visible in figs. 3.3 to 3.5. For our tip-NV nanobeams, this has not been a critical issue since on the one hand we have many NVs per nanobeam, and on the other hand the implantation depth ($\sim 60\,$nm) is relatively large compared to the roughness and the NVs are therefore less affected. Yet for an individual NV center close (usually on the order of $10\,$nm or lower for the cantilevers) to the surface, the actual probe-sample distance could be uncertain as the roughness becomes comparable with the implantation depth, and the coherent properties of the NV could also be severely affected.

The stripe-shaped roughness on the diamond sidewalls is a combined effect from non-ideal e-beam lithography, hard mask etch and diamond etch, and is common for nano/microstructures created via reactive ion etching [8]. Therefore, optimization of various parameters of these fabrication steps is necessary to reduce the sidewall roughness, as demonstrated in refs.[9, 10].

Besides, during the course of this project we also briefly explored the possibility to improve the sidewall roughness via ion beam milling, illustrated in fig. 7.2(a). This approach is inspired by the ion beam polishing of diamond surface [11]. Since diamond requires significantly higher ion energy and fluence to be effectively polished and that the Si_3N_4 hard mask is already rough on the sidewalls after the CHF_3 etch (fig. 7.2(b)), we tried to instead use ion beam polishing to improve the sidewalls of the Si_3N_4 hard mask. Figure 7.2(b) and (c) show the change in the sidewall profiles of a Si_3N_4 on Si test structure after 2h argon ion beam milling (SCIA Mill 150) at a $4°$ shearing angle with respect to the substrate surface. The sidewall facing the ion beam shows improved smoothness, plus angled bevels at the corners. This is more obvious in fig. 7.2(d), where a structure of the same shape on the same substrate is placed perpendicular to the ion beam and is milled for 6h. A clear difference between the roughness profile of the side facing the ion beam and the opposite unmilled side is visible.

These preliminary characterizations indicate that it is possible to use ion beam milling to polish the sidewalls of the hard mask, given that the (incident-angle-dependent) milling rate and the beveled corners are quantitatively characterized and taken into account prior to pattern design.
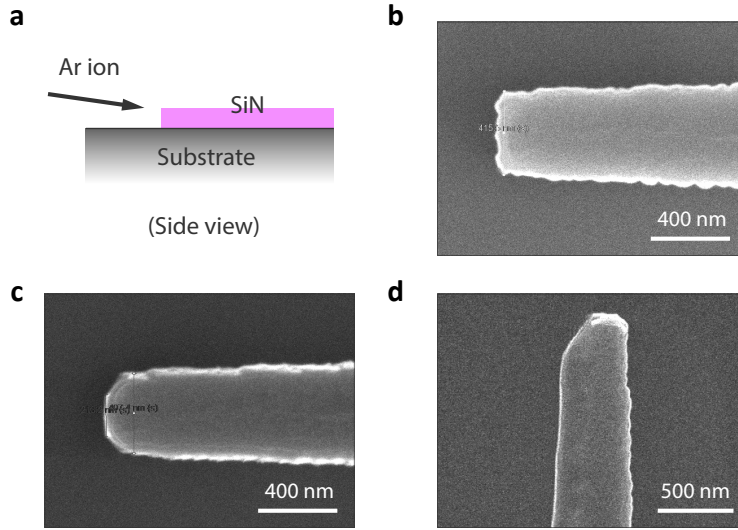
Figure 7.2 - **Effect of ion beam milling on the sidewalls of the hard mask.** **(a)** Schematics of ion beam polishing. The substrate is mounted at shearing angle with respect to the argon ion beam. **(b)** Top view SEM image of a 200 nm-thick Si_3N_4 test structure (lighter shade) on a silicon substrate (darker shade). Sidewall roughness on the order of 20~30 nm is visible. **(c)** The same structure in (b) after 2h ion beam milling with 100 keV argon ion at 4° with respect to the substrate surface. The blue arrow indicates the orientation of the ion beam. **(d)** Top view of a Si_3N_4 test structure on the same substrate that is perpendicular to the ion beam, after 6h ion beam milling with the same parameters. Roughness difference between the side facing the beam and opposite side is visible.

7.2.4. Low-temperature magnetometry with tin-vacancy (SnV) centers

One important future application of our fiber-coupled probe is scanning magnetometry at low temperature, facilitated by the all-fiber optical interface. As such, it could be an excellent platform for exploring the sensing capabilities of group-IV color centers, which have proven to be more stable against surface charge noise at low temperatures [12–14]. Considering the low-temperature instability of NV centers [15], this could be a more promising alternative for implementing single-spin magnetometry eventually in the mK regime.

Specifically, we are interested in the possible magnetometry capability of tin-vacancy (SnV) center in diamond - a defect consisting of a tin atom in between *two* adjacent vacancies in the carbon lattice [16]. In recent years, it has emerged as a promising platform for quantum information processing thanks to its better properties as a qubit compared to the NV center, such as stronger zero-phonon-line (ZPL) emission and better stability against electrical noise. And

since the manipulation, readout and magnetic field dependence of the SnV spin states are also already experimentally demonstrated [14], they can in principle also function as magnetometers.

Towards the realization of low-temperature SnV magnetometry, major challenges could include the following aspects:

- **Resonant excitation and readout of SnV centers:** A crucial part of manipulating and reading out the spin states of a SnV center is the resonant excitation of these states, using a tunable laser at around 620 nm. While this has already been demonstrated experimentally [13], extra challenges still apply for our fiber-based devices. Compared to the off-resonant excitation regime of NV centers, the fiber-coupling efficiency could be different and the composition of background fluorescence also needs to be characterized. Also as mentioned in section 7.2.1, since it is not possible anymore to filter out the background at 700 nm, alternative methods to suppress the fiber and glue autoluminescence will be required.

- **Establishing sensing protocols:** One possibility of SnV magnetic sensing is measuring the Zeeman splitting of their ground states via phololuminescence excitation (PLE), as demonstrated in fig.2 of ref.[14]. Whether this is a feasible solution for scanning-probe measurements remains to be tested experimentally.

- **Characterizing magnetic field sensitivity:** Ultimately, whether SnV centers can be a practical magnetic sensor at low temperatures is very much dependent on their magnetic field sensitivity. It is therefore crucial to characterize the sensitivity of possible sensing protocols, and see how it compares to the existing NV-based solutions.

7

References

[1] N. H. Wan, B. J. Shields, D. Kim, S. Mouradian, B. Lienhard, M. Walsh, H. Bakhru, T. Schröder, and D. Englund. "Efficient extraction of light from a nitrogen-vacancy center in a diamond parabolic reflector". In: *Nano Letters* 18.5 (May 2018), pp. 2787–2793. ISSN: 1530-6984. DOI: 10.1021/acs.nanolett.7b04684.

[2] T. Fujii, Y. Taguchi, T. Saiki, and Y. Nagasaka. "A fusion-spliced near-field optical fiber probe using photonic crystal fiber for nanoscale thermometry based on fluorescence-lifetime measurement of quantum dots". In: *Sensors* 11.9 (Sept. 2011), pp. 8358–8369. ISSN: 14248220. DOI: 10.3390/s110908358.

[3] S. Dix, D. Lönard, I. C. Barbosa, J. Gutsche, J. Witzenrath, and A. Widera. "A miniaturized magnetic field sensor based on nitrogen-vacancy centers". In: *arXiv:2402.19372* (Feb. 2024). URL: https://arxiv.org/abs/2402.19372.

[4] M. Schmid, D. Ludescher, and H. Giessen. "Optical properties of photoresists for femtosecond 3D printing: refractive index, extinction, luminescence-dose dependence, aging, heat treatment and comparison between 1-photon and 2-photon exposure". In: *Optical Materials Express* 9.12 (Dec. 2019), p. 4564. ISSN: 2159-3930. DOI: 10.1364/OME.9.004564.

[5] P. Maletinsky, S. Hong, M. S. Grinolds, B. Hausmann, M. D. Lukin, R. L. Walsworth, M. Loncar, and A. Yacoby. "A robust scanning diamond sensor for nanoscale imaging with single nitrogen-vacancy centres". In: *Nature Nanotechnology* 7.5 (2012), pp. 320–324. ISSN: 17483395. DOI: 10.1038/nnano.2012.50.

[6] F. Gao, X. Li, J. Wang, and Y. Fu. "Dynamic behavior of tuning fork shear-force structures in a SNOM system". In: *Ultramicroscopy* 142 (2014), pp. 10–23. ISSN: 18792723. DOI: 10.1016/j.ultramic.2014.03.011.

[7] C. L. Tschirhart, M. Serlin, H. Polshyn, A. Shragai, Z. Xia, J. Zhu, Y. Zhang, K. Watanabe, T. Taniguchi, M. E. Huber, and A. F. Young. "Imaging orbital ferromagnetism in a moiré Chern insulator". In: *Science* 372.6548 (June 2021), pp. 1323–1327. ISSN: 10959203. DOI: 10.1126/science.abd3190.

[8] A. Toros, M. Kiss, T. Graziosi, S. Mi, R. Berrazouane, M. Naamoun, J. Vukajlovic Plestina, P. Gallo, and N. Quack. "Reactive ion etching of single crystal diamond by inductively coupled plasma: State of the art and catalog of recipes". In: *Diamond and Related Materials* 108 (Oct. 2020). ISSN: 09259635. DOI: 10.1016/j.diamond.2020.107839.

[9]   M. Kiss, T. Graziosi, A. Toros, T. Scharf, C. Santschi, O. J. F. Martin, and N. Quack. "High-quality single crystal diamond diffraction gratings fabricated by crystallographic etching". In: *Optics Express* 27.21 (Oct. 2019), p. 30371. ISSN: 1094-4087. DOI: 10.1364/OE.27.030371.

[10] M. Mitchell, D. P. Lake, and P. E. Barclay. "Realizing Q > 300 000 in diamond microdisks for optomechanics via etch optimization". In: *APL Photonics* 4.1 (Jan. 2019). ISSN: 2378-0967. DOI: 10.1063/1.5053122.

[11] S. Mi, A. Toros, T. Graziosi, and N. Quack. "Non-contact polishing of single crystal diamond by ion beam etching". In: *Diamond and Related Materials* 92 (Feb. 2019), pp. 248–252. ISSN: 09259635. DOI: 10.1016/j.diamond.2019.01.007.

[12] A. E. Rugar, S. Aghaeimeibodi, D. Riedel, C. Dory, H. Lu, P. J. McQuade, Z.-X. Shen, N. A. Melosh, and J. Vučković. "Quantum photonic interface for tin-vacancy centers in diamond". In: *Physical Review X* 11.3 (July 2021), p. 031021. ISSN: 2160-3308. DOI: 10.1103/PhysRevX.11.031021.

[13] L. De Santis, M. E. Trusheim, K. C. Chen, and D. R. Englund. "Investigation of the Stark effect on a centrosymmetric quantum emitter in diamond". In: *Physical Review Letters* 127.14 (Sept. 2021), p. 147402. ISSN: 0031-9007. DOI: 10.1103/PhysRevLett.127.147402.

[14] E. I. Rosenthal, C. P. Anderson, H. C. Kleidermacher, A. J. Stein, H. Lee, J. Grzesik, G. Scuri, A. E. Rugar, D. Riedel, S. Aghaeimeibodi, G. H. Ahn, K. Van Gasse, and J. Vučković. "Microwave spin control of a tin-vacancy qubit in diamond". In: *Physical Review X* 13.3 (Aug. 2023), p. 031022. ISSN: 2160-3308. DOI: 10.1103/PhysRevX.13.031022.

[15] D. Rohner. "Towards Single Spin Magnetometry at mK Temperatures". PhD thesis. University of Basel, 2020. URL: https://edoc.unibas.ch/76045/.

[16] T. Iwasaki, Y. Miyamoto, T. Taniguchi, P. Siyushev, M. H. Metsch, F. Jelezko, and M. Hatano. "Tin-vacancy quantum emitters in diamond". In: *Physical Review Letters* 119.25 (Dec. 2017), p. 253601. ISSN: 0031-9007. DOI: 10.1103/PhysRevLett.119.253601.

7

Acknowledgments

I

I still remember the first time I received a copy of PhD thesis from a graduating colleague during my first year in the department: Back then, I was really surprised by the tradition of writing these many-page-long acknowledgment sections. But soon enough, I came to realize that it absolutely makes sense to be extensive on this *most important chapter* of the entire thesis. As the first (if not the only) thing that most people will read when they receive a thesis[1], the acknowledgment is not only a proper thank-you note to the people without whom this journey would not be possible, but also the only place where a PhD student is allowed to write subjectively, illogically, imprecisely and emotionally - like an actual human being, if that ability is not yet permanently lost.

As soon as I realized this, I immediately started picturing at the back of my head how I should write my own acknowledgment, and that was already more than two years ago. Now here I am, finally writing it, I hope that the next few pages could give you a glimpse from my perspective into what the past four years[2] was *actually* about, outside those 100+ previous pages of science.

---

[1] But, my friend, if I get you here, I would actually like to use this opportunity to recommend reading also the rest of my thesis, at least the introductory sections - I did spend some effort to hopefully make them understandable!

[2] Well, at least the good parts, which are fortunately also most of the parts. The complaints are instead addressed (implicitly) in some of my propositions, in case you are curious.

II

My PhD journey started during the covid times. In the early summer of 2020, I was sitting in my bedroom in Zürich during the lockdown looking for a PhD position, and received an interview invitation from Toeno. I gave a presentation about my Master thesis project in the morning, and afterwards had a remote tour of the lab which was still relatively empty back then, with Toeno holding his iPad being the tour guide. I was quite impressed by such a form of interview, as well as the offer for the position that I received some 3 hours after we hung up. Later on through the years, I learned that I am neither the first nor the last person in the group that was hired at such a pace - somehow indicating a certain shared mindset of the group I guess?

I'd say that for a decision concerning the next 4 entire years, it was quite a bold (and somewhat random) move to just say yes based on only a 2-hour-ish video call. Yet I am lucky enough to be able to confirm, after these years, that I ended up in the right place. The first person to thank about this is of course **Toeno**, for being one-of-a-kind as a supervisor: A supervisor who will both sit in the lab for an hour diving through a pile of matlab scripts, and drag the entire group to a random karaoke bar in Castelldefels on a conference night letting out the rock-and-roll soul within. I have learned so much from you - from NV physics to techniques of giving a presentation and writing a paper, and I am sure I will keep benefiting from them in the years to come. Thank you for all of these, and above all, for putting together a group of great people and making the Sarlab such an enjoyable place to work in!

Richard was also there during my initial interview, as he is throughout my entire PhD journey. Although I must confess that I am still no expert on nanomechanics despite auditing all the group meeting discussions in the past four years, being involved in two very different research groups has definitely helped me in many ways, whether it's for the out-of-the-box advices or simply a change of mind when I got stuck. Thank you, Richard, for all your fabrication expertise (and training me on SEM yourself, especially), your never-ending creative ideas, and always being so cheerful in our discussions!

As my second promotor, **Ronald** has been providing feedback and advices during my progress meetings, and they are always helpful and to-the-point. Thank you for keeping track with my PhD, and I look forward to discussing with you on my defence - the one last progress meeting!

Speaking of the defence, special thanks goes to the committee members - **Peter Steeneken**, **Tjerk Oosterkamp**, **Artur Widera**, **Tim Taminiau** and **Sander Otte**. Thank you for accepting the invitation to be part of the committee, for taking time assessing my thesis, and very importantly, for your kindness and understanding when coordinating the time! I look forward to our discussions.

III

Doing research is more social and collaborative than most people, including myself many years back, would have thought. It is therefore not really ideal to start a PhD during a period of *social distancing*. Nevertheless, I still got acquainted with the OGs

of both Sarlab and Norte lab despite that 1.5m barrier, and thanks to their kindness I could start smoothly with my journey.

Iacopo was already preparing for graduation when I started. As a result I think we only get to know each other better during your postdoc months, but we definitely shared some fun times together! Aside from laying the experimental foundation for the entire lab, I also really appreciate it that you're also kindly taking care of the group outside the lab, whether it's about using your Italian taste to make sure we always end up in a nice restaurant, or making sure all the stupid moments are properly recorded and documented for future defence parties. Also, thanks for all your career advices during our chats and I am really happy to see you enjoying your new role as a consultant!

Joris-"JJC"-Carmiggelt is no doubt a legendary figure in the lab and beyond. I have been constantly impressed by the genuine cheerfulness residing both in your tone of speaking and on your face since the first time we met, especially when it is boosted to another level with a proper amount of alcohol. Somehow, this and your academic excellence blends on you in an *amazing* way and make you the legend that you are. Thank you for all the positive attitude you have brought to us throughout the years, and I hope you are still keeping it up in Munich! Also, I cannot believe you're already becoming a father now - I'm really happy for you, and all the best to your family life!

In the same generation of PhD students there is also **Matthijs**, representing the seniority of Norte lab - We didn't get to work together as much, but I did still benefit from your feedback and advices on the group meetings, as everyone else in the group. Thank you for that, and also for sharing your fun stories and adventures during the beer evenings! I am sure the Scandinavian winter (and price) won't stop you in the next chapter of your adventure!

Brecht is the one who set the ground of diamond fabrication in Sarlab, and the one who taught me some of the most challenging handwork one could ever encounter in cleanroom - manipulating $50\,\mu\text{m}$-thin diamond membranes with tweezers, assembling the monstrous glassware set and boiling super dangerous acid mixtures inside, fishing the ceramic boat from the annealing oven tube with a metal hook, and counting. Having you around during these tasks has always been a mental relief for me, something I am constantly missing after you graduate and I kinda move into your role (I think I am still nowhere near your level in terms of handling diamonds with tweezers). Besides, you are also a great friend to hang out or have a chill moment with - I really enjoyed the adventures in Barcelona and during group *uitje*s, and thanks for always staying on the sober side of the group!

Besides Brecht, the two people with whom I probably shared most cleanroom time were **Andrea** and **Minxing** - helping each other out on all sorts of processes, for which I am truly grateful. The effort both of you have put into pushing the limit of nanofabrication was absolutely impressive. Andrea, I regret for not being able to attend your defence and I definitely need to catch up on how you're doing recently! Thank you for always being kind and helpful, and I am sure you will excel in whatever you are pursuing in your postdoc journey! And Minxing, thanks for the warm invitations to your place for dinner (and Texas poker). I hope that you are (finally) enjoying some well-deserved holidays after all the hard work, and I'm

curious to see what you decide to do next - Hopefully, that won't involve late-night measurements or weekend e-beam alignments anymore!

Allard, the wandering god of AFMs, is the one we can always turn to for help whenever a technical issue occurs in the lab. Although we did not work together that much, I am still thankful for the very helpful advices both on AFM and on mountain biking! It's always good to have you around the lab for an advice or a drink, and I hope you will keep staying around for many years to come!

Michael is the only person (aside from Toeno) that was already in the Sarlab when I started my PhD, and will still be there after I finish. I think that makes you on top of the Sarlab *anciënniteit* ranking. Thank you for being my cleanroom mentor, and giving me valuable advice throughout my PhD from the beginning till the end! It is always aspiring to see your passion in so many aspects of work and life, ranging from superconductors all the way to *jägermeister*. And I am really happy that all the passion and hard work are finally paying you off at the end of your PhD! Looking at how you're doing in the lab now, I would totally be not surprised if you end up also staying for four more years as a postdoc and pushing the spinwave-superconductor experiment to the next level, yet I am also sure that you will excel in anything else you might decide to do!

The man who actually stayed for four years as a postdoc is **Samer**. You certainly deserve to be crowned with another Doctor title. Despite being forever busy and hustling on a ton of different tasks (I guess that already makes you ready to become a PI), you still manage to always keep up with your positive attitude and pass it on to everybody with your signature laugh. Maybe *Snickers* is indeed the secret! Thank you for being such a reliable colleague and *such a nice guy* (quoting Brecht)! Though you are dearly missed by all of us, it is great to see you finally moving out of your hotel room to reunite with **Fran** in Groningen (and soon Edinburgh, I heard!), and at the same time becoming an actual dad after being called *Daddy Kurdi* for this many years. All the best to you and the family for the exciting new life!

IV

Well, it feels like yesterday when I was still the youngest member of the two labs. And within the blink of an eye, here I am writing this elderly memoir. I do recall, though, the first time I started to feel old as a PhD: This was at Iacopo's defence party, where I stood beside Annick, Roland and Pim - the later-to-be *New Kids* trio - hearing them chatting on their first (to my knowledge) gathering. For a distinct second, I had the "Aha, that's the new generation" feeling. And one sign of getting old is not being able to remember the exact order of history anymore: bear with me if the rest of this memoir no longer follows the correct time order!

In any case, from my perspective "the new generation" started with **Fabian**, the first master student I supervised, who continued in the group as a PhD to take on new challenges. Working with you in the lab upstairs was definitely fun and fruitful! It's quite amazing to see how far you have come since the day you start with your master project, and I'm grateful to have you as my paranymph! Apart from being a sharp and reliable colleague, in my foreign eyes, you are definitely one of the most anti-stereotypical Dutch I ever came across, with your somewhat ruthless remarks

on various beings, and the obsession with the word *idiot* in those remarks - and I found it fascinating. Thanks for bringing such a distinct character to the group, and I hope you keep up with that! In the next years to come, I do have the feeling that apart from becoming the next level of master on cryogenic scanning NVs (that for sure), you will eventually also become the new *legend* of the group, and I look forward to that!

Roland started off in the group as a somewhat low-key and hard-working master student. I don't think we had much chance to talk to each other during that period, until you stayed in the group as a PhD and became my office mate. You never fail to impress me by how you manage to tackle the endless challenges in LT1 (I really hope the magnets can get fixed soon!), and in the same time being the loving young father of Andrea. Thank you for all the sweet stories you shared with us, and for being a great office mate! I believe with your dedication and perseverance, you're already not far away from getting great images from those Josephson junctions!

Pim has always been the energy boy of the group since day 1, with the passion and ability to climb on anything - bouldering is really a sport that can be done anytime anywhere, no? Besides that, you are also a quick learner and sharp thinker, picking up all those superconductor physics and cleanroom techniques at an impressive pace. Thank you for the active energy you bring to the group, for keeping the lab clean and for doing a great job in the organizational role - whether it's data meetings or group uitje! I look forward to hearing both new juicy results from LT2, and your new adventure in another wilderness somewhere else in the world!

Also in the legendary *New Kids* trio there's **Annick**. Getting to know you and your lifestyle truly broadened my horizons - your dedication to the outdoors and your level of profession are really unmatched. I miss the times when you would drag the group for a refreshing after-lunch CoffeeStar walk, as well as our struggle to get NVAFM working on the practicum setup. Thank you for being a cheerful and energetic friend and colleague, and I am really happy for you on making such a courageous and conscious decision to search for a new path that truly suits you. I can't wait to hear about your adventure in CERN the next time we meet!

Meanwhile across the street, Norte lab also moves into the new generation with the addition of **Lucas** and **Paulina**. Both of you have quickly became key players of the group and cleanroom masters at the same time. Thank you for sharing your exciting results in the group meetings and helping everyone out! Lucas, your photonic crystals are definitely looking more amazing every week, I'm sure soon enough they'll have their chance to float! Paulina, I think your calm and persistent attitude will make you go far in your research, and I am curious to find out what you can come up with your resonators!

Our friend **Samuel** took upon the challenge of building an entire new scanning setup immediately after joining the Sarlab as a postdoc. With a great amount of dedication and hard work (do you ever take days off, by the way?), it's definitely a huge achievement to be finally imaging spin waves with the sloth microscope! Also, thank you for always giving such enjoyable data meetings updates and talks - you have really *defined* a style of presentation with your impressive knowledge and sense of humour. Best of luck with the rest of your time in the lab, and with your next

chapter of journey towards becoming a professor!

Gesa joined me on the same project roughly a year after we first met at NanoMRI in Barcelona. We spent quite some time in the lab upstairs trying to figure our how to get those nanobeams fixed to the fiber tips, and finally got it to work after trying all kinds of random methods. Thank you for your time reading through and giving feedback on my thesis, as well as all the discussions that helped me clearing my mind! It is always nice to have a second brain when working on these exploratory challenges. Also, thank you for taking care of the group, not only with your professional experience, but also with your cooking and baking skills. I believe your effort on both tin vacancies and finding a new position will pay off very soon!

And in my final PhD months, I had the luck of working together with my fellow *Y&Y* partner-in-crime **Yasmin** on a number of different projects: from figuring out what is a spin, to learning how to make a nice cappuccino. All of these has been so joyful that inviting you to be my paranymph becomes the only reasonable decision. And your reaction upon the invite was just golden - I could live on that for like a year! I remember in that late night Margarita session of the group uitje, you were asking about what makes a person *young* (though in a very different context) - you know what, I think you yourself are the exact definition of that: sharp, energetic, always curious, passionate about life, plus a right amount of gen-Z girl vibe. Thank you for all of these, and I do hope and believe that stress will not stop you from keeping up the spirit and living life to its fullest as always! Best of luck for your PhD, and the quest of becoming a master bartender-barista - I have no doubt you will do great in both!

Throughout the years, I have also encountered many other people in both labs who, despite not having the chance to share longer time together, are still very much essential reasons of my PhD journey being enjoyable. **Thomas**, having you as my first student to supervise had definitely raised my expectation standards for student projects. You did a great job with the simulations! **Pepijn**, thank you for the codes you wrote on RT3 which we still use now, and it was fun working together with you! **Andrew**, on top of all the stories of your excellence I constantly hear from Michael, you also remain the most self-disciplined person I have ever met. I'm sure you are still at top level in whatever you are up to now! **Tim**, you have been such a good fit to both the LT1 team and the entire group. It was always pleasant talking to you, wish you all the best at TNO! **Ilse**, organizing the uitje with you was really fun. Thank you also for bringing your taste of art to the lab! **Ata**, I really enjoy your kind and easy-going character, and I am really looking forward to seeing the 400W laser full power at work! **Megha**, thanks for the group meeting discussions and I hope your DBR mirrors will work as you wish soon! **Merel**, your energy and positiveness are truly aspiring. Best of luck on measuring spin waves and winning the LT2 plank contest! Also my heartful thank goes to **Olaf**, **Helena**, **Edouard**, **Kaveh**, **Nikolaj**, **Leon**, **Tijmen**, **Tjipke**, **Fenghuan** and **Bas** for our short yet enjoyable interaction!

V

Okay, this has already become way longer than I anticipated. But again, since I am (finally) not writing anything academic, I think I should be allowed to be not

concise. And bear with me, we're not there yet, as the interpersonal aspect of a PhD journey goes of course way beyond one's own lab(s).

Nina and I started at basically the same time (might be the same day even, according to my vague memory), and has always been our lighthouse in the cleanroom - My learning and progress of diamond fabrication could have taken way longer and way more detours without you generously sharing your recipes and valuable experience. Your dedication in fabrication and the level of mastery as a result are unmatched. Thank you for all of this, and wish you all the best in wrapping up the great work and obtaining the PhD after all the effort - you definitely deserve every bit of that!

And niche as it might be, diamond nanofabrication is a dominant part not only for my PhD, but also for many other people. Though working on very different topics, we still manage keep each other updated through helpful discussions, for which I am grateful. Therefore also a big thanks to the rest of the diamond fab crew - **Julia** (It's always a pleasure discussing with you and all the best to the rest of your PhD!), **Max**, **Chris**, **Colin**, **Sezer**, **Simon**, **Salahhudin** (Great to see you starting your own group now and I hope your recruitment is going well!), **Réne** (for the career talk and advices) and **Efi** (for the good times in Hasselt together with Sal and Réne!).

That being said, I believe all of us can agree that the *true* heroes behind all the fab are the top-notch professional staff of the Kavli NanoLab, our cleanroom. I have heard many stories of cleanrooms elsewhere in the world over the years, which made me further convinced that we are privileged to have you guys in charge of all those equipments and providing expertise whenever we need. **Marc**, thanks for the organization and your cheerful spirit both in discussions and QN events! **Eugene**, thanks for keeping both myself and my samples safe in the wet bench, and bearing with us constantly bugging you on the progress of new setups, or our diamonds getting lost once again in another random corner. **Charles**, thanks for all the etcher expertise and solving every weird error ever happened to them. I sincerely wish less wafers will get chopped inside those chambers! **Roald**, thanks for your enthusiasm and the inspiring discussions, for the ellipsometry course, and for always being available immediately the next day for intro/training/tests - something I really miss after you left the CR crew! All the best for the PhD journey! **Hozanna**, thanks for spending time experimenting on FIB with me - though we did not went for the FIB approach in the end, I still believe that approach could have its day somewhere in the future! **Bas**, thanks for the thin film expertise and the chill chats inside and outside CR! **Arnold** and **Anja**, thanks for always keeping the e-beam in good order for all these years despite all the challenges! Together with **Lodi**, **Pauline**, **Brian**, **Marinus**, **Marco**(2x), **Ewan**, **Ron**, **Esther** and **Loïc**, thanks for the effort to make everything in the CR possible!

Equally important is the support we get from the Quantum Nanoscience department. **Tino**, thank you for helping setting up the lab upstairs, taking care of all the infrastructure and making sure our lab is always safe! And on top of all these, your passion (for Feyenoord, among others) and cheerful spirit is also an essential part of our department! **Ronald**, thanks for bringing all the custom parts from my CAD designs into reality - the machine shop technique of yours definitely qualifies

as wizardry from my perspective! **Lizzy**, **Marijke** and **Karin**, thanks for always being super helpful and efficient in terms of any administrative issues! I believe the overall level of graduation experience can already be improved by an order of magnitude if only the graduate school could have like 10% of your efficiency. Together with **Lidewij**, **Etty** and **Erika**, thank you for making all the organizational issues in QN as smooth as they are now!

Outside doing research, the department of Quantum Nanoscience is also an enjoyable place just to dwell in, and that is only possible with the great people it consists of. Thanks to them, even an introvert like me could also enjoy interpersonal connections under a relaxed and understanding environment, without having to worry about the *social safety* issues that are apparently around other corners of TU. I consider that a luxury.

So to start with, I would like to thank my office mates in D115 throughout the years - **Sarwan**, **Adrian**, **Thomas**, **Robin**, **Roland** and **Clinton** - for making the office hours (arguably the not-so-exciting part of an experimental physics PhD) relaxed and productive. Then, the leading figures of social events, **Sonakshi** (thanks for explaining your fiber mounts!), **Evert** (thanks for your presence and discussion in and after many of my talks!), **Álvaro** (I always enjoy your Spanish cheerfulness and anecdotes of the department!), **Gary**, **Maz**, along with everyone in the C&C committee, thank you for organizing all the social events to bring everyone together! Also, for everyone with whom I have shared a coffee/beer's time - **Luigi**, **Mattias**, **Rasa**, **Lukas**, **Parsa**, **Niccolo**, **Jingkun** (thanks for the training on HF fibers!), **Patrick**, **Ulderico**, **Alex**, **Talieh**, **Yu** (thanks for the training on the Hitachi!), **Jin**, **Yong**, **Liu**, **Xiong**, **Gaia**, **Emanuele**, **Lorenzo**, **Daniël** (thanks for explaining your setup!), **Onima**, **Chris** (thanks for the Captain Morgan, it's not very common to receive such a gift for CR training!), **Guido**, **Damian(o)**, **Hans** (the *TimTam* boys - thanks for the great times in Barcelona!), **Laurens**, **Trent**, **Riccardo**, **Raúl**, and probably many more - it has been fun getting to know all of you!

<div align="center">*VI*</div>

Naturally, *almost* everything in this thesis is a result of my work here at TU. Yet there are still people outside TU who still made contribution to a certain part of this thesis despite, for some of them, probably not knowing about it themselves. Although it's also less likely for many of you to be reading this at any point, I would still like to express my gratitude here (and consider this a small easter egg for you if you do read it!).

I spent quite some time and went through a few iterations on the cover and bottom art of this thesis (I will leave the interpretation of these works open for all of you who are reading the thesis), as I want them to kind of conclude and represent also my graphics design side quest for the past 10 years - about as long as my physics career. I am quite satisfied with how they look now, and I know this is only possible with the guidance and discussion on graphics design I had through the years. Therefore I'd like to thank **En** and **Haoyan** along with everyone in the design team of the student association of PKU School of Physics, **Kunyi** and **Qinxian** along with everyone in PKU Youth (working with you people was definitely

one of the highlights in my life!), as well as **Lotia** and **Ember** along with everyone in D-Prism. I hope that you also like this work! Also, I would like to express my heartful gratitude and admiration for the great artists and content creators on YouTube, Instagram, Behánce, Twitter (I still refuse to call it X), Weibo and other platforms, from whom I either learned software techniques or aesthetics inspiration: **Blender Guru**, **Polyfjord**, **Texturelabs**, **Ducky 3D**, **Josh Gambrell**, **Visual Dreamz**, **Steve Biggert**, **NoriZC**, and many many more. You people really deserve a dedicated hall in the Louvre!

And another special thank-you note goes to the *HomeOffice* crew with whom I spent two weeks on the gorgeous island of Madeira, where the majority of chapter 2 was completed. Although I did not turn out as productive as I had imagined myself to be, going daily on a hike after hours of writing has definitely made a significant improvement on my mental (and maybe even physical) health during my time in the writing jail. I hope I will see every one of you again either back on Madeira, or anywhere else in the world!

Finally, to my family - **Mom**, **Dad**, **Grandma** and **Grandpa**, thank you for your care and support through these years, as well as your trust on my decisions, whether it's for pursuing a PhD on the other side of the planet, or for my next career move. And also, thank you for raising me to be the person I am today, I am truly grateful for that.

VII

At the very, very end, I would like to express my sincere gratitude if you read all the way through and reach here - thank you for taking this time to read about me and my not necessarily interesting experiences. Also don't worry if you didn't, I know this is a bit too long even for Delft standards. But if there is one thing I have learned from doing research, it is the fact that if things aren't written down, they are bound to be forgotten at some point. Therefore I do believe that every single line in this acknowledgment is necessary!

And I guess my struggle to find a nice concluding remark for this acknowledgment partially indicates that I am not particularly good at saying goodbye. But luckily, as I will be sticking around in Delft for a bit longer, I will hopefully still see many of you every now and then, and I look forward to that. So with that positive attitude, I will conclude this acknowledgment and this thesis with a Chinese proverb which might not be the most suitable for the circumstance, but simply because I like how it reads in English under literal translation:

江湖再见！

"Until we meet again amidst the rivers and lakes"

Yufan Li
Delft, November 2024

Curriculum Vitæ

Yufan Li

28-12-1995	Born in Xi'an, China.

Education

2014–2018	**Bachelor of Science in Physics**
	Peking University, Beijing, China
2017	*Summer Internship*
	Universität Innsbruck, Innsbruck, Austria
2018-2020	**Master of Science in Physics**
	Eidgenössische Technische Hochschule Zürich, Zürich, Switzerland

Thesis:	Wide-field fluorescence microscope for optically-detected magnetic resonance
Supervisor:	Prof. dr. C. L. Degen

2020-2024	**Ph.D. in Applied Physics**
	Delft University of Technology, Delft, the Netherlands

Thesis:	Fiber-based scanning-probe magnetometry with nitrogen-vacancy spins in diamond nanobeams
Promotors:	Dr. ir. T. van der Sar
	Dr. R. A. Norte
	Prof. dr. ir. R. Hanson

List of Publications

4. Y. Li, G. Welker, R. Norte, and T. van der Sar. "A robust, fiber-coupled scanning probe magnetometer using electron spins at the tip of a diamond nanobeam". In: *New Journal of Physics* 26.10 (Oct. 2024), p. 103031. ISSN: 1367-2630. DOI: 10.1088/1367-2630/ad8779

3. Y. Li, F. A. Gerritsma, S. Kurdi, N. Codreanu, S. Gröblacher, R. Hanson, R. Norte, and T. van der Sar. "A fiber-coupled scanning magnetometer with nitrogen-vacancy spins in a diamond nanobeam". In: *ACS Photonics* 10.6 (June 2023), pp. 1859–1865. ISSN: 2330-4022. DOI: 10.1021/acsphotonics.3c00259

2. E. Togan, Y. Li, S. Faelt, W. Wegscheider, and A. Imamoglu. "Polariton Electric-Field Sensor". In: *Physical Review Letters* 125.6 (Aug. 2020), p. 067402. ISSN: 0031-9007. DOI: 10.1103/PhysRevLett.125.067402

1. T. Luan, Y. Li, X. Zhang, and X. Chen. "Realization of two-stage crossed beam cooling and the comparison with Delta-kick cooling in experiment". In: *Review of Scientific Instruments* 89.12 (Dec. 2018). ISSN: 0034-6748. DOI: 10.1063/1.5046815